EVIDENCE OF ABRUPT HYDROCLIMATE AND ENVIRONMENTAL CHANGE IN THE GARHWAL HIMALAYA, INDIA THROUGH AN APPLICATION OF NON-DESTRUCTIVE, RADIOLOGICAL METHODOLOGIES TO LACUSTRINE SEDIMENT

by

EMILY ALYSSA NIEDERMAN

(Under the Direction of David F. Porinchu)

ABSTRACT

Non-destructive, radiological imaging approaches were applied to a 3.80 m long sediment core recovered from Deoria Tal, a mid-elevation lake located at 2393 m a.s.l. in the Garhwal Himalaya, India to characterize abrupt climatic fluctuations. Ten AMS ^{14}C dates indicated that the core extends back to 5200 cal yr BP and were used to calibrate the results from the X-ray fluorescence (XRF), X-ray, and CT scans. Anomalous hydroclimate episodes, evidenced by variations in elemental concentrations and sediment density, are centered at 4850, 4200, and 3100 cal yr BP. The 4850 and 4200 cal yr BP events were initially characterized by elevated detrital input, greater sediment density, and decreased lake ventilation, reflecting elevated lake level. The 3100 cal yr BP event was characterized by lower detrital flux, decreased sediment density, and increased oxygenation, reflecting lake drawdown. The hydroclimate record was compared with archeological evidence of regional civilization and cultural change.

INDEX WORDS: India, paleoclimatology, lake sediment, X-ray fluorescence (XRF), Computerized Tomography (CT), radiography, abrupt climate change, non-destructive imaging, Harappa

EVIDENCE OF ABRUPT HYDROCLIMATE AND ENVIRONMENTAL CHANGE IN THE GARHWAL HIMALAYA, INDIA THROUGH AN APPLICATION OF NON-DESTRUCTIVE, RADIOLOGICAL METHODOLOGIES TO LACUSTRINE SEDIMENT

by

EMILY ALYSSA NIEDERMAN

B.S., Stetson University, 2017

A Thesis Submitted to the Graduate Faculty of The University of Georgia in Partial Fulfillment of the Requirements for the Degree

MASTER OF SCIENCE

ATHENS, GEORGIA

2021

EVIDENCE OF ABRUPT HYDROCLIMATE AND ENVIRONMENTAL CHANGE IN THE GARHWAL HIMALAYA, INDIA THROUGH AN APPLICATION OF NON-DESTRUCTIVE, RADIOLOGICAL METHODOLOGIES TO LACUSTRINE SEDIMENT

by

EMILY ALYSSA NIEDERMAN

Major Professor:	David F. Porinchu
Committee:	David S. Leigh Suzanne E. Pilaar-Birch

Electronic Version Approved:

Ron Walcott
Vice Provost for Graduate Education and Dean of the Graduate School
The University of Georgia
August 2021

DEDICATION

To the closest people who lovingly supported me around the world; in times of health, sickness, and plague; and in God, we trusted.

ACKNOWLEDGEMENTS

Firstly, I show my gratitude to my advisor, Dr. Porinchu, the Environmental Climate Lab, and the University of Georgia's (UGA) Geography Department for making available to me the opportunity and providing the resources. Specifically, I appreciate Hunter Kunzelmann, Andrew Knazek, and Stephen Cooper for their assistance during key research steps. Next, I appreciate my committee members, Dr. Leigh and Dr. Birch for their guiding expertise. I am indebted to the Geology Department at Kumaun University (KU) in India and specifically to Professor Kotlia and his family for hosting the research expedition, assisting in the on-site lab work, and for his geological expertise for the study site. I appreciate Neha Kholia from KU for making the original figures for the stratigraphy and Dr. Anoop Kumar for providing the base map utilized in Figure 1.3. Additionally, without Dr. Speakman making available the facility at the Center for Applied Isotopes Studies (CAIS) for the XRF analysis, and additionally, the helpful staff at the UGA's Veterinary Teaching Hospital's Radiology and Imaging Department, namely Billie Rae King, Dana Duncan, Charleen Romine, and Dr. Secrest, this paper would not have been possible. Therefore, many thanks go to the wonderful facility and the dedicated people at both facilities. The guidance received from Dr. Brendan Reilly from Oregon State University (OSU) was paramount in processing the computed tomography (CT) scans and very much appreciated. Lastly, I express gratitude to my brother, Eric Niederman, who first transcribed the python script for an initial step toward processing of the XRF data.

TABLE OF CONTENTS

LIST OF TABLES

Page

LIST OF FIGURES

Page

CHAPTER 1

INTRODUCTION

1.1 Context

The Indian Summer Monsoon (ISM) is the main source of precipitation for India. The timing and intensity of the ISM influences the success of the agricultural sector and thereby, directly impacts the livelihoods of a large portion of the population (Dimri et al., 2016). From June to September, the subcontinent of India receives over 80 % of its annual precipitation (Gadgil, 2003; Paul et al., 2016) but year-to-year variations in the ISM may result in severe negative hydroclimate anomalies, leaving much of the country in a drought. The importance of the ISM and ISM-related rainfall (ISMR) to the country is reflected in India's Gross Domestic Product (GDP). Indian GDP was reduced 2 – 5 % during drought episodes between 1951 and 2003, regardless of the decreasing contribution of the agricultural sector to the total GDP during this interval (Gadgil and Gadgil, 2006). The profound socio-economic impacts of variations in the ISM in recent decades has encouraged the Indian government and climate scientists to re-double efforts into predicting year-to-year variations in ISMR and understanding the drivers of ISM variability on annual to multi-decadal timescales. Analysis of historical data indicate that there is no long-term trend apparent in ISMR between 1871 and 2004 (Gadgil and Gadgil, 2006); however, recent work has identified the occurrence of a regime shift in Asian monsoon convection strength (Turner and Hannachi, 2010) and that the frequency of extreme ISM events has increased in recent decades (Goswami et al., 2006; Singh et al., 2014).

The timing of the onset of the ISM is intimately connected with the seasonal migration of the Inter-tropical Convergence Zone (ITCZ), with the mean summer position of the ITCZ defining the northernmost extent of the ISM dominated region in south Asia (Dixit and Tandon, 2016; Goswami and Chakravorty, 2017). The northward movement of the ITCZ during the boreal summer facilitates the flow of warm, moist air, from the Indian Ocean, inland into the interior of the Indian subcontinent, beginning in southern India in late June. There are two primary branches of the ISM: the Arabian Sea branch providing moisture from the west and the Bay of Bengal branch providing the larger portion of moisture to the subcontinent from the east (Ponton et al., 2012). There are three drivers that are hypothesized to exert a major influence on the timing and intensity of the ISM: (1) the strength of thermally-induced low pressure over Tibetan Plateau (Dixit and Tandon, 2016), (2) fluctuations in North Atlantic sea surface temperatures (SSTs) and the North Atlantic Oscillation (Gupta et al., 2003), and (3) ENSO-related variations in SSTs in the tropical Pacific (MacDonald, 2011). In addition to these drivers, other factors such as the Equatorial Indian Ocean Oscillation (EQUINOO) (Gadgil et al., 2003), solar and volcanic activity (Gray et al., 2010; van Loon and Meehl, 2012), changes in land cover (Paul et al., 2016), and changes in atmospheric chemistry (Bollasina et al., 2011) have been implicated in ISM variability. Developing mechanistic, process-based general circulation models (GCMs) of the behavior of the ISM that incorporate various proposed drivers of ISM variability has proven difficult. Gadgil and Srinivasan (2011) noted that it was expected that none of the ISM models produced from the 'Seasonal Prediction of the Indian Monsoon' (SPIM) project would be able to resolve ISM anomalies correctly for the interval of study.

The relationship between the ISM and agricultural productivity holds for not only the modern context in India but also extends back to the mid-Holocene, with the Harappa, an

ancient, hydraulic, socially complex, and highly urbanized civilization based along the Indus and Ghaggar-Hakra river valleys, which experienced significant demographic contraction coinciding with a multi-decadal drought centered at 4200 cal yr BP (Staubwasser et al., 2003; Giosan et al., 2012). The specific causes of the Harappa or Indus Valley Civilization's demise have been hotly debated, with researchers suggesting it was primarily climatologically driven (Ponton et al., 2012), socially driven (Madella and Fuller, 2006), some mix of the two (MacDonald, 2011; Giosan et al., 2012; Schug et al., 2013; Sarkar et al., 2016), or due to re-organization of the river network (Chatterjee and Ray, 2017). There remains a paucity of information on the drivers of the ISM and ISM variability, and limited detail on how fluctuations in the ISM may have impacted local geographies during the mid-Holocene. Therefore, to gain a better understanding of the potential influence of climate on the Harappa during the mid- to late Holocene, it is imperative to develop detailed, well-constrained records of the ISM and hydroclimate variability for northern India during this interval.

There are two different methodological approaches that can be used to develop robust, regional reconstructions of ISM variability in northern India. The first approach involves the development of well-dated, high-resolution paleoclimate records in new localities that are constrained and interpreted based on modern observations (Dixit and Tandon, 2016). The second approach involves utilizing global or regional climate models to simulate monsoon behavior during the past (Midhun and Ramesh, 2016). Both methods aim at extending our understanding of the spatial and temporal patterns of hydroclimate variability in this region during the Holocene. I will follow the first methodological approach in this thesis. In addition to paleoclimatological, lake sediment-based reconstructions from northern India (Prasad et al., 1997; Sharma and Gupta, 1997; Enzel et al., 1999; Chauhan and Sharma, 2000; Sharma et al.,

2000; Wünnemann et al., 2010; Leipe et al., 2014; Menzel et al., 2014; Chauhan et al., 2015; Demske et al., 2016; Saxena and Singh, 2017; Tripathi et al., 2017) and from the ISM dominated region of China (Peng et al., 2109), a partial list of other well-dated paleoclimatological archives include continental shelf sediments (Ponton et al., 2012; Ankit et al., 2017), $\delta^{18}O$ from the Indian Ocean (Bolton et al., 2013), tree rings (Singh et al., 2017), and stalagmites (Sanwal et al., 2013; Kotlia et al., 2015; Kotlia et al., 2017). These records are characterized by varying temporal resolution and duration, ranging from a few millennia to 500,000 years.

Dixit and Tandon (2016) utilized fifty-seven paleoclimate records including speleothems, tree rings, marine sediment cores, and lake sediment cores to develop a comprehensive reconstruction of hydroclimate variability spanning the last millennia for South Asia. However, Dixit and Tandon (2016) noted that the northern region of India (whether directly influenced by the ISM or by the Indian Winter Monsoon (IWM) is poorly represented in their synthesis and that the addition of well-constrained lake sediment-based paleoclimate reconstructions from northern India should be prioritized. Developing highly resolved lake sediment reconstructions of ISM variability can be used to address outstanding questions related to the influence of climate change on the Harappa and potentially improve our understanding of how the Harappa responded to climate and environmental change (Madella and Fuller, 2006). These are the issues that will be addressed through the use of a novel methodological approach: non-destructive, radiological imaging.

Existing lake-based paleoclimate reconstructions from northern India largely rely on detailed analysis of pollen (Sharma and Gupta, 1997; Chauhan and Sharma, 2000; Sharma et al., 2000; Wünnemann et al., 2010; Leipe et al., 2014; Chauhan et al., 2015; Demske et al., 2016; Saxena and Singh, 2017), biogenic silica (Tripathi et al., 2017) and the geochemistry of organic

matter (Prasad et al., 1997; Enzel et al., 1999; Menzel et al., 2014). Recently, the relatively rapid and inexpensive assessment of environmental variables in lakes sediment cores through the use of non-destructive imaging approaches has been used to successfully develop higher resolution reconstructions of climate and environmental change than studies which solely rely on sediment geochemistry (Zaragosi et al., 2006; Sáez et al., 2009; Fouinat et al., 2017). However, the use of non-destructive imaging approaches in lake-based paleoenvironmental research in India is limited, with very few X-Ray Fluorescence (XRF) based study completed in northern India (Wünnemann et al., 2010; Bohra and Kotlia, 2015) and one in ISM-dominated region of China (Peng et al., 2019). To date there have been no studies published based on lake sediment cores recovered from Garhwal Himalaya that make use of X-ray images (or radiographs) or Computerized Tomography (CT) scans. Applying XRF, X-ray, and CT scans to a well-dated lake sediment core from northern India will provide much-needed insight on long-term and abrupt fluctuations of the ISM during the mid- to late Holocene.

1.2 Study Region

Deoria Tal (30.5222° N, 79.1277° E) is located on a hilltop (2393 m a.s.l.) above Okhimath (alt. spelling Ukhimath) and 3 km from Sari Village in the Rudraprayag district of Uttarakhand, a state in northern India (Figure 1.1). The lake has an approximate surface area of 2.7 ha and a closed catchment area of 11 ha, rendering it potentially a climatically sensitive lake.

Situated in the Garhwal Himalaya (within the Inner Lesser-Higher Himalayan domain), Deoria Tal is located above the Main Central Thrust (MCT) zone that is characterized by a high-grade metamorphic terrain. The geological context for the region encompassing Deoria Tal is characterized by three major lithotectonic groups, delineated by the Bhulkhund Thrust, Okhimath Thrust, and Banswara Thrust, which are listed from north to south, respectively (Bist

and Sinha, 1980; Figure 1.2). Deoria Tal is located just to the south of the Bhulkund Thrust in a zone that is characterized by porphyritic gneiss with mica schist and granite also present. Geomorphologically, the area is full of dissected hills and mountains. This is a tectonically and seismically active area; landslides have been witnessed in the region, including the 2012 landslide at Okhimath (Islam et al., 2014). The formation of the Deoria Tal lake basin likely resulted from tectonic activity (Kotlia, 2019, personal communication).

The major source of precipitation for Deoria Tal is the ISM. Deoria Tal lies south of the Intertropical Convergence Zone (ITCZ), which demarcates the northern limit of the ISM dominated region (Dixit and Tandon, 2016; Goswami and Chakravorty, 2017). The ISM is characterized by heavy rains during the summer months (June-September). The daily average of ISMR typically ranges between 8 and 10 mm/day during the summer (JJAS) (Patwardhan et al., 2016; Figure 1.3). Deoria Tal can also receive additional precipitation during the winter (December-February) from extra-tropical cyclones, known as Western Disturbances, Westerlies, or the IWM (Dimri et al., 2016). A present time climograph of Chamoli Gopeshwar (Climate-Data, n.d.; Figure 1.4) provides an example of the regional climate shared with Deoria Tal, including the dominant precipitation being sourced during the ISM.

Deoria Tal is situated in the temperate vegetation belt. The temperate forest is comprised mainly of *Quercus semecarpifolia* (Sharma and Gupta, 1997; Sharma et al., 2000) with a mix of shrubby elements and a thick ground cover, predominantly made up of grasses, also present. The littoral zone of Deoria Tal is covered by a mat of water chestnut (genus: *Trapa*). *Trapa* is a rooted aquatic plant, found in relatively shallow and nutrient rich water (1 - 4 m), with leaves floating on the surface (Hummel and Kivat, 2004). Regionally speaking, similar vegetation cover was also observed to the southeast of Deoria Tal at Dewar Tal (Chauhan and Sharma, 2000) and

at Badanital which is west-southwest of Deoria Tal (Demske et al., 2016), suggesting a strong correspondence still exists between vegetation and climate in the mid-elevations of this region. Alternatively, grassland with sparse tree coverage predominantly comprises the rest of the eastern Ganga Plain (Saxena and Singh, 2017) and moving westward to the central Ganga Plain (Chauhan et al., 2015; Tripathi et al., 2017; Kar and Quamar, 2019).

Currently, the lake is protected by the Uttarakhand Forestry department, however, human impact on the lake system may have varied during the past. Deoria Tal is located along the eastern part of the Ganga plain. The Harappa started their eastward migration through the Ganga Plain at c. 5000 cal yr BP (c. 3050 BC) (Gupta et al., 2006), with the human-induced environmental changes observed in the Garhwal Himalaya at c. 3950 cal yr BP (c. 2000 BC) occurring during the Late Mature and post-Harappa phases. Figure 1.5 includes the known Harappa civilization settlements (Dutt et al., 2018) with the juxtaposition of Deoria Tal. After the Harappa, human influences increase in this region with the arrival of the Painted Grey Ware (PGW) people in c. 2950 cal yr BP (c. 1000 BC) with large-scale cultivation in the upper Jamuna-Ganges valley (Bryson and Baerreis, 1967; Gupta et al., 2006). At nearby Dewar Tal, evidence for human impact between 4220 and 2430 cal yr BP (2270 – 480 BC) is evident with an increase in the amount of charcoal fragments and a marked increase in fungi spores associated with dung from grazing animals at c. 2430 BP (480 BC) (Demske et al., 2016). Factors driving environmental change at the site were primarily natural prior to c. 3950 cal yr BP (c. 2000 BC), after which time the observed changes were likely driven by human activity (Demske et al., 2016).

1.3 Research Objectives and Thesis Layout

The major objectives of this study are to: (1) develop a robust, well-constrained record of hydroclimate variability for the mid- to late Holocene for the Garhwal Himalaya utilizing non-destructive analyses of a sediment core recovered from Deoria Tal, Uttarakhand; and (2) assess the correspondence of the timing of the abandonment of established settlements along the lower reaches of Indus-Ghaggar and Saraswati River Valleys with hydroclimate variability during the mid- to late Holocene, paying particular attention to the interval between 5000 and 3000 cal yr BP. Accordingly, the thesis is organized into three chapters. The first chapter introduces the research and its motivation and describes the study area. The second chapter, which is formatted to be a publishable manuscript, focuses on the connection between hydroclimate variability, the 4200 cal yr BP event, and Harappan Metamorphosis (Giosan et al., 2018). The third chapter summarizes the major findings of the research project and describes potential avenues for future research. References for the entire thesis are found at the end of the thesis. Three appendices describe the process/approach utilized in prepping the sediment core for XRF, X-Ray and CT scans.

1.4 Figures

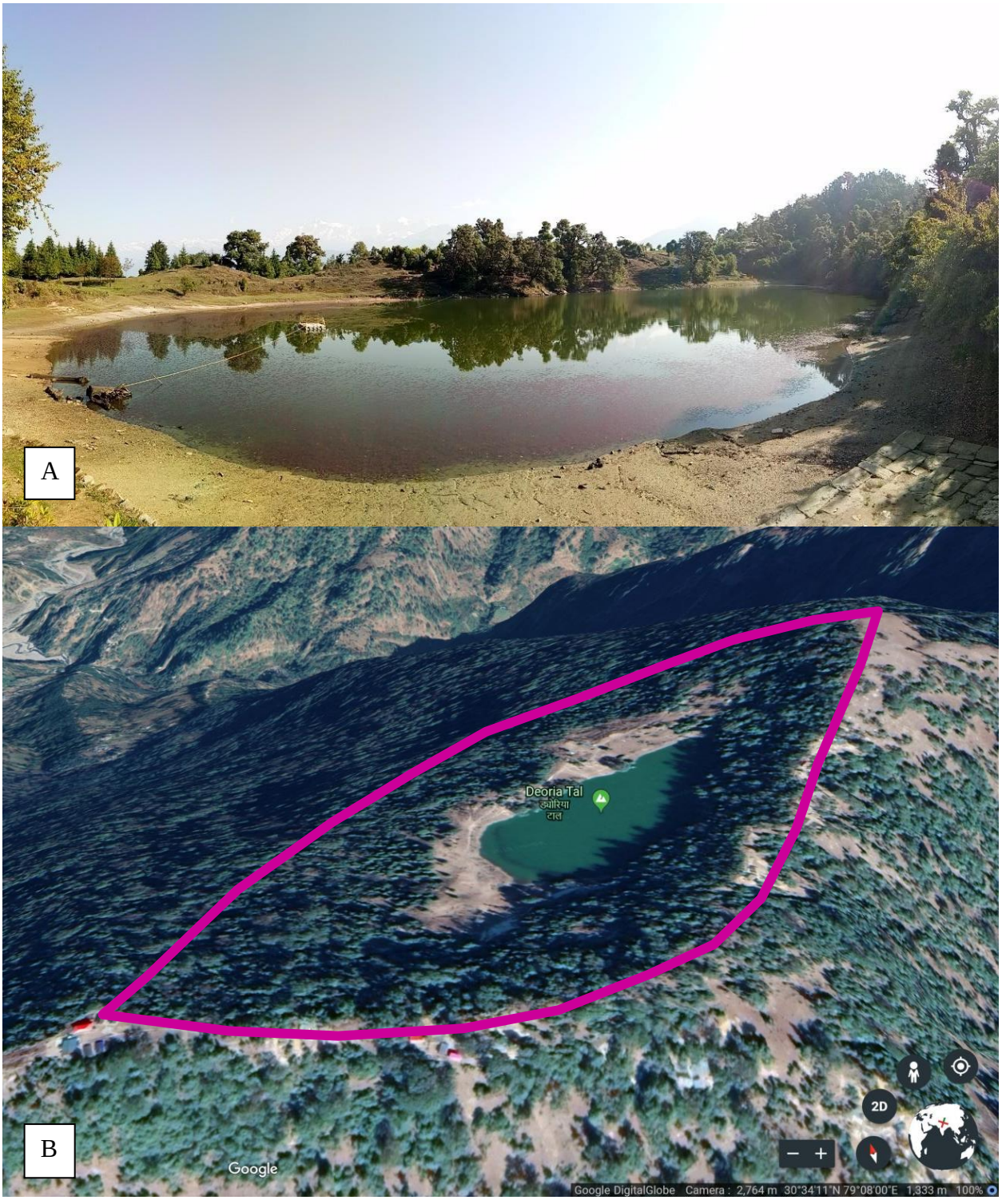
A
B
Deoria Tal
Google
2D
Google DigitalGlobe Camera : 2,764 m 30°34'11"N 79°08'00"E 1,333 m 100%

Figure 1.1. Study area. (a) Photo of Deoria Tal illustrating the location of *Trapa* in the littoral of the lake, the coring platform, and the snow-covered peaks of the Himalaya in the background (Porinchu 2018, image). (b) Google Earth image (n.d.) of Deoria Tal with the closed basin catchment (11 ha) outlined in pink.

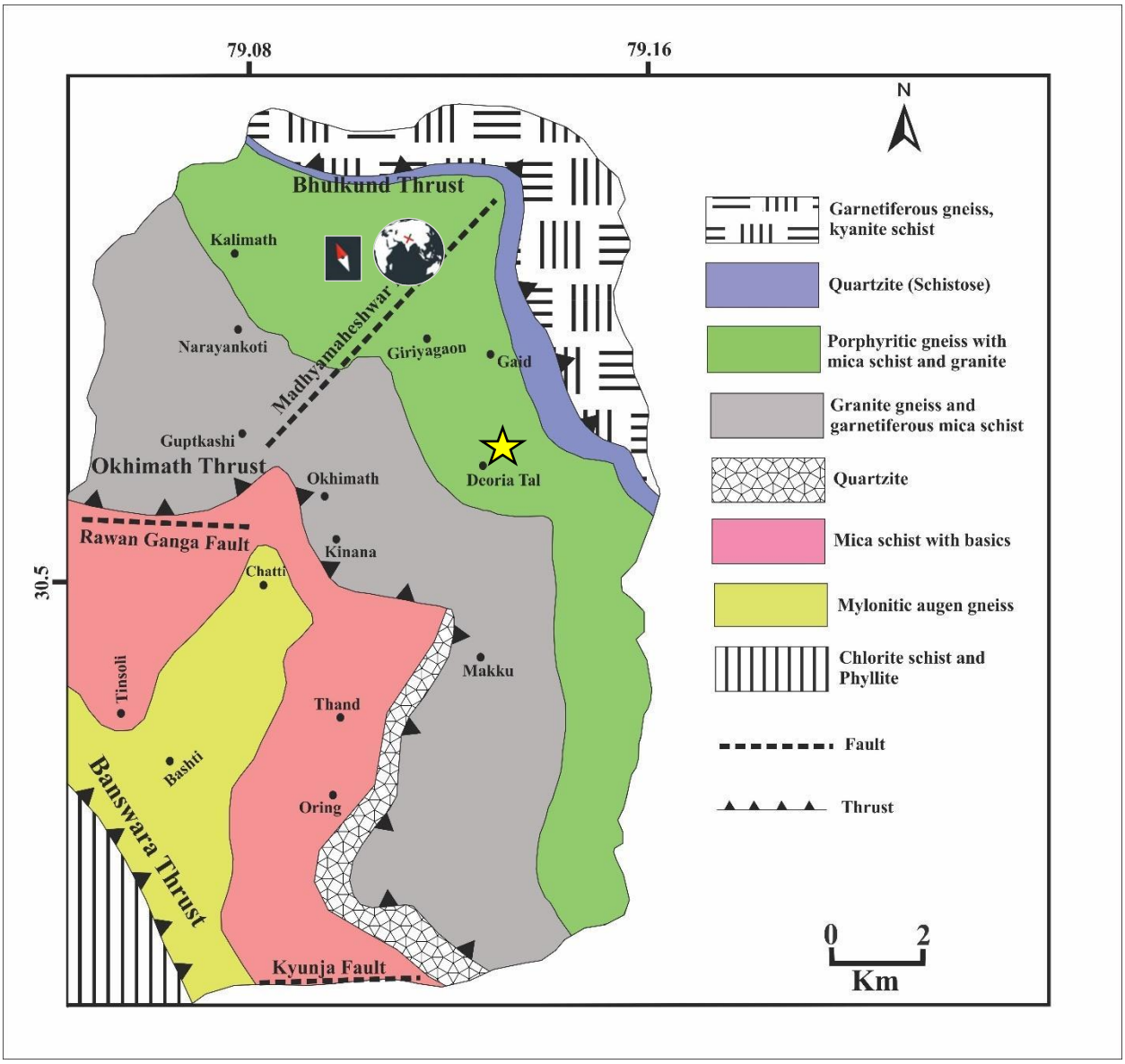

Figure 1.2. Map of the geological context for Deoria Tal. Geologic context for Deoria Tal (indicated with a yellow star) showing the high-grade metamorphic terrain (Chaudhary et al., 2010; Kotlia, 2019, personal communication). The lithotectonic groups present in the area are delineated by three thrusts. The first lithotectonic group is located adjacent to the Bhulkhund Thrust, the second is between the Bhulkhund Thrust and the Okimath Thrust, and the third is between the Okimath Thrust and the Banswara Thrust.

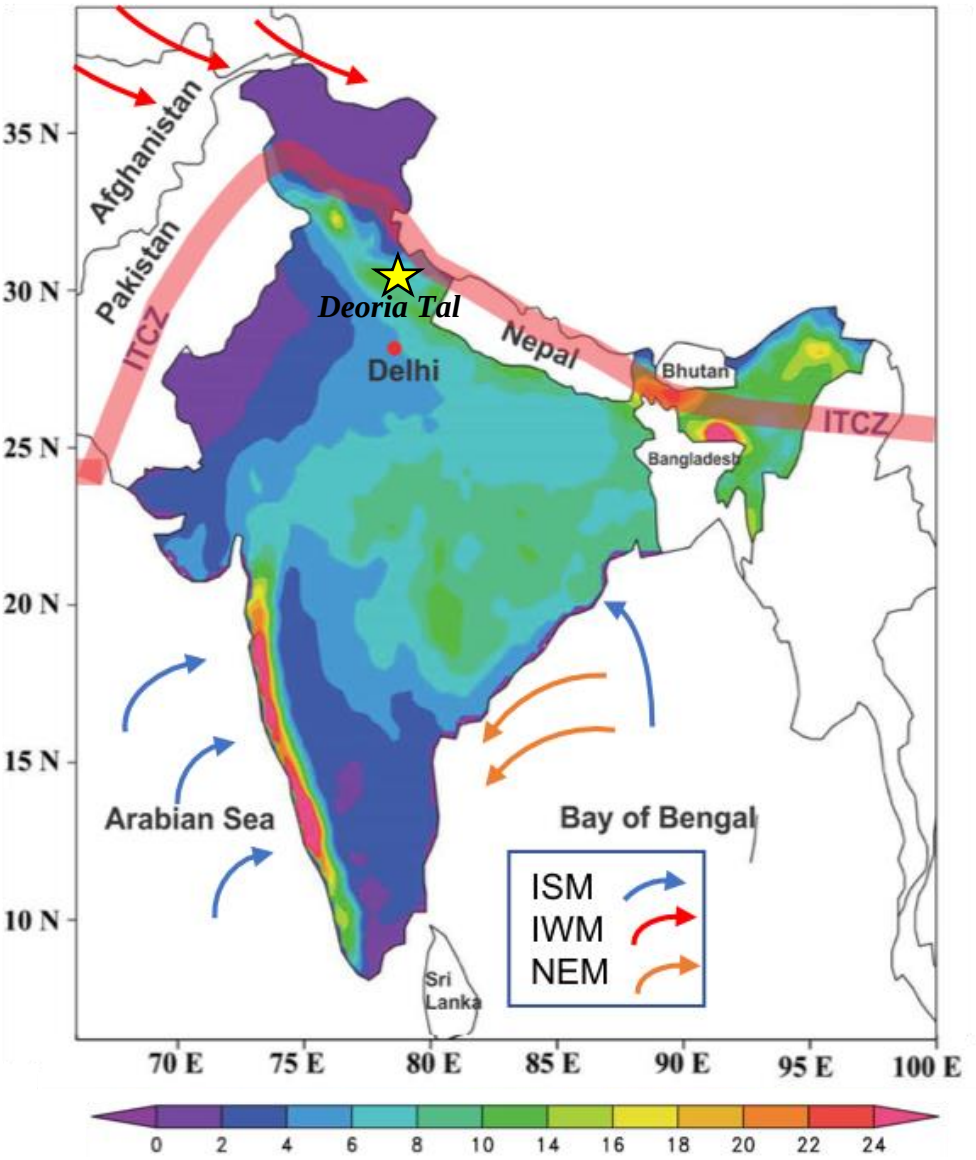

Figure 1.3. Climatological map of India. Modified after Patwardhan et al. (2016) with the choropleth designating the mean Indian Summer Monsoon (ISM) for summer precipitation (JJAS) based on 1951-2000 instrumental data in mm/day and the study location of Deoria Tal designated with a yellow star (base map provided by Dr. Anoop Singh). Arrows show the prevailing direction of the seasonal winds and associated precipitation, including ISM for Indian Summer Monsoon, IWM for Indian Winter Monsoon (Western Disturbances), and NEM for

Northeast Monsoon. The mean northern-most position of the Intertropical Convergence Zone (ITCZ) is highlighted in red.

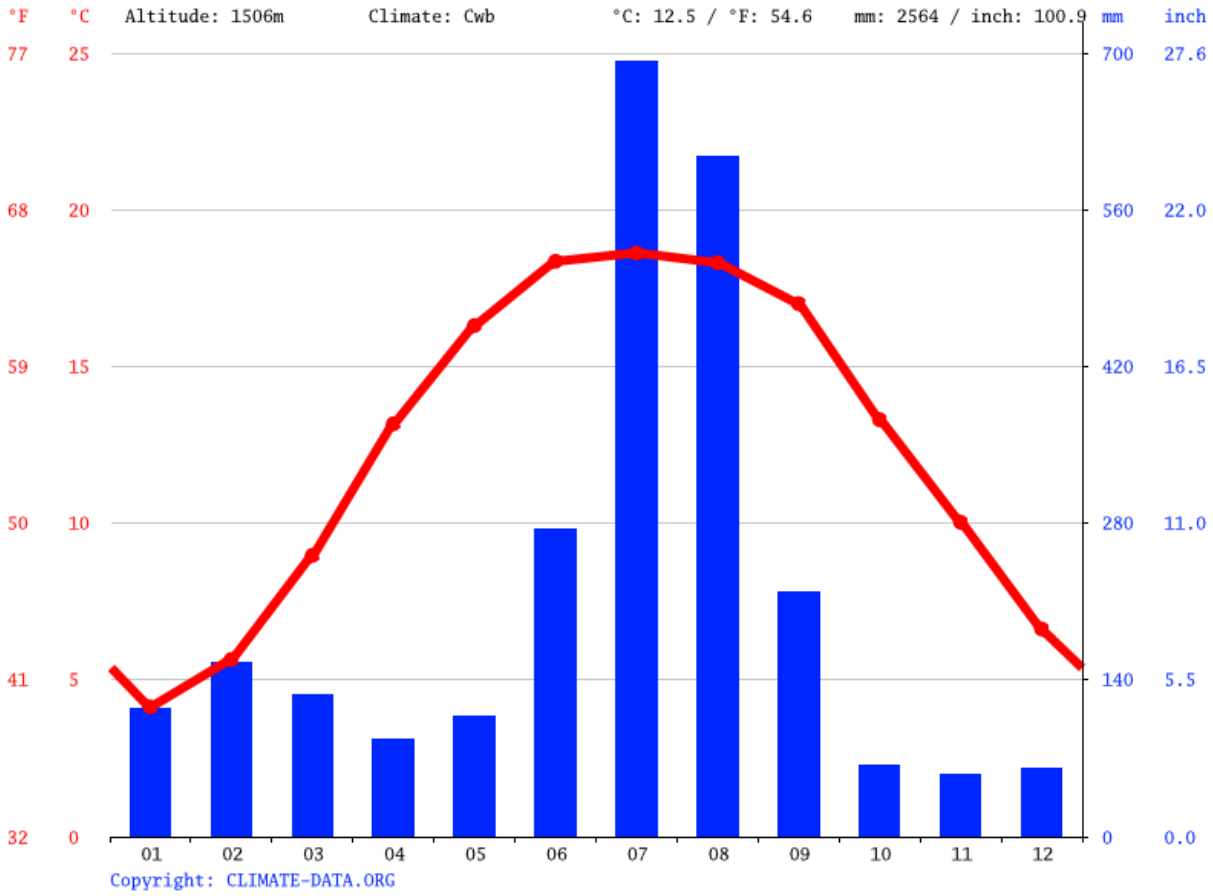

Figure 1.4. Climograph of Chamoli-Gopeshwar. Present time climatic data of monthly temperatures in (°F and °C; red) and precipitation (mm and inches; blue) for Chamoli-Gopeshwar (Climate-Data, n.d.).

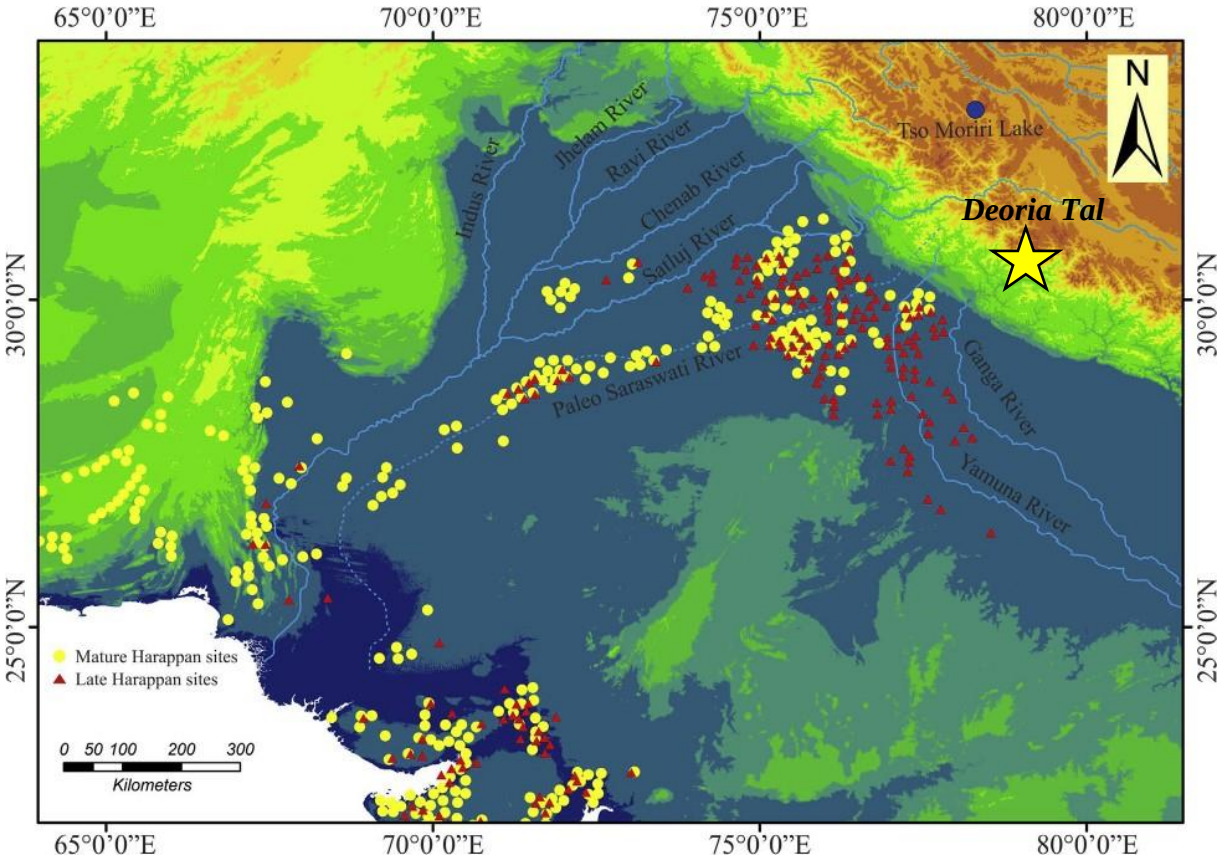

Figure 1.5. Harappan Civilization and Deoria Tal. Modified after Dutt et al. (2018), Deoria Tal is denoted with a yellow star. Yellow circles denote Mature Harappan sites and red triangles denote Late Harappan sites.

CHAPTER 2

EVIDENCE OF ABRUPT HYDROCLIMATE AND ENVIRONMENTAL CHANGE IN THE GARHWAL HIMALAYA, INDIA AT 4200 CAL YR BP COEVAL WITH HARAPPAN METAMORPHOSIS[1]

[1] Niederman, E.A., Porinchu, D.F., and Kotlia, B.S. To be submitted to *Scientific Reports.*

2.1 Abstract

High-resolution analysis of a 3.80 m long sediment core, recovered from Deoria Tal, a mid-elevation lake located at 2393 m a.s.l. in the Garhwal Himalaya of Uttarakhand, was undertaken to characterize long-term and abrupt climatic fluctuations in northern India during the mid- to late Holocene. Of particular interest is the potential link between abrupt climate change at 4200 cal yr BP and the onset of a stepwise decline of the highly complex Harappan civilization. A robust chronology, based on ten AMS ^{14}C dates, indicates that the core extends back to 5200 cal yr BP. Non-destructive, radiological imaging analyses, such as X-ray fluorescence (XRF), X-ray, and Computerized Tomography (CT) scans, were used to assess the response of the lake system to changing hydroclimatic conditions. Episodes of notable hydroclimate change, evidenced by variations in elemental concentrations and sediment density are centered at 4850, 4200, and 3100 cal yr BP. The 4850 and 4200 cal yr BP events were initially characterized by elevated detrital input, greater sediment density, and decreased lake ventilation, reflecting elevated lake level. The 3100 cal yr BP event was characterized by lower detrital flux, decreased sediment density, and increased oxygenation, reflecting lake drawdown. Strengthened Westerly Disturbances may account for the expansion of Deoria Tal between 4300 and 4100 cal yr BP, an interval associated with Harappan migration.

INDEX WORDS: India, paleoclimatology, lake sediment, 4200 cal yr BP event, Harappa, X-ray fluorescence (XRF), Computerized Tomography (CT), radiography, abrupt climate change, non-destructive imaging

2.2 Introduction

A number of researchers have proposed that the 4200 cal yr BP megadrought, which extended from 4200 to 3900 cal yr BP, is characterized by a reduction in the global monsoon and associated circulation systems, leading to droughts and seasonal precipitation failures worldwide (Weiss, 2016). This event, which included a 30 – 50 % reduction in the strength of the Mediterranean Westerlies (Weiss, 2016) and a widespread drought over much of the interior of North America (Booth et al., 2005), also impacted Asia. Weiss (2016) noted that the East Asian Summer Monsoon (EASM) and the Indian Summer Monsoon (ISM) experienced periods of weakening in eastern China, Inner Mongolia, and India, "synchronous" with the 4200 cal yr BP event. Given that the EASM and the ISM are the main sources of precipitation for their respective regions, climate scientists and archaeologists have postulated that a dramatic reduction in precipitation at 4200 cal yr BP would have impacted the complex societies present in India and China during the mid- to late Holocene.

At 4200 cal yr BP, northern India was occupied by the well-established Harappan or Indus Valley Civilization. The Harappa, or the Indus River Civilization, was a socially complex, agrarian, and highly urbanized civilization located along the Indus and Ghaggar-Hakra river valleys, with technological advancements including bathrooms served by sewer systems (Bryson and Murray, 1977; Winner, 2012). During the Late Mature phase (between 4500 and 3900 cal yr BP; Leipe et al., 2014), the Harappan civilization was characterized by extensive infrastructure including large cities with extensive sanitation facilities (Schug et al., 2013) and agricultural and water delivery systems heavily reliant on hydraulic engineering (Wright et al., 2008). The distinguishing characteristic of the Late Mature phase is it includes the onset of the Harappan civilization's "collapse" or "metamorphosis", which involved demographic contraction and

extensive de-urbanization coinciding with eastward migration (Staubwasser et al., 2003; Madella and Fuller, 2006; Giosan et al., 2012; Giosan et al., 2018). However, the specific causes of the Harappa Civilization's demise are hotly debated with explanations invoking climate variability (Ponton et al., 2012), changes in social processes (Madella and Fuller, 2006), some mixture of the two (MacDonald, 2011; Giosan et al., 2012; Schug et al., 2013; Sarkar et al., 2016), or a re-organization of the river network (Chatterjee and Ray, 2017).

Researchers have linked inferred changes in hydroclimate at 4200 cal yr BP with the onset of the Harappan decline (Staubwasser et al., 2003; Giosan et al., 2018; Giesche et al., 2019). Most of the existing studies have focused on reconstructing the ISM, as the ISM is the main source of precipitation for the region occupied by the Harappa and therefore critical to this agrarian society. These studies include lake sediment-based reconstructions from northern India (Prasad et al., 1997; Sharma and Gupta, 1997; Enzel et al., 1999; Chauhan and Sharma, 2000; Sharma et al., 2000; Wünnemann et al., 2010; Leipe et al., 2014; Menzel et al., 2014; Chauhan et al., 2015; Demske et al., 2016; Saxena and Singh, 2017; Tripathi et al., 2017), marine sediment records from the Arabian Sea and Bay of Bengal (Ponton et al., 2012; Bolton et al., 2013; Ankit et al., 2017; Giosan et al., 2018), tree rings (Singh et al., 2017), and stalagmites (Sanwal et al., 2013; Kotlia et al., 2015; Kotlia et al., 2017). Other approaches include making use of $\delta^{18}O$ from animal teeth to derive paleoclimate signals (Sarkar et al., 2016), relating climatologically driven fluvial dynamics to settlement locations (Rajani and Rajawat, 2011; Giosan et al., 2012; Chatterjee and Ray, 2017) and inferring climate based on agricultural requirements (Wright et al., 2008; Farooqui et al., 2013).

This study is motivated by the correspondence of the timing of the megadrought at 4200 cal yr BP with the onset of Harappan deurbanization and shifts in agricultural strategies

beginning at 4200 cal yr BP (Madella and Fuller, 2006) and the eastward migration of Harappan settlements that occurred between c. 5000 and c. 4000 cal yr BP (Gupta et al., 2006). Here, I present a high-resolution (decadal-scale) reconstruction of hydroclimate variability between 5200 and 180 cal yr BP, with a specific focus on the interval between 5200 and 3000 cal yr BP, which spans the interval when the Harappa flourished and declined. I make use of non-destructive, radiological approaches, i.e. X-ray fluorescence (XRF), X-Ray Imaging, and Computerized Tomography (CT) scans of a well-dated lake sediment core recovered from Deoria Tal, a small, closed basin lake located in the Garhwal Himalaya to: (1) characterize regional hydroclimate variability; (2) determine if evidence of an abrupt, short-lived climate event at 4200 cal yr BP is present at this site; and (3) determine whether there is a correspondence between regional hydroclimate variability during the late Holocene and Harappan metamorphosis.

2.3 Study Site

Deoria Tal (Lake) (30.5222° N, 79.1277° E) is located on a hilltop (2393 m a.s.l.) in the northern Indian state of Uttarakhand, above Okhimath (alt. spelling Ukhimath) and 3 km from Sari Village in the Rudraprayag District (Figure 2.1). Deoria Tal has a surface area of 2.7 ha, a closed catchment area of 11 ha, and a central lake depth of 16 m. The lake is situated in a high-grade metamorphic terrain above the Main Central Thrust (MCT) zone in the Garhwal Himalaya and is underlain by three major lithotectonic groups (Bist and Sinha, 1980; Chaudhary et al., 2010) (Figure 2.2). The lithotectonic groups are delineated by three main thrusts—Bhulkund Thrust, Okhimath Thrust, and Banswara Thrust (from north to south). Deoria Tal is located between the Bhulkund Thrust and the Okhimath Thrust and is characterized by a geology consisting of porphyritic gneiss with mica schist and granite (Chaudhary et al., 2010). The

formation of the lake basin likely resulted from tectonic activity (Kotlia, 2019, personal communication).

Lying south of the mean northern-most position of the Intertropical Convergence Zone (ITCZ), the major source of precipitation for Deoria Tal is the ISM (Figure 2.3) with the average annual rainfall totaling around 200 cm (Sharma et al., 2000). ISM-related rainfall (ISMR) occurs between June to September (Dixit and Tandon, 2016; Goswami and Chakravorty, 2017) and typically ranges between 8 and 10 mm/day (Paatwardhan et al., 2016). However, Deoria Tal can receive additional precipitation from extra-tropical cyclones, also known as Western Disturbances or the Indian Winter Monsoon (IWM), between December and February (Dimri et al., 2016). During the winter months, Deoria Tal can be covered in ice, but snowfall in the immediate area is relatively rare (Sharma et al., 2000).

The vegetation currently surrounding Deoria Tal includes *Quercus semecarpifolia* (Oak) dominated temperate forests with *Rhodendron arboretum*, *Alnus nepalensis* (Alder), *Ulmus wallichtana* (Elm) also present (Sharma and Gupta, 1997; Sharma et al., 2000). Shrubby elements include *Rubis* spp., *Berberis chirta*, etc. with ground cover elements including *Tridax incumbeus*, *Cynoglossum* spp., *Thalictrum foliosum*, and other grasses. A mat of water chestnut (genus: *Trapa*), with the characteristic habitat of relatively shallow (0.3 — 3.6 m), nutrient rich water (Hummel and Kivat, 2004), covers the littoral of Deoria Tal. The vegetation community in the Deoria Tal catchment has remained relatively stable, with evidence of only three major shifts in vegetation occurring during the late Holocene (Sharma et al., 2000). Deoria Tal was surrounded by a temperate oak forest consisting of oak, elm, and alder between 4000 and 3200 cal yr BP (Sharma et al., 2000). The composition of the vegetation community likely reflects the existence of cool, moist conditions during this interval. The reduction in oak and an increase in

the relative abundance of grasses at 3200 cal yr BP is inferred to reflect the onset drier conditions, which lasted until c. 1700 cal yr BP. However, it is important to note the reduction in the abundance of oak between 3200 and 1700 cal yr BP may be associated with its selective logging by local inhabitants. The presence of charcoal along with elevated amounts of ruderal plant taxa, e.g., Brassicaaceae, Chenopodiaceae/Amaranthaceae, *Artemisia*, and Asteraceae, may reflect human activity within the catchment.

Human impact on the lake system currently is limited as it is protected by the Uttarakhand Forestry Department, but historically, human influence is potentially quite variable. The Harappa started migrating eastward through the Ganga plain at c. 5000 cal yr BP (Gupta et al., 2006). The proximity of the Harappan civilization to Deoria Tal is illustrated in Figure 2.4 with known Mature Harappan and Late Harappan settlements denoted (Dutt et al., 2018). Of note, Demske et al. (2016) noted from their lake sediment pollen analysis of a nearby site, Dewar Tal, that migrants may have arrived in the region at c. 4000 cal yr BP. Other evidence of human influence includes the presence of the well-documented Painted Grey Ware (PGW) culture and large-scale cultivation between 2000 and c. 1300 cal yr BP in the region (Demske et al., 2016).

2.4 Materials and Methods

2.4.1 Core Recovery and Stratigraphic Record

A sediment core was recovered from the central basin of Deoria Tal in May 2018 using a modified Livingstone corer, deployed from a platform, at a depth of 5.65 m (Figure 2.1A). The core consists of five overlapping drives with a total composite core length of 380 cm. The uppermost sediment was recovered using a plastic tube to ensure that the flocculent surface sediment was captured with minimal disturbance while the stiffer lower sediment was recovered using a stainless-steel barrel. Limnological measurements were made and water samples for

water chemistry were also collected at this time. Stratigraphical notes were made in the field and later at Kumaun University (KU), Nainital, where each drive was longitudinally split and photographed. The stratigraphic description of the core includes changes in color, qualitative estimates of grain size, and organic content. Samples for radiocarbon dating were removed, bagged, and labeled at KU. Core compression was accounted for during sub-sampling by creating a ratio between the original length of the core (measured in the field) and the length of the core measured in the lab. The adjusted sample depths are based on the application of this ratio to the core. The presence of a distinct sand lens in drive LC1C was also used to help establish the adjusted core depths.

2.4.2 Dating

Ten *Trapa* seed cases (Figure 2.5) were extracted from the sediment core. Additionally, a seed case from *Trapa* currently extant in Deoria Tal was also dated to determine if 'old' carbon or a reservoir effect was present. The samples used for radiocarbon dating were rinsed in deionized water, bagged, and labeled before being submitted for analysis at the Center for Applied Isotope Studies (CAIS) at the University of Georgia. The radiocarbon dates for the samples were determined using accelerator mass spectrometry (AMS) and were converted to calendar years using OxCal 4.3 (Bronk Ramsey, 2017) with the reported 2σ age ranges following Reimer et al. (2013) (Table 1). An age-depth model, based on ten ^{14}C dates, was developed using BACON (Bayesian Accumulation Model; Blaauw and Christen, 2011), an open-source R code package (Figure 2.6).

2.4.3 X-Ray Fluorescence (XRF)

Preparation of the cores for elemental analysis using X-ray fluorescence (XRF) was completed at the Environmental Change Lab at the University of Georgia and it involved

establishing a flat planar surface along the longitudinal axis of each core drive. The sediment cores were scanned using a Bruker Tracer 5i mounted portable XRF (pXRF) with a rhodium tube source at CAIS. As outlined by Hunt and Speakman (2015) two parameter settings were utilized. To detect elements with a low atomic number (Z) a 60 second exposure time of 20 keV, 35 amps, and no filter was employed. To detect high Z elements, a 60 second exposure time of 40 keV, 35 amps, and a Cu 100 µm: Ti 25 µm: Al 300 µm filter was employed. The pXRF measurements were scanned at a 0.2 mm interval, but were adjusted to account for core shrinkage. The spectra were parsed utilizing a custom Python script before processing in the Bruker Artax software for elemental identification and exported into Microsoft Excel. Elemental data from the pXRF analysis were normalized using the rhodium Kα peak to minimize the noise variation of the Compton peak. To distinguish natural variation from anthropogenic influence the resultant time-series spectra were normalized using the aluminum Kα record (Elder, 1988; Nakamura et al., 2016). A series of Spearman's correlations implemented in R, were used to determine the significance, direction, and magnitude of correlations in the variations of the elemental returns for the 10 elements that were detected in the pXRF analysis following Haenssler et al. (2013) and others (Olsen et al., 2010; Heymann et al., 2013). This nonparametric approach was utilized to account for the possibility that the sampling of a heterogenous sediment matrix would result in an error distribution that was not normally distributed (Hunt and Speakman, 2015). Principal component analysis (PCA) was utilized to identify which of the elements could account for a statistically significant amount of variance along a reduced number of environmental axes (Olsen et al., 2010; Hahn et al., 2014; Hendy et al., 2015; Chassiot et al., 2018). All statistical analyses were undertaken in R.

Hydroclimatic regimes can influence the allogenic processes responsible for influencing the detrital flux, which results from weathering and overland flow processes within a catchment, to a lake. Typically, during a wetter regime, an elevated flux of coarse-grained sediment will enter the lake (Cuven et al., 2011; Bohra and Kotlia, 2015). As a means to distinguish anomalous climatic conditions in lacustrine records, general associations have been identified between specific elements, identified by XRF, and grain size at numerous sites in varying geologic settings and hydroclimatic conditions (Davies et al., 2015). Elements associated with fine grained sediment include potassium (Olsen et al., 2010; Wünnemann et al., 2010; Cuven et al., 2011; Haenssler et al., 2013; Heymann et al., 2013; Hahn et al., 2014; Chassiot et al., 2018), titanium (Olsen et al., 2010; Wünnemann et al., 2010; Haenssler et al., 2013; Heymann et al., 2013; Olsen et al., 2013; Chassiot et al., 2018; Peng et al., 2019; Schmidt et al., 2019), manganese (Hahn et al., 2014; Chassiot et al., 2018), and rubidium (Haenssler et al., 2013; Hahn et al., 2014; Chassiot et al., 2018). Elements associated with coarse grained sediment include silicon (Wünnemann et al., 2010; Cuven et al., 2011; Haenssler et al., 2013; Heymann et al., 2013; Hahn et al., 2014; Schmidt et al., 2019) and zirconium (Haenssler et al., 2013; Heymann et al., 2013; Chassiot et al., 2018).

Existing grain size-element associations enable the development of specific elemental ratios that further aid environmental interpretation of hydroclimate climatic variability. The Zr/Rb ratio (Heymann et al., 2013) and the Zr/K ratio (Cuven et al., 2011) have been used to distinguish grain size, with a larger ratio indicative of a larger grain size. This interpretation is based upon zirconium's association with large grain-sized zircon crystals (Haenssler et al., 2013; Heymann et al., 2013; Chassiot et al., 2018), while rubidium (Haenssler et al., 2013; Hahn et al., 2014; Chassiot et al., 2018) and potassium (Olsen et al., 2010; Wünnemann et al., 2010; Cuven

et al., 2011; Haenssler et al., 2013; Heymann et al., 2013; Hahn et al., 2014; Chassiot et al., 2018) are typically associated with the small, clay-sized fraction of lacustrine sediment. However, this relationship is dependent on the source material. For example, the presence of K feldspars in the catchment may result in elevated levels of potassium and rubidium, which reflect an increase in the flux of coarse-grained sediment rather than fine-grained sediment (Heymann et al., 2013; Cherkashina et al., 2014).

Thorium is not commonly used in paleoenvironmental XRF-based studies, however Hunt and Speakman (2015) demonstrated that thorium is measurable by pXRF, and was therefore a potentially useful element to measure in the Deoria Tal sediment core. Other studies have demonstrated that thorium concentrations can be established using XRF. Xi et al. (2018) determined the amount of thorium in zircon crystals, which would potentially suggest a grain size association, with larger particles corresponding to the presence of zirconium (Haenssler et al., 2013; Heymann et al., 2013; Chassiot et al., 2018). However, An et al. (2018) measured thorium using XRF to assess the sediment matrix background in preparation for OSL dating, and found higher concentrations of thorium associated with smaller mean grain sizes. In this study, thorium is not associated with a particular grain size fraction, rather the interpretation of variations in thorium follows existing studies, where elements such as calcium (Cuven et al., 2011; Haenssler et al., 2013; Heymann et al., 2013; Hahn et al., 2014; Chassiot et al., 2018), iron (Cuven et al., 2011; Haenssler et al., 2013; Heymann et al., 2013; Olsen et al., 2013; Hahn et al., 2014; Nakamura et al., 2016; Chassiot et al., 2018), and strontium (Olsen et al., 2010; Cherkashina et al., 2014; Chassiot et al., 2018) are interpreted to reflect detrital input but are not associated with the delivery of sediment of a specific grain size to the lacustrine system.

Measured elemental abundances are also associated with authigenic influences on lacustrine systems. Silicon, in particular, can be sourced biogenically as it is a primary component of biogenic silica (Heymann et al., 2013). Calcium can also be strongly correlated with silicon in certain settings (Hahn et al., 2014). Differentiating between detrital and biogenically sourced silicates, which can be done by identifying intervals characterized by lack of correlation between elements that can biologically-sourced (e.g., silicon and calcium) from those that are not (e.g., potassium, titanium, manganese, iron, rubidium, strontium, and zirconium) can serve as a proxy for biogenic silica (Olsen et al., 2010; Fritz et al., 2018).

Hypolimnetic oxygen conditions are often reconstructed using iron (Wünnemann et al., 2010) and manganese (Haenssler et al., 2013; Heymann et al., 2013). The relative abundance of iron and manganese is influenced by redox potential in the benthic zone of aquatic systems (Cuven et al., 2011; Heymann et al., 2013; Olsen et al., 2013; Hahn et al., 2014; Nakamura et al., 2016), which in turn is influenced by hypolimnetic oxygen conditions. Although pH can be a confounding factor (Olsen et al., 2013), manganese is typically retained in lake surface sediment under oxic conditions as iron is mobilized into the bottom waters due to it having a higher redox potential, whereas the reverse is true under dysoxic/anoxic conditions. The relationship between iron, manganese, and redox potential has facilitated the development of reconstructions of hypolimnetic oxygen conditions (Heymann et al., 2013). A low Fe/Mn ratio is indicative of oxic bottom waters and higher ratio suggests the existence of dysoxic/anoxic conditions. There are conditions where the Fe/Mn ratio should not be used as a proxy of redox conditions. For example, Hahn et al. (2014) determined that the presence of high amounts of phosphate, found in vivianite, basaltic rock, and pumice as is typical in a volcanic region, can influence Fe/Mn. Deoria Tal, however, is located in a largely metamorphic region, so the Fe/Mn ratio redox signal

is not anticipated to be perturbed. However, caution should be used as variations in detrital flux rather than changes in redox potential, could be driving manganese (Hahn et al., 2014) and iron (Cuven et al., 2011; Haenssler et al., 2013; Heymann et al., 2013; Olsen et al., 2013; Nakamura et al., 2016) availability. However, in some instances, differentiation between redox potential versus detrital influx can be determined within an individual core for manganese (Chassiot et al., 2018) and iron (Han et al., 2014; Chassiot et al., 2018). To distinguish between the primary sourcing processes of manganese, Nakamura et al. (2016) used the lack of a correlation with titanium to determine that the source of manganese was not terrigenous in origin. It is important to note that hypolimnetic oxygen concentrations and redox potential can also be influenced by lake level fluctuations, wind stress and/or photosynthetic activity within the lake (Heymann et al., 2013).

2.4.4 X-Ray Imaging

Traditional medical X-ray images or X-radiographs were completed at the University of Georgia Veterinary Teaching Hospital's Radiology and Imaging Department on a SEDECAL table with the radiograph processing software being Canon CXDI Control Software NE. Each core drive was imaged using a fixed table height with two exposure settings: Rt Extremity Lateral (75 kV, 200 mA) and Abdomen VD (80 kV, 400 mA). This analysis provided grayscale, longitudinal images along the coronal axis, which were used to refine the stratigraphy of the core (Zaragosi et al., 2006; Sáez et al., 2009; Francus et al., 2015). The grey-level values of the sediment in the X-radiographs are a result of the X-ray attenuation to the sediment, which is controlled primarily by bulk sediment density (St-Onge et al., 2007; Francus et al., 2015). Bulk sediment density in turn is influenced by factors including granularity (grain size) and composition (e.g., organics, silicates, etc.) (St-Onge et al., 2007; Francus et al., 2015). As the

resultant X-radiographs were not quantitatively corrected for possible distortion and stitching errors, the X-radiographs were primarily used to identify the location of embedded *Trapa* seed cases in the core.

2.4.5 Computerized Tomography (CT) Scans

Computerized Tomography (CT) scans, also known as Computerized Coaxial Tomography (CAT) scans (Francus et al., 2015), were completed at the University of Georgia Veterinary Teaching Hospital's Radiology and Imaging Department on a Siemens Sensation 64 CT scanner with Syngo WinNT 5.1 Service pack 3 imaging processing software. Each core drive was imaged axially with two different exposure settings: Soft (40 window level; 300 window width) and Bone (400 window level; 4000 window width). The result was a series of images or tomograms, which are cross sectional images perpendicular to the length of the core (Francus et al., 2015). The tomograms were compiled using a MATLAB™ package (Reilly et al., 2017). The SedCT software (Reilly et al., 2017) produces four main outputs: CT number, pixel count, standard deviation, and a compiled coronal axis image (reconstructed topogram). CT scans also are based on measuring X-ray attenuation as with X-radiography; however, CT scans are not susceptible to the sample thickness contributing to the grey-level values (Francus et al., 2015). Instead, CT scans use CT numbers which is the number of Hounsfield Units (HU), calculated according to Equation 1, where μ_{water}= 0 HU and μ_{air}= -1000 HU (Reilly et al. 2017), as a

Eqn. 1

$$HU = 1000 \times \frac{\mu_{sample} - \mu_{water}}{\mu_{water} - \mu_{air}}$$

measure of radiodensity calibrated according to the Hounsfield Scale. HU numbers (or CT numbers) are influenced by bulk sediment density, mineralogy, and porosity (St-Onge et al., 2007; Francus et al., 2015) and therefore CT scans can be used to identify internal structure

within sediment for paleoenvironmental interpretation (Flisch and Becker, 2003; Fouinat et al., 2017). Presentation of the CT scan HU data will be limited to the Soft CT settings output; the Bone setting will not be discussed due to the Bone setting having higher signal-to-noise variability.

2.5 Results

2.5.1 Chronology

The radiocarbon analysis indicates that the lake sediment was deposited in stratigraphic order (Table 2.1). The age-depth model, developed in BACON, indicates that the base of the sediment core extends back to c. 5200 cal yr BP (Figure 2.6). The modern *Trapa* sample returned a modern radiocarbon date with a pMC equal to 101.9, which, when input into OxCal with the Bomb NH 13 curve, results in a calibrated calendar date range between 1955.48 – 1957.44 AD. The bomb curve only extends to 2010 AD, which accounts for the date obtained on the modern *Trapa* seed case (Hadden, 2021, personal communication). As a result, the dates obtained on the *Trapa* seed cases were not corrected for a reservoir effect. A notable increase in the sedimentation rate occurs at 2100 cal yr BP. The average sedimentation rate from c. 5200 to 2100 cal yr BP was 30.0 yr/cm; whereas, it was 7.3 yr/cm from 2100 cal yr BP to present.

2.5.2 Chemostratigraphy

The results of a PCA of the elemental data were used to divide the core into four distinct zones: DRL-1 (380 – 318 cm; 5200 – 3000 cal yr BP), DRL-2 (318 – 256 cm; 3000 – 1500 cal yr BP), DRL-3 (256 – 169 cm; 1500 – 800 cal yr BP), and DRL-4 (169 – 50 cm; 800 – 180 cal yr BP) (Figure 2.7). The stratigraphy (PT and LC1A-D; Table 2.2; Figure 2.8A-D), PCA results, pXRF data (termed elemental signatures and ratios; Figures 2.9 and 2.10), HU number (Figure 2.11), and radiological imagery (Figures 2.12A-B, 2.13A-D), will be summarized by zone.

Figure 2.9 depicts the results from the pXRF, which is comprised of ten different elemental signatures: silicon Kα, potassium Kα, calcium Kα, titanium Kα, manganese Kα, iron Kα, rubidium Kα, strontium Kα, zirconium Kα, and thorium Lα (from here referenced by the respective elemental symbol). The Spearman's correlation coefficients indicate the existence of a statistically significant correlation between all the elements (Figure 2.14). Of note are the strong Spearman's correlation coefficients between Th and Rb ($\rho^2 = 0.92$), Sr ($\rho^2 = 0.89$), and Zr ($\rho^2 = 0.90$).

The results of a PCA for the ten elemental signatures (Figure 2.9) and two elemental ratios (Figure 2.10) correspond to the results from the Spearman's correlation (Figure 2.14). However, the results of the initial PCA-based exploratory screening identified that Si, Ca, and the Zr/Rb ratio did not correspond with the other elements and thus these elemental measures were not included in further statistical analyses. A PCA limited to the remaining eight elements and Fe/Mn, indicated that approximately 90 % of the variance in the dataset could be explained by the first two principal component axes (Figure 2.15). PCA Axis 1, which captured 78 % of the variance in the elemental dataset, was strongly correlated with K, Ti, Fe, Rb, Sr, Zr, and Th. PCA Axis 2, which captured an additional 12 % of the variance, was strongly correlated with Mn and Fe/Mn. A plot of the PCA axes against time indicates notable deviations in the elemental data at 4850, 4200, and 3100 cal yr BP (Figure 2.7).

DRL-1 (380 – 318 cm; 5200 – 3000 cal yr BP) is characterized by dark brown, almost black sediment at 380 cm, lightening to light brown sediment with a strong presence of organics at 350 cm, and then shifts to brown, organic sediment from 347 to 320 cm (Figure 2.8A). The presence of a piece of gravel at 367 cm, leaf fragment at 334 cm, piece of wood at 327 cm, and *Trapa* seed cases at 372 and 329 cm was noted. The radiographs provide additional stratigraphic

information (Figure 2.13D). Dark grey bands occur at 376 cm and 372 cm, a light grey band is located between 370 and 367 cm, a thin white band occurs at 351 cm, and a broad white band is found between 350 and 347 cm. A *Trapa* seed case is located at 346 cm.

Elemental returns in DRL-1 are largely driven by variations in the elements strongly correlated with PCA Axis 1 (K, Ti, Fe, Rb, Sr, Zr, and Th) while smaller magnitude changes are evident in Si, Ca, and Mn through the early portion of this zone. Prominent fluctuations in the elemental counts occur at 4850, 4200, and 3100 cal yr BP, with a less pronounced event evident at 3500 cal yr BP. At 4850 cal yr BP the elements associated with PCA Axis 1 (K, Ti, Fe, Rb, Sr, Zr, and Th), in addition to Ca and Mn are elevated while there is a slight positive excursion in Si. At 4200 cal yr BP the PCA Axis 1 elements are elevated, while there are slight positive excursions in Si and Ca and a slight negative excursion in Mn. A minor increase in Si, K, Ca, Ti, Fe, Rb, Sr, and Zr is evident at 3500 cal yr BP. At 3100 cal yr BP, elevated element counts occur in Rb, Sr, Zr, and Th while a large positive excursion occurs in Si and negative excursions occur in K, Ti, and Fe. Notable deviations from the mean in the Zr/Rb ratio include peak negative excursions at 4600, 4200, 3500 and 3100 cal yr BP (Figure 2.10). The fluctuations in the Zr/Rb ratio are largely driven by the increase in Rb for all of the noted events. Fluctuations in Fe/Mn are largely driven by changes in Fe and include peak positive excursions at 4850, 4200, 4000, and 3500 cal yr BP; and peak negative excursions at 3400 and 3100 cal yr BP. The HU number is elevated at 4850, 4200, 3500, 3200, and 3000 cal yr BP (Figure 2.11); the HU number's standard deviation is elevated at 4200 cal yr BP.

The sediment comprising DRL-2 (318 – 256 cm; 3000 – 1500 cal yr BP) is primarily dark brown and organic. Gravel was present between 318 and 320 cm. *Trapa* seeds were extracted at 304 and 290 cm (Figure 2.C). The radiographs document the presence of discrete

stratigraphic sections within DRL-2: the sediment grades from dark to light grey with banding throughout from 320 to 280 cm, grades from grey to light grey between 280 and 259 cm, and is dark grey from 259 to 256 cm, with a thin smear of white sediment present at the base of this zone. Prominent stratigraphic markers consist of a dark band at 292 cm and a very light band at 319 cm (Figure 2.13C). *Trapa* seed case remnants were present at 274 cm. The PCA identifies notable shifts in elemental returns between 2100 and 2000 cal yr BP and from 1600 to 1500 cal yr BP, with the majority of elements loading positively on PCA Axis 1 and negatively on PCA Axis 2 between 3000 and 1500 cal yr BP. Similarly, the elemental returns include depressed counts at 2000 cal yr BP for all elements (Si, K, Ca, Ti, Mn, Fe, Rb, Sr, Zr, and Th) and elevated counts at 1500 cal yr BP for all elements except Si. Variations in the Fe/Mn ratio are largely driven by changes in Fe and include elevated values at 2100 and 1500 cal yr BP and a depressed value at 2000 cal yr BP. Fluctuations in the Zr/Rb ratio are largely driven by changes in Rb and include elevated values at 2900, 2800, and 2500 cal yr BP; elevated values between 1600 and 1500 cal yr BP; and a depressed value at 2600 cal yr BP. The HU number includes notable positive excursions at 2500 and 1500 cal yr BP and a negative excursion at 2100 cal yr BP.

DRL-3 (256 – 169 cm; 1500 – 800 cal yr BP) is composed primarily of dark brown, organic sediment with a light brown, clay layer found between 248 and 204 cm. Aquatic moss is present from 204 to 169 cm and *Trapa* seed cases were extracted at 252 and 189 cm (Figure 2.8B). The radiographs document the presence of distinct stratigraphic sections in DRL-3: a white layer from 256 to 253 cm, a grey layer from 253 to 215 cm, and sediment grading from dark to light grey between 215 and 169 cm. A white band is found at 245 cm in addition to white banding extending from 222 to 215 cm. Additionally, two stepwise shifts in color, from dark to light grey, occur at 196 and 181 cm. *Trapa* seed cases are found at 253 and 231 cm and

throughout the core from 215 to 169 cm (Figure 2.13B). The PCA identifies notable shifts in elemental returns at 1400, 1200, and 1000 cal yr BP in PCA Axis 1 and at 800 cal yr BP for PCA Axis 2. The majority of elements load negatively on PCA Axis 1 and PCA Axis 2 between 1500 and 800 cal yr BP, although the PCA Axis 1 score begins to increase at 1000 cal yr BP. Notable changes in the elemental record are evidenced by the negative excursion for all elements (Si, K, Ca, Ti, Mn, Fe, Rb, Sr, Zr, and Th) throughout DRL-3 and elevated counts at 800 cal yr BP for Mn. Fluctuations in the Fe/Mn ratio are largely driven by changes in Fe throughout DRL-3 and include elevated values at 1400, 1100, and 800 cal yr BP and negative excursions from 1100 to 900 cal yr BP and at 800 cal yr BP. The Zr/Rb ratio values are largely driven by changes in Rb throughout DRL-3 and include highly variable values, with a notably elevated value at 1100 cal yr BP. Fluctuations in the HU number include a negative excursion between 1500 and 1000 cal yr BP and elevated values at 1400 and 1200 cal yr BP.

The sediment in DRL-4 (169 – 50 cm; 800 – 180 cal yr BP) initially consists of dark brown, organic, and clay rich sediment; at 122 cm the color grades to light brown, organic, and clay rich sediment. The uppermost sediment that was extracted via the plastic tube (PT) consisted of brown gyttja with the sediment transitioning from dark brown organic sediment to moderately brown organic sediment at 81.67 cm. Discrete layers of well-preserved aquatic moss are found between 97 and 110 cm; 122 and 144 cm; and 159 and 169 cm (Figure 2.8A). *Trapa* seed cases were found at 163, 117.5, 89.67, and 61 cm. The radiographs document the presence of many discrete stratigraphic groupings in DRL-4. The PT sediment consisted of a marbled light grey sediment from 95 to 91 cm, moderately grey grading to dark grey sediment between 91 and 82 cm, gray sediment between 82 and 77 cm, sediment that graded from white to grey between 77 and 75 cm, white marble appearing sediment from 75 to 66 cm, grey sediment between 66

and 55 cm, and dark grey sediment between 55 and 50 cm. A discrete stratigraphic marker consisting of a thin white and black band of sediment is found at 82 cm (Figure 2.12A-B). The sediment comprising LC1A grades from dark to light grey from 169 to 141 cm, is grey from 141 to 107 cm and light grey from 107 to 70 cm. Discrete stratigraphic bands consisting of: light grey sediment occurs at 115 cm; dark brown sediment occurs at 107, 100, 88, and 70 cm; and darker grey sediment, bordered by lighter colored bands at 107 and 100 cm (Figure 2.13A). The entirety of LC1B (169-165 cm) in DRL-4 is composed of light grey sediment. *Trapa* seed cases can be found in LC1B from 169 to 165 cm; in LC1A at 162, 157, 147, 145, from 138 to 120, 112, 107, and 71 cm; and in the PT at 84, 79, 76, 73, and from 66 to 55 cm (Figure 2.13B). The PCA identifies notable shifts in elemental returns in PCA Axis 2 at 300 cal yr BP, with the majority of elements loading positively on PCA Axis 1 between 800 and 180 cal yr BP. Fluctuations in elemental returns include a positive excursion for all elements (Si, K, Ca, Ti, Mn, Fe, Rb, Sr, Zr, and Th) extending from 800 to 180 cal yr BP. The Fe/Mn ratio, which includes a positive excursion from 800 to 600 cal yr BP, reaches a core maximum at 600 cal yr BP. The elevated Fe/Mn value is largely driven by changes in Fe. The negative excursion from 600 to 180 cal yr BP is largely driven by changes in Mn. The Zr/Rb ratio values are largely driven by changes in Zr throughout DRL-4 and include a sudden, positive excursion from 500 to 400 cal yr BP and a negative excursion from 400 to 180 cal yr BP. Fluctuations in the HU number includes a positive excursion from 800 to 180 cal yr BP and a notably depressed HU number at 500 and 300 cal yr BP.

2.6 Discussion

Given the interest in assessing the relationship between hydroclimate variability and documented changes in the Harappa, I focus my efforts on developing a holistic

paleoenvironmental reconstruction spanning the interval captured by DRL-1 (5200 – 3000 cal yr BP).

2.6.1 Elemental and Radiological Proxies Environmental Interpretation

PCA Axis 1 is inferred to primarily reflect variations in detrital influx. The elements most strongly correlated with PCA axis 1 (K, Ti, Fe, Rb, Sr, Zr, and Th) have been identified as common constituents of detrital-sourced sediment (see Olsen et al., 2010; Wünnemann et al., 2010; Cuven et al., 2011; Haenssler et al., 2013; Heymann et al., 2013; Olsen et al., 2013; Cherkashina et al., 2014; Hahn et al., 2014; Nakamura et al., 2016; Chassiot et al., 2018; Peng et al., 2019; Schmidt et al., 2019). Furthermore, the grouping of Th with PCA Axis 1 and the strong Spearman's correlation coefficients (Figure 2.13) between Th and Rb ($\rho 2 = 0.92$), Sr ($\rho 2 = 0.89$), and Zr ($\rho 2 = 0.90$), suggests that the concentration of Th is also related to detrital input from the catchment. PCA Axis 2 is inferred to reflect variations in hypolimnetic oxygen conditions. The element most strongly correlated with PCA axis 2 (Mn) is strongly influenced by redox conditions (Haenssler et al., 2013; Heymann et al., 2013). Here, the Fe/Mn ratio is utilized as a proxy for hypolimnetic oxygen conditions and redox conditions (Heymann et al., 2013). However, it is important to note that redox potential in freshwater, reflected by variation in Mn, is controlled by a suite of variables (e.g., dissolved oxygen, pH, temperature, organic matter, and nutrient availability), all of which can be influenced by changing limnological conditions including variations in lake level, thermal stratification and lake productivity.

The PCA identified that Si, Ca, and the Zr/Rb ratio did not account for a statistically significant amount of variance in the elemental data, however, this is likely due to the influence of differing sourcing processes. Calcium, which is associated with calcium carbonate ($CaCO_3$), can be sourced either through detrital transport or through in-lake precipitation processes

including chemical saturation and biogenic production (Haenssler et al., 2013; Heymann et al., 2013). The Spearman's Correlation between Ca and Sr ($\rho = 0.76$); Ca and Si ($\rho = 0.67$); and Sr and Si ($\rho = 0.47$) suggest that both detrital influx and in-lake precipitation of $CaCO_3$ processes are reflected in the sediment geochemistry. Environmentally, conditions for $CaCO_3$ precipitation include highly bioactive lakes and high concentrations of dissolved $CaCO_3$, such as with reduced lake volume (Haenssler et al., 2013; Heymann et al., 2013). Treatment of sediment samples with HCl indicates the presence of $CaCO_3$ throughout the core. Similarly, the positive Spearman's Correlations between Si with Ca ($\rho = 0.67$) and the positive Spearman's Correlations between Si with K ($\rho = 0.67$), Ti ($\rho = 0.59$), Mn ($\rho = 0.60$), Fe ($\rho = 0.57$), Rb ($\rho = 0.46$), Sr ($\rho = 0.47$), and Zr ($\rho = 0.46$), suggest that the Si present in this zone was potentially derived from both biogenic sources and detrital influx (Olsen et al., 2010; Heymann et al., 2013; Hahn et al., 2014).

The Zr/Rb ratio, although used elsewhere as a proxy for grain size, is not utilized in this study due to suspected skewing by K feldspars (Heymann et al., 2013). Evidence to support the assertion that use of the Zr/Rb ratio as a proxy for grain size may be confounded by the presence of K-feldspars at this site is based on the co-occurrence of a low Zr/Rb ratio, reflecting fine-grained sediment, and radiograph-based evidence of the presence of coarse-grained sediment at 3100 cal yr BP. Therefore, the Zr/Rb ratio is not included as a proxy for grain size in the interpretation of environmental conditions.

Sediment stratigraphy is used as additional evidence supporting the paleoenvironmental inferences. The presence of gravel or coarse-grained sediment, evidenced in the radiographs, are used to support the inference of elevated transport energy in the catchment (Fritz et al., 2018). High HU numbers, which corresponds to lighter colors in the grey-scale tomograms similar to the white/light grey values in the X-radiographs, are also used to support the inferences based on

the radiographs. *Trapa* seed cases, which were located by both the X-Ray radiographs and the CT scans, provide evidence of the existence of relatively shallow water conditions, as *Trapa* is typically found in water between 0.3 and 3.6 m with optimal habitat located at approximately 2 m (Hummel and Kivat, 2004).

2.6.2 Paleohydrological and Paleoenvironmental Interpretation

The pXRF-derived elemental counts, the PCA, and radiology results identify prominent fluctuations in hydroclimate conditions between 5000 and 4700; 4350 and 4050; 3600 and 3400; and 3200 and 3000 cal yr BP. The paleoenvironmental interpretation will be organized around these four events.

The event between 5000 and 4700 cal yr BP is initially characterized by elevated elemental counts for PCA axis 1; elevated HU number; and the presence of gravel and coarse-grained sediment between 5000 and 4850 cal yr BP. Taken together, the increase in allogenic detrital influx and the higher transport energy, captured by the elemental counts and sediment stratigraphy, respectively, suggest the occurrence of an episode of elevated precipitation beginning at 5000 cal yr BP. The low PCA axis 2 scores are inferred to reflect decreasing hypolimnetic oxygen availability due to an increase in lake volume (Figure 2.16). A reduction of lake level and lake volume, beginning at 4850 cal yr BP and ending at 4650 cal yr BP, is supported by evidence of lower transport energy (lower PCA Axis 1 scores) and increased oxygenation of the water column (increasing Fe/Mn) (Figure 2.17).

The event between 4350 and 4000 cal yr BP is initially characterized by elevated precipitation and a positive hydroclimate anomaly. This event is larger in magnitude than the event centered at 4850 cal yr BP. This inference is supported by the elevated Fe/Mn ratio driven largely by an increase in Fe, which suggests the occurrence of anoxic conditions in the bottom

water during this interval. The existence of anoxia in the deep water is likely a response to a deepening of the lake and strengthened thermal stratification, both of which would reduce water column mixing and thereby reduce oxygenation of the bottom water. The increase in allogenic detrital input, inferred from the elevated counts for PCA Axis 1 and the elevated HU number provide further support for this inference. Typically, in subtropical environments, increased precipitation would increase erosion in the catchment and the transport of detrital material to the lake (Figure 2.16). At 4200 cal yr BP the parameters outlined above shift in an opposing direction suggesting a lowering of lake levels and the onset of drier conditions and a negative lake mass balance (Figure 2.17).

Hydroclimate variability between 3600 and 3400 cal yr BP is characterized by a relatively small event, which is inferred to reflect the onset of slightly wetter conditions. This inference is supported by the small increase in allogenic detrital input into Deoria Tal, evident in the elevated counts for PCA Axis 1 scores, the corresponding elemental components, and the slightly higher HU number (Figure 2.16). The presence of seed cases belonging to *Trapa*, which requires shallow waters to grow, suggests that the latter half of this event was characterized by a decrease in effective moisture and a lowering of lake levels between 3500 and 3400 cal yr BP. The inference that this event was characterized by a negative hydroclimate anomaly is also supported by the Fe/Mn values. The elevated Fe/Mn values indicate the existence of well-oxygenated bottom waters at 3500 cal yr BP, likely reflecting the increased effectiveness of wind-driven water column mixing in a shallower lake (Figure 2.17).

The event between 3200 and 3000 cal yr BP is inferred to reflect the occurrence of an episode of severe drought. This inference is supported by the existence of an extremely low Fe/Mn ratio, which suggest that the bottom waters were very well oxygenated, likely resulting

from the increased effectiveness of wind-driven water column mixing in a shallow lake. The negative excursion in Ti provides additional support for lake drawdown between 3200 and 3100 cal yr BP, as lower counts of Ti have been associated with drought conditions (Haug et al., 2003). The presence of visibly coarser materials, evident in the radiograph imagery, and the PCA Axis 1 scores and HU number, which abruptly increase at 3100 cal yr BP, suggest that this event resulted in the margin of the lake being drawn closer to the depocenter (Figure 2.16). Taken together these lines of evidence (e.g., low Fe/Mn and Ti values) indicate that this event was characterized by a hydroclimate anomaly that was large enough to significantly lower lake levels (Figure 2.17).

2.6.3 Comparison of Deoria Tal to Regional Paleoclimate Records

Broadly, DRL-1 (5200 – 3000 cal yr BP) is within the middle of a climatic regime characterized by a weakening ISM (Peng et al., 2019). DRL-1, specifically, spans an interval of rapid climatic transition (Menzel 2014). The climatic regime prior to 5200 cal yr BP consisted of gradual climatic "amelioration" characterized by the gradual failure of precipitation due to a weakening of the ISM and IWM (Leipe et al., 2014; Kotlia et al., 2015). However, relative to the modern hydroclimatic regime, precipitation during the interval captured by DRL-1 can be characterized as enhanced (likely driven by the ISM) (Chatterjee and Ray, 2017). The decrease in precipitation was not unidirectional nor gradual through DRL-1. A number of distinctive "centennial-scale" events occurred, characterized by fluctuating hydroclimate, embedded within an overall trend of decreasing effective moisture (Leipe et al., 2014). The four notable events in the Deoria Tal record, at 4850, 4200, 3500, and 3100 cal yr BP, are compared to existing records below.

Contemporaneous records from the region describe an event occurring at either 5000 or 4800 cal yr BP. At 5000 cal yr BP, a wet event is documented in the Greater Himalaya (Kar and Quamar, 2019) with this region further described as warm and humid by Bohra and Kotlia (2015). Other records point to 4800 cal yr BP as the transition point to a climatic regime characterized by decreasing precipitation (Wünnemann et al., 2010) in the Trans Himalaya region (Kar and Quamar, 2019). Additional evidence of decreasing effective moisture at 4850 cal yr BP include the drying up of paleolake Lunkaransar in northwestern India due to the water table dropping (Enzel et al., 1999), contraction of forest groves (Chauhan et al., 2015), and a net decrease in fluvial discharge (Gische et al., 2019).

Though the 4200 cal yr BP event is described as being initiated with cold phase in the northern Atlantic Ocean (Leipe et al., 2014), it is documented to have impacted India (McDonald 2011). Numerous studies identify the occurrence of a notable decrease in the monsoon at 4200 cal yr BP (Tripathi et al., 2017). Most studies suggest that this event was characterized by a weakened ISM (Weiss, 2016, and references within); however, more recent research implicates a weakened IWM as contributing to the regional drought (Gische et al., 2019), which culminated in the largest negative hydroclimate anomaly of the mid- to late Holocene (Wünnemann et al., 2010). Regionally, Kar and Quamar (2019) describe the coastal areas as being “excessively dry” and the Trans Himalaya experiencing a cold and arid climate at 4200 cal yr BP.

Some authors subscribe to an “extension” of the 4200 cal yr BP event in India, with hydroclimate variability between 4500 and 4000 cal yr BP associated with the 4200 cal yr event (Leipe et al., 2014). The global 4200 cal yr BP event occurred in the middle of a “climatic deterioration” in India, with a trend toward a cooler and drier climate (Demske et al., 2016). The

inference that the interval between 4700 and 4000 cal y BP was characterized by decreasing precipitation is corroborated by other regional studies:

- The Asian SW Monsoon was weak between 4600 to 4200 cal yr BP (Gupta et al., 2003).
- Indications of soil disturbances associated to increased fluvial activities at riverside habitats dated to 4500 cal yr BP (Demske et al., 2016).
- A weak monsoon event at 4400 cal yr BP impacted the Arabian Sea winds (Gupta et al., 2006).
- A prominent drought event occurred at 4400 cal yr BP (Leipe et al., 2014).
- The Lesser Himalayas experienced a brief pluvial 4300 to 4000 cal yr BP, but afterwards the sharp decline in trees suggested a shift to a cool and dry climate (Kar and Quamar, 2019).
- A gradual decline in monsoonal wind intensity culminated at 4200 cal yr BP, shifting the regime to a prolonged weak monsoon interval that continued until 3700 cal yr BP (Nakamura et al., 2016).
- A widespread drought in northern India dated to approximately 4200 cal yr BP (McDonald, 2011).
- The ISM weakened abruptly at 4100 cal yr BP, lasting for approximately 200 years (Dixit et al., 2014).
- At approximately 4000 cal yr BP, the Ganga Plain regionally experienced a decrease in the number of trees due to the decline in humidity due to a weakening of the SW monsoon (Kar and Quamar, 2019).

Furthermore, the effects of the 4200 cal yr BP event were not uniformly or evenly distributed in India, with site-specific variations in climate conditions (Chauhan et al., 2015; Kar and Quamar, 2019) vegetation and paleoenvironments (Gupta et al., 2006).

The event at 3500 cal yr BP is proposed to correspond to the record by Sharma and Gupta (1997), in which a "catastrophic decline" of broad leaf and oak vegetation is identified as occurring at 3600 cal yr BP during a cool, humid interval. Similarly, at 3500 cal yr BP there was a decline in mangrove populations although a slight increase in moisture occurred in coastal areas (Kar and Quamar, 2019). There was a notable amount of spatial variation, however the general trend was characterized by increasing precipitation (Kar and Quamar, 2019). It is important to note that regional differences in hydroclimate are evident at approximately 3500 cal yr BP (Menzel, 2014; Kar and Quamar, 2019). This could be due to: (1) poor chronological control as the timing of this event seems to occur between 3600 (Sharma and Gupta, 1997; Gupta et al., 2003; Kothyari et al., 2017) and 3400 cal yr BP (Gupta et al., 2006; Mohan et al., 2017) and; (2) the literature differs as to the sign of the event. Inferred shifts in the climatic regime around 3500 cal yr BP include:

- 3500 cal yr BP being the end of a wet regime that started around 3900 cal yr BP (Menzel, 2018).
- 3500 cal yr BP being the start of a heavy rainfall event that lasts until 3400 cal yr BP (Mohan et al., 2017).
- 3600 cal yr BP being the start of a weak Asian SW monsoon event until 3300 cal yr BP (Gupta et al., 2003).
- At approximately 3650 cal yr BP monsoons weakened due to an increase in the penetration of Arctic air, resulting in a regional cooling (Bryson and Murray, 1977).

- 3400 cal yr BP being a weak monsoon event with Arabian Sea wind impact (Gupta et al., 2006).

Although there are notable variations in inferred regional hydroclimate between 3600 and 3400 cal yr BP it is clear that at approximately 3500 cal yr BP a notable shift in regional hydroclimate did occur.

Existing studies document a decline in monsoon strength (Nakamura et al., 2016), signaling a transition to a climate regime characterized by decreasing precipitation at 3100 cal yr BP. The weakened monsoon was likely a response to decreasing solar insolation (Ankit et al., 2017). This transition is identified as occurring slightly earlier at 3200 cal yr BP (Leipe et al., 2014; Kotlia et al., 2015) with evidence of forest thinning (Sharma et al., 2000) and marked vegetational changes due to fires and human influences exasperating natural factors (Demske et al., 2016). In coastal areas, the negative hydroclimate anomaly at 3200 cal yr BP led to an increase in the abundance of salt tolerant mangroves (Kar and Quamar, 2019). The exact timing of the transition notwithstanding, by approximately 3000 cal yr BP the end of the transitional phase is generally viewed as complete (Sharma et al., 2000; Wright et al., 2008). By 3000 cal yr BP, modern river morphology had developed (Kothyari et al., 2017) and regional differences associated with the new precipitation patterns were manifested as some localities experienced record lake level lows (Prasad et al., 1997) while other areas experienced a surge in precipitation (Wright et al., 2008). The large spatial extent and the existence of notable environmental heterogeneity within this region would make it unlikely that climatic expressions of hydroclimate variability would manifest uniformly (Petrie et al., 2017).

2.6.4 Hydroclimate Variability, the Harappa, and the 4200 cal yr BP Event

The 4200 cal yr BP event occurs at the same point in time as the beginning of the Harappan "collapse", which was prolongated enough that it has been further described as "deterioration", "deorganization", "cultural transition", "protracted collapse", or "metamorphosis" (Staubwasser et al., 2003; Madella and Fuller, 2006; Wünnemann et al., 2010; McDonald, 2011; Giosan et al., 2012; Ponton et al., 2012; Kotlia et al., 2015; Sarkar et al., 2016; Giosan et al., 2018). Currently, there is no consensus as to whether human or environmental factors are considered to be more influential on the Harappan transformation (Petrie et al., 2017). Instead of a direct causal relationship, the opinion of this writing is that the 4200 cal yr BP event has more of a "casual" relationship with the decline of the Harappa (Staubwasser et al., 2003). As Staubwasser et al. (2003) explained, from a climatic standpoint, the 4200 cal yr BP event would have impacted the agricultural base of the agrarian society and therefore the complexity of a combined environmental and human influence, which possibly in small part, contributed to the eventual demise of the civilization.

The Harappan agriculture system was dependent on flooding rather than precipitation directly (Giosan et al., 2012). The rise of the Harappa cultural complexity, between approximately 5000 and 4200 cal yr BP, coincided with an interval characterized by a trend of decreasing ISM and IWM. This allowed for crops to be planted in what previously were flood-prone areas without the crops being washed away (Giosan et al., 2012). With the increase of agricultural product and success, flourishing urban areas were common by 4200 cal yr BP during the Mature Harappan phase (Madella and Fuller, 2006). However, weakening of the ISM and IWM continued to the point where the agricultural grounds were no longer being sufficiently inundated by flood waters. Whether it was in response to the 4200 cal yr BP event (Giosan et al.,

2012), at approximately 4000 cal yr BP (Farooqui et al., 2013; Leipe et al., 2014), or before 4600 cal yr BP (Sarkar et al., 2016), the Harappa switched their primary agricultural base from winter crops of wheat and barley to summer crops of rice and millet. Sarkar et al. (2016) referenced the winter to summer crop change, which is coincident with interval captured by DRL-1, as the first step of the Harappan "de-organization".

After 4200 cal yr BP, the Harappa responded to the deteriorating climatological conditions by migrating upvalley into the periphery and away from urban centers, following the receding optimal flooding regime for agriculture (Rajani and Rajawat, 2011; Giosan et al., 2012; Giosan et al., 2018). Schug et al. (2013) proposed that the Harappa urban centers were able to handle the centuries of ecological climatic stress, including the 4200 cal yr BP event, until approximately 4000 cal yr BP where the stress on the agricultural base led to gradual depopulation. Furthermore, significant anthropogenic influences on the landscape are evidenced in the paleo- records between 4500 and 4000 cal yr BP (Leipe et al., 2014; Demske et al., 2016; Enzel et al., 1999), with negative hydroclimate anomalies compounded in some areas by the crop cultivation itself (Tripathi et al., 2017) and farming areas experiencing soil erosion (Madella and Fuller, 2006). Bryson and Murray (1977) summarized the tenuous situation: the population base grew, agricultural practices intensified, drier years came, the grass cover weakened, a dust bowl grew, and the Harappa increased agricultural activity and moved to other areas to maintain the production—eventually abandoning many of the cities adjacent to the former farmlands that then were buried by sand. The drought at 4200 cal yr BP, associated with a weakened ISM and IWM, ceased at 3900 cal yr BP (Gische et al., 2019). Coinciding with elevated precipitation at 3900 cal yr BP, the leading cause of death amongst the Harappa was no longer associated with ecologically driven food stress, but rather violence and infection (Schug et al., 2013). The

"dispersal" of the Harappan peoples continued during this time (Leipe et al., 2014). Bryson and Murray (1977) mark approximately 3650 cal yr BP as the beginning of the interval of "rapid" decline. The "collapse" of the Harappa civilization was completed between 3500 to 3000 cal yr BP (Kotlia et al., 2015). By approximately 3000 cal yr BP written material and artifacts of the Harappa civilization were no longer evident in the archaeological record (Leipe et al., 2014).

Though climatically the monsoon precipitation was decreasing during DRL-1, it is important to note that the interval captured by DRL-1 is marked by being very fluvially active (Demske et al., 2016; Sarkar et al., 2016) with enhanced surface water runoff (Ankit et al., 2017). The fluvial activity continued to decline tracking precipitation until it decreased enough to reach the modern fluvial regime at approximately 3000 cal yr BP (Kothyari et al., 2017). However, as Chatterjee and Ray (2017) clearly noted, the rivers were still flowing during the Harappan period, so the hypothesis that the Indus River (and others) dried up could not be the sole cause of the Harappan "decline."

Unlike the contemporaneous civilizations, the Harappa did not develop canal or irrigation technology to compensate for the lack of reliable flooding by harnessing the snow-fed systems of the local hydrology (Giosan et al., 2012; Giosan et al., 2018). If the Harappa had been able to do so, then additional land could have been made available for farming. Unfortunately, the Harappa were caught chasing the receding optimum flood regime dependent farm land. It is likely that the Harappa ran out of suitable farming lands and/or they overextended beyond their resource capacity. Ultimately, the shifts in hydroclimate that characterized the late Mature Phase were not favorable for the Harappa to prevent the "protracted collapse" (Ponton et al., 2012).

2.7 Conclusion

The analysis of Deoria Tal's lacustrine sediment core highlighted anomalous hydroclimate events occurred centered at 4850, 4200, 3500 and 3100 cal yr BP. Utilization of non-destructive radiological imaging facilitated the development of a highly resolved (sub-annual scale) paleoenvironmental record that enabled the identification of these anomalous hydroclimate events. The first three events (4850, 4200, and 3500 cal yr BP) are inferred to reflect initially positive hydroclimate anomalies and higher lake levels, as evidenced by elevated detrital flux (PCA Axis 1) and decreased bottom water ventilation (Fe/Mn). The 3100 cal yr BP event is inferred to reflect negative hydroclimate anomalies and notable lake drawdown initially, as evidenced by decreasing detrital flux, extremely low Fe/Mn and the presence of *Trapa* seed cases. Importantly, the Deoria Tal record captures the complexity of hydroclimate response during the 4200 cal yr BP event. The interval between 4350 and 4200 cal yr BP was characterized by positive hydroclimate anomalies and elevated lake levels; between 4200 and 4050 cal yr BP this region was characterized by a centennial-scale drought event. The fluctuating hydroclimate evident during the 4200 cal yr BP event can be explained by changes in the relative strength of the IWM or Westerly Disturbances between 4300 and 4100 cal yr BP. Ongoing research including biological proxies, mainly chironomids and pollen, and stable oxygen isotopes are anticipated to help further refine the inferences of lake level variations between 5200 and 3000 cal yr BP.

2.8 Tables

Table 2.1. Radiocarbon samples from Deoria Tal's core. All samples were calibrated using OxCal 4.3 (Bronk Ramsey 2017) with the ages reported using the 2σ range derived from Reimer et al. (2013).

Sample Location	**Depth (cm)**	**Sample Material**	**CAIS ID#**	**pMC**	**$\delta^{13}C$**	**^{14}C yr. BP**	**Cal yr. AD/BC (2σ)**	**Curve**
Modern	0	Seed Case	36821	101.99 ± 0.25	-26.81	modern	1955.48 - 1957.44 AD	Bomb13 NH3
PT	61	Seed Case	37904	98.26 ± 0.23	-25.41	140 ± 20	1670.94 - 1707.92 AD 1719.06 - 1779.30 AD 1799.3 - 1826.72 AD 1832.54 - 1888.08 AD 1913.80 - 1942.90 AD 1952.56 - 1953.86 AD	Bomb13 NH3
PT	89.67	Seed Case	37905	95.76 ± 0.23	-23.24	350 ± 20	1462 - 1529 AD 1545 - 1635 AD	IntCal13
LC1A	117.5	Seed Case	37906	92.58 ± 0.23	-25.11	620 ± 20	1294 - 1330 AD 1339 - 1397 AD	IntCal13
LC1A	163	Seed Case	37907	89.6 ± 0.22	-26.57	880 ± 20	1049 - 1084 AD 1124 - 1137 AD 1150 - 1218 AD	IntCal13
LC1B	189	Seed Case	37908	89.79 ± 0.22	-24.85	870 ± 20	1052 - 1080 AD 1151 - 1220 AD	IntCal13
LC1B	252	Seed Case	37909	82.66 ± 0.20	-24.24	1530 ± 20	429 - 494 AD 511 - 517 AD 529 - 595 AD	IntCal13
LC1C	290	Seed Case	37910	77.31 ± 0.19	-26.03	2070 ± 20	166 - 41 BC	IntCal13
LC1C	304	Seed Case	40239	73.53 ± 0.19	-26.22	2470 ± 20	764 - 508 BC 500 - 491 BC	IntCal13
LC1C	329	Seed Case	40238	66.1 ± 0.18	-26.55	3330 ± 20	1683 - 1672 BC 1666 - 1597 BC 1588 - 1532 BC	IntCal13
LC1D	372	Seed Case	37104	56.8 ± 0.16	-24.99	4540 ± 25	3365 - 3311 BC 3295 - 3287 BC 3275 - 3265 BC 3239 - 3105 BC	IntCal13

Table 2.2. Stratigraphical description of Plastic Tube (PT) sediment. Stratigraphical description of sediment recovered with a plastic tube and location of *Trapa* seed cases.

Depth (cm)	**Stratigraphical Description**	***Trapa* Seed Case Depth Locations (cm)**
50 - 81.67	Moderately brown, moderately organic, lake mud	61, 69
81.67 - 95	Dark brown, organic, gyttja	89.67

2.9 Figures

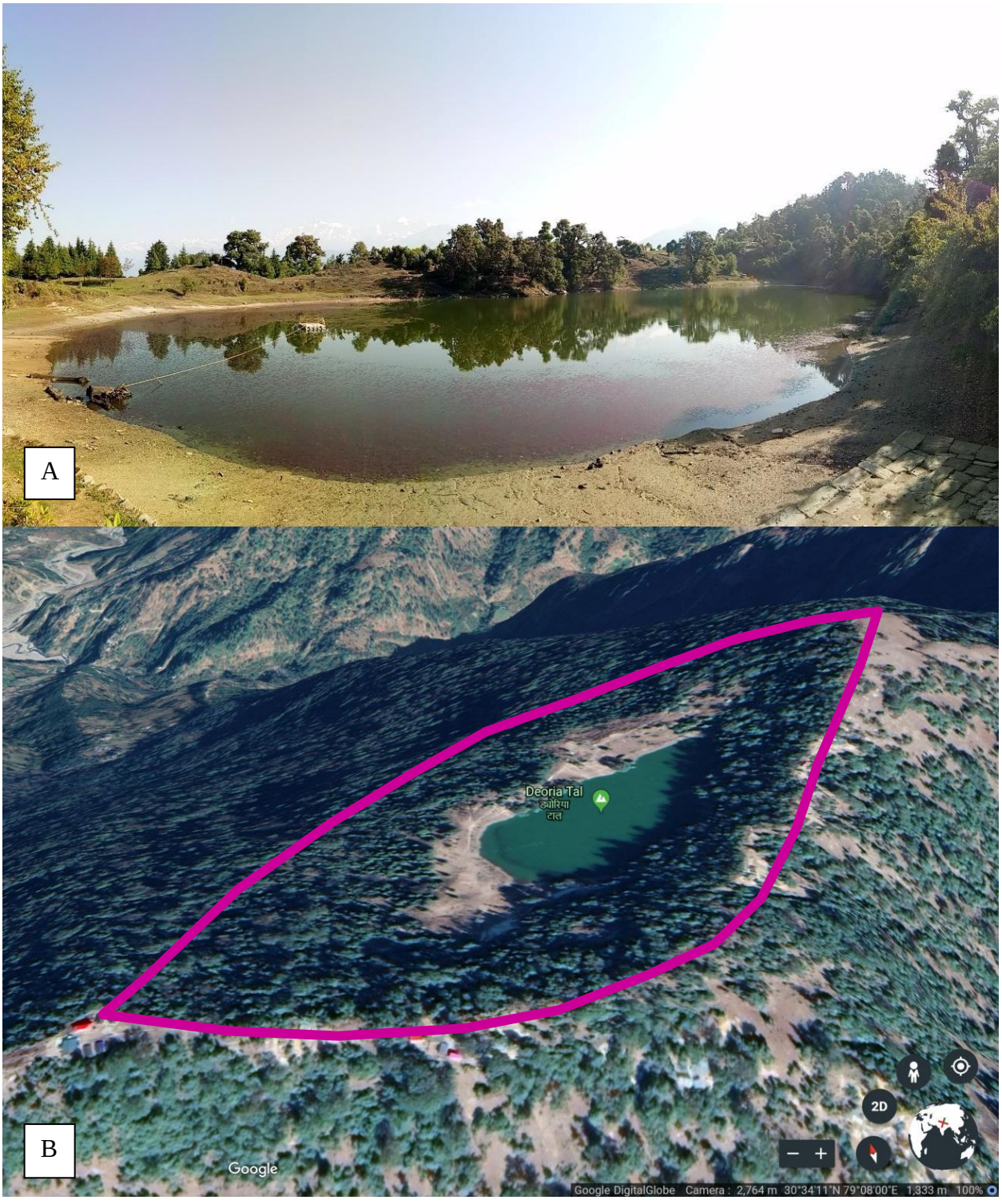
A
B
Deoria Tal
ड्योरिया
ताल
2D
Google
Google DigitalGlobe Camera : 2,764 m 30°34'11"N 79°08'00"E 1,333 m 100%

Figure 2.1. Study area. (a) Photo of Deoria Tal illustrating the location of *Trapa* in the littoral of the lake, the coring platform, and the snow-covered peaks of the Himalaya in the background (Porinchu 2018, image). (b) Google Earth image (n.d.) of Deoria Tal with the closed basin catchment (11 ha) outlined in pink.

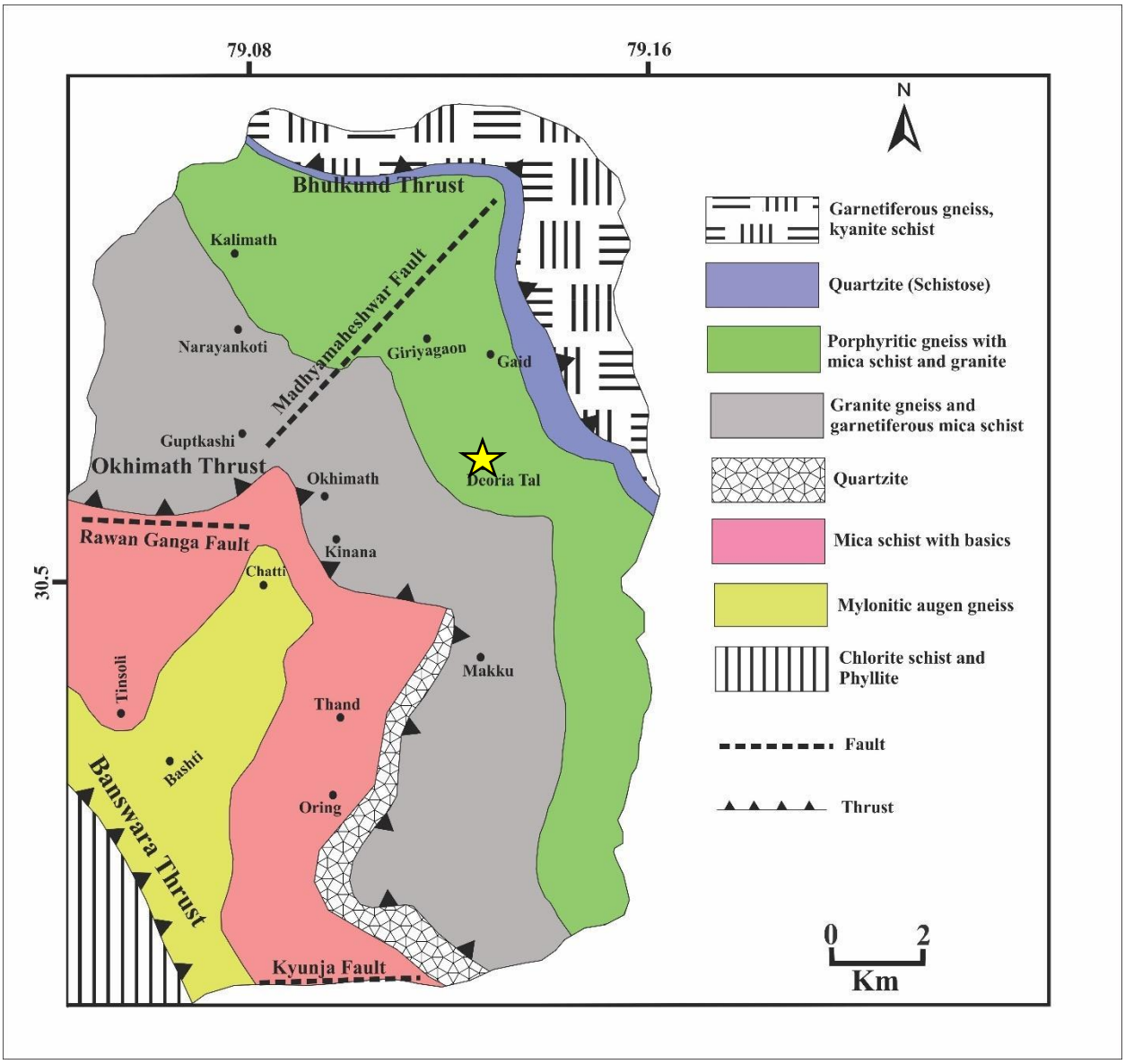

Figure 2.2. Map of the geological context for Deoria Tal. Geologic context for Deoria Tal (indicated with a yellow star) showing the high-grade metamorphic terrain (Chaudhary et al., 2010; Kotlia, 2019, personal communication). The lithotectonic groups present in the area are delineated by three thrusts. The first lithotectonic group is located adjacent to the Bhulkhund Thrust, the second is between the Bhulkhund Thrust and the Okimath Thrust, and the third is between the Okimath Thrust and the Banswara Thrust.

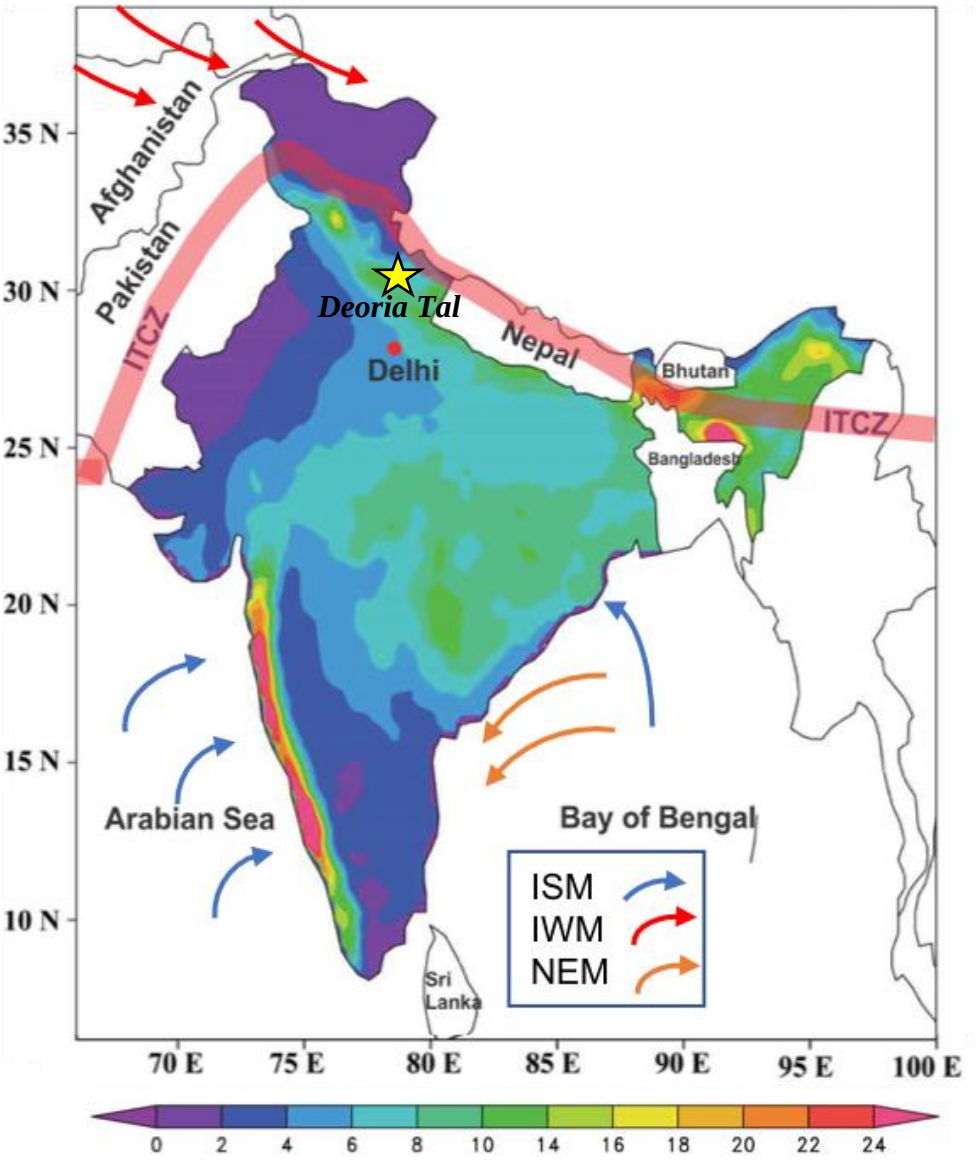

Figure 2.3. Climatological map of India. Modified after Patwardhan et al. (2016) with the choropleth designating the mean Indian Summer Monsoon (ISM) for summer precipitation (JJAS) based on 1951-2000 instrumental data in mm/day and the study location of Deoria Tal designated with a yellow star (base map provided by Dr. Anoop Singh). Arrows show the prevailing direction of the seasonal winds and associated precipitation, including ISM for Indian Summer Monsoon, IWM for Indian Winter Monsoon (Western Disturbances), and NEM for

Northeast Monsoon. The mean northern-most position of the Intertropical Convergence Zone (ITCZ) is highlighted in red.

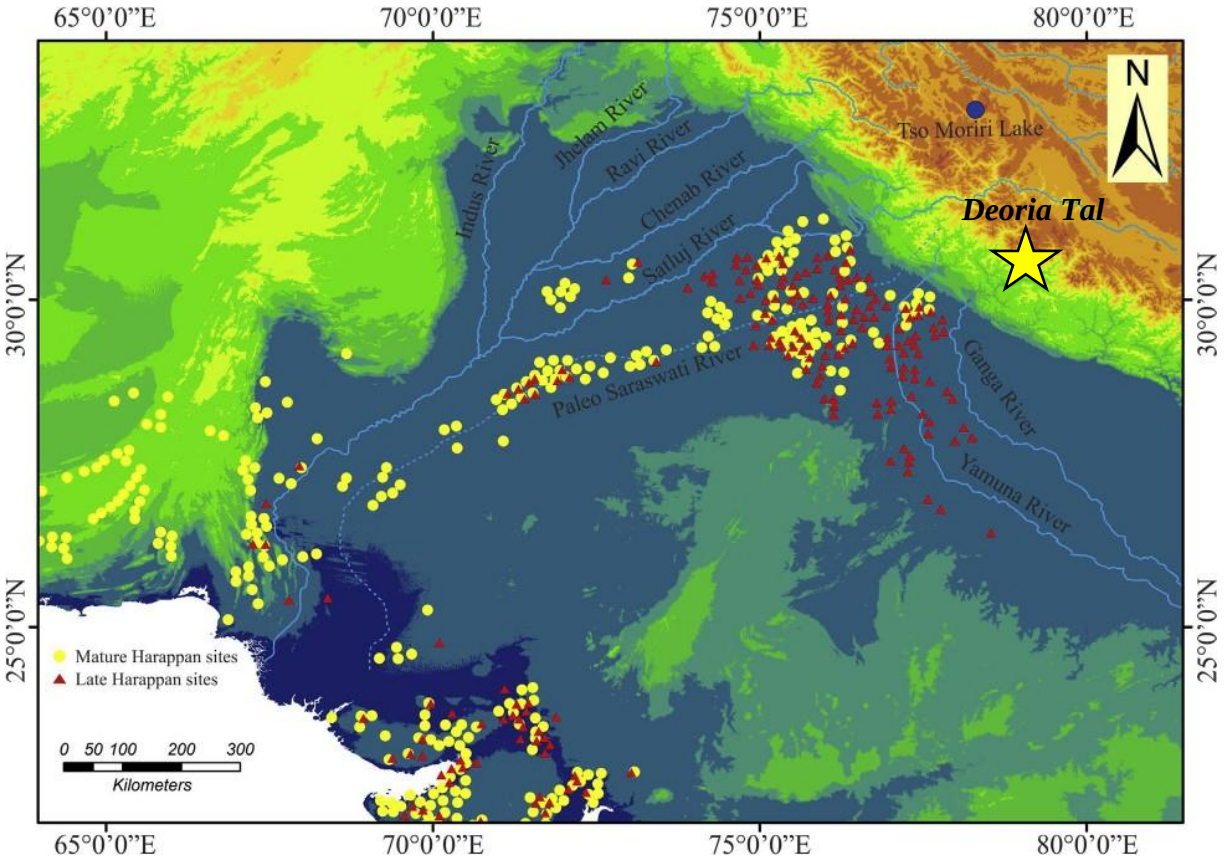

Figure 2.4. Harappan Civilization and Deoria Tal. Modified after Dutt et al. (2018), Deoria Tal is denoted with a yellow star. Yellow circles denote Mature Harappan sites and red triangles denote Late Harappan sites.

Figure 2.5. *Trapa* seed case. The *Trapa* seed case specimen is pictured with a US quarter for scale (Niederman 2019, image).

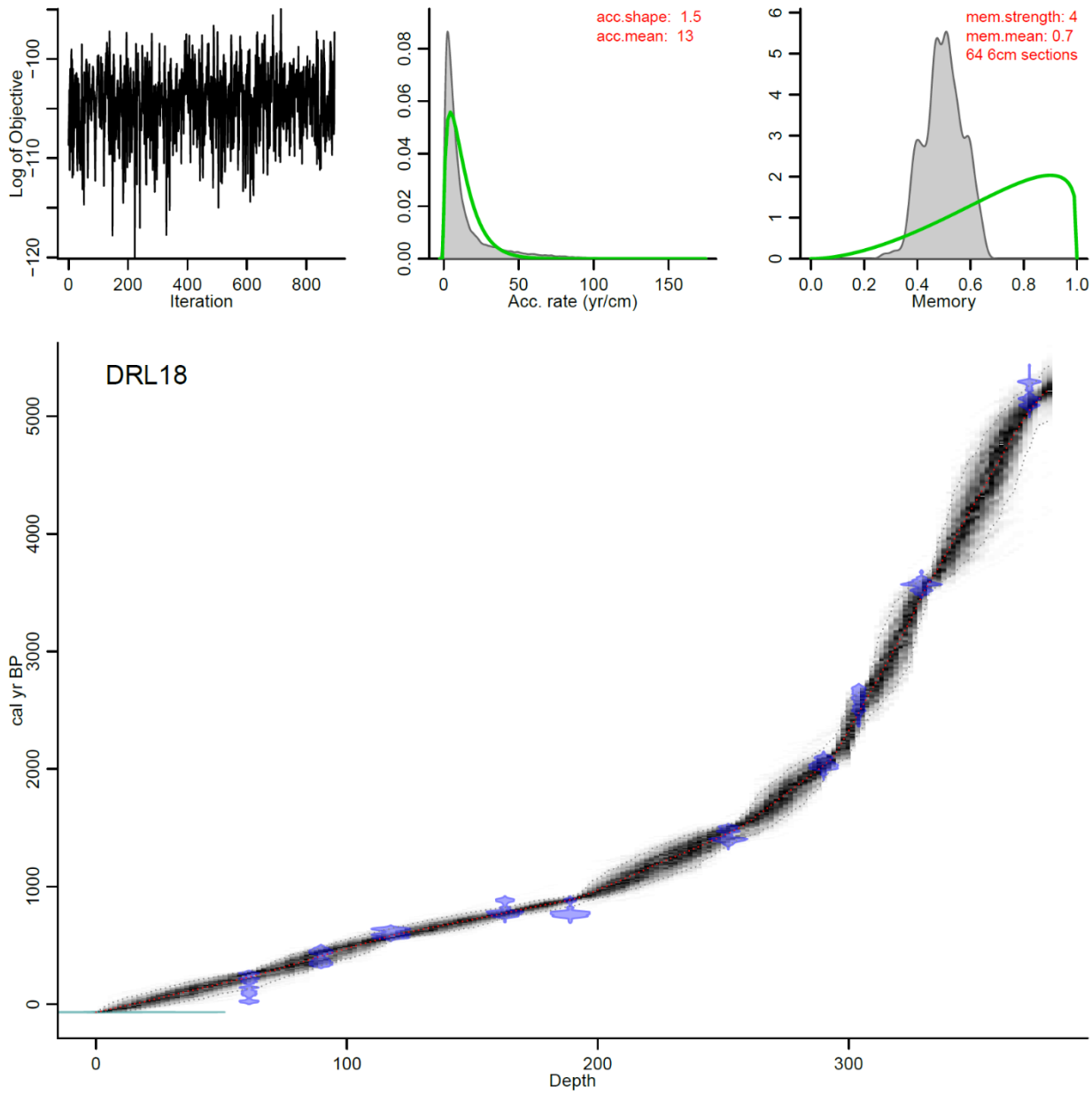

Figure 2.6. Age depth model for the Deoria Tal core. Age-depth model output from BACON (Blaauw and Christen 2011). The depth of the lake sediment core (x-axis) is plotted from 0 cm (top) to 380 cm (bottom) and the age calibration (y-axis) is plotted in cal yr BP. Each of the water chestnut seed cases (blue) are plotted against the age-depth curve (black) with the dotted lines marking the 2σ range of certainty.

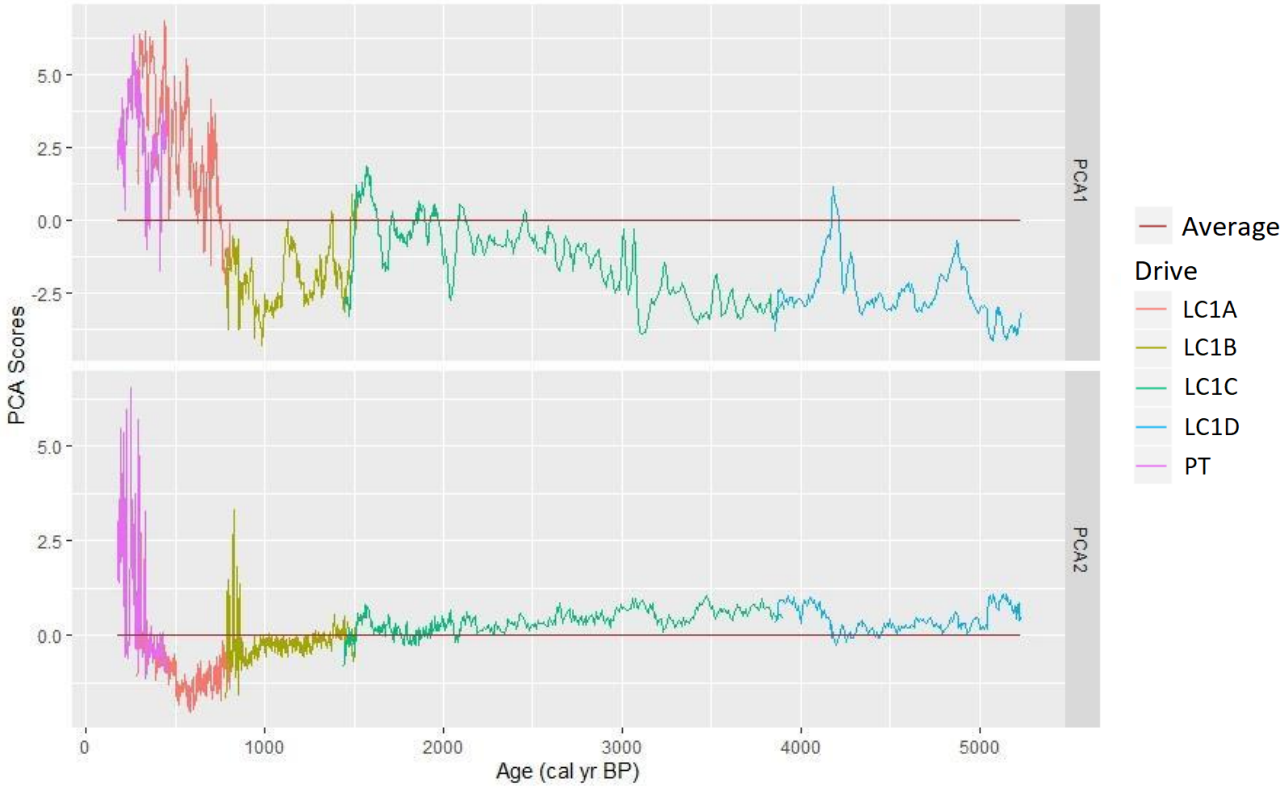

Figure 2.7. Principal Component Analysis (PCA) of the elemental data. Stacked graph depicting principal component analysis (PCA) axes 1 and 2. Individual core drives are uniquely identified via color.

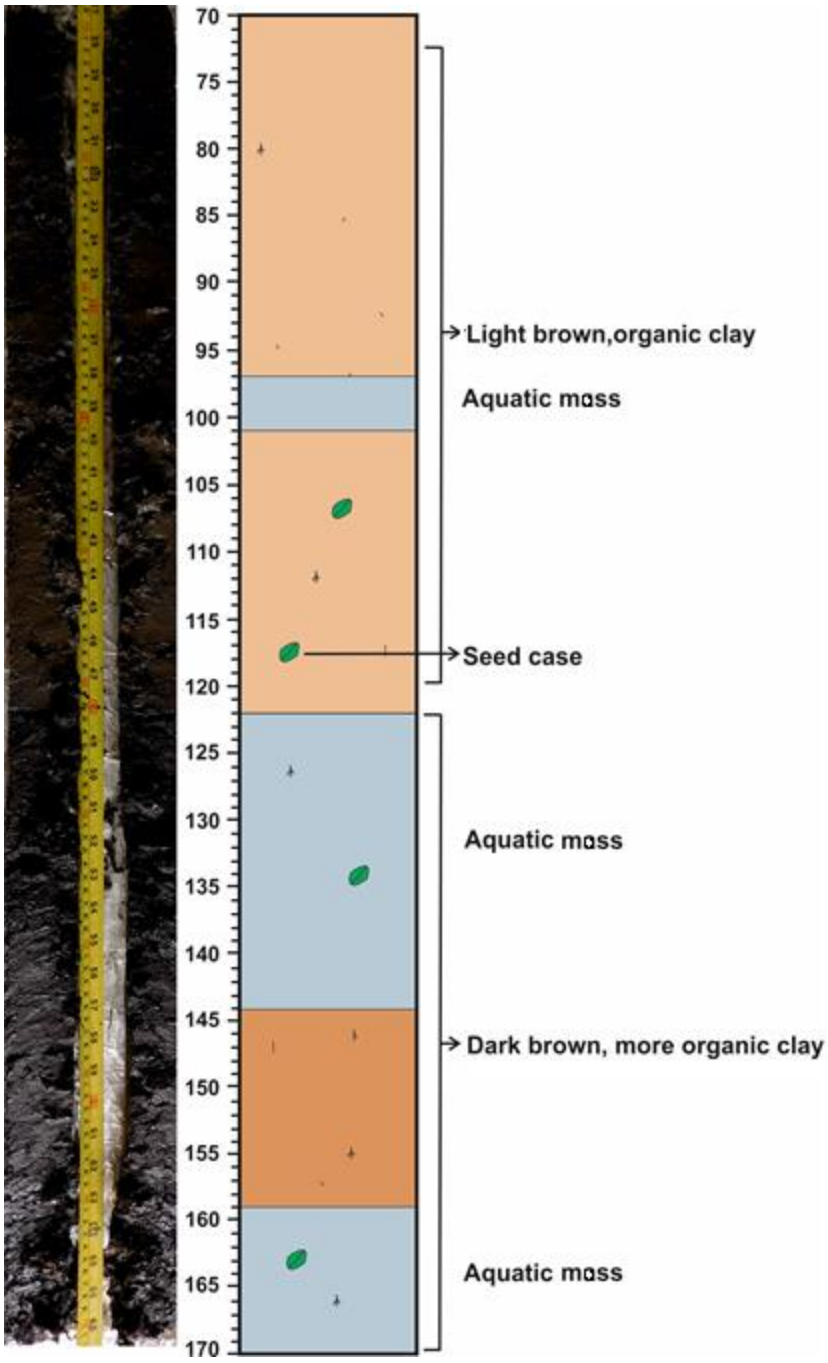

Figure 2.8. Long Core (LC) stratigraphical depiction. A) Depiction of the cross-section LC1A with a ruler in cm, an image of the core segment, and core stratigraphy (Kholia and Kotlia, 2018, personal communication). Seed cases with potential for radiocarbon dating are represented by the green ovals. The location of abundant aquatic moss is depicted in blue.

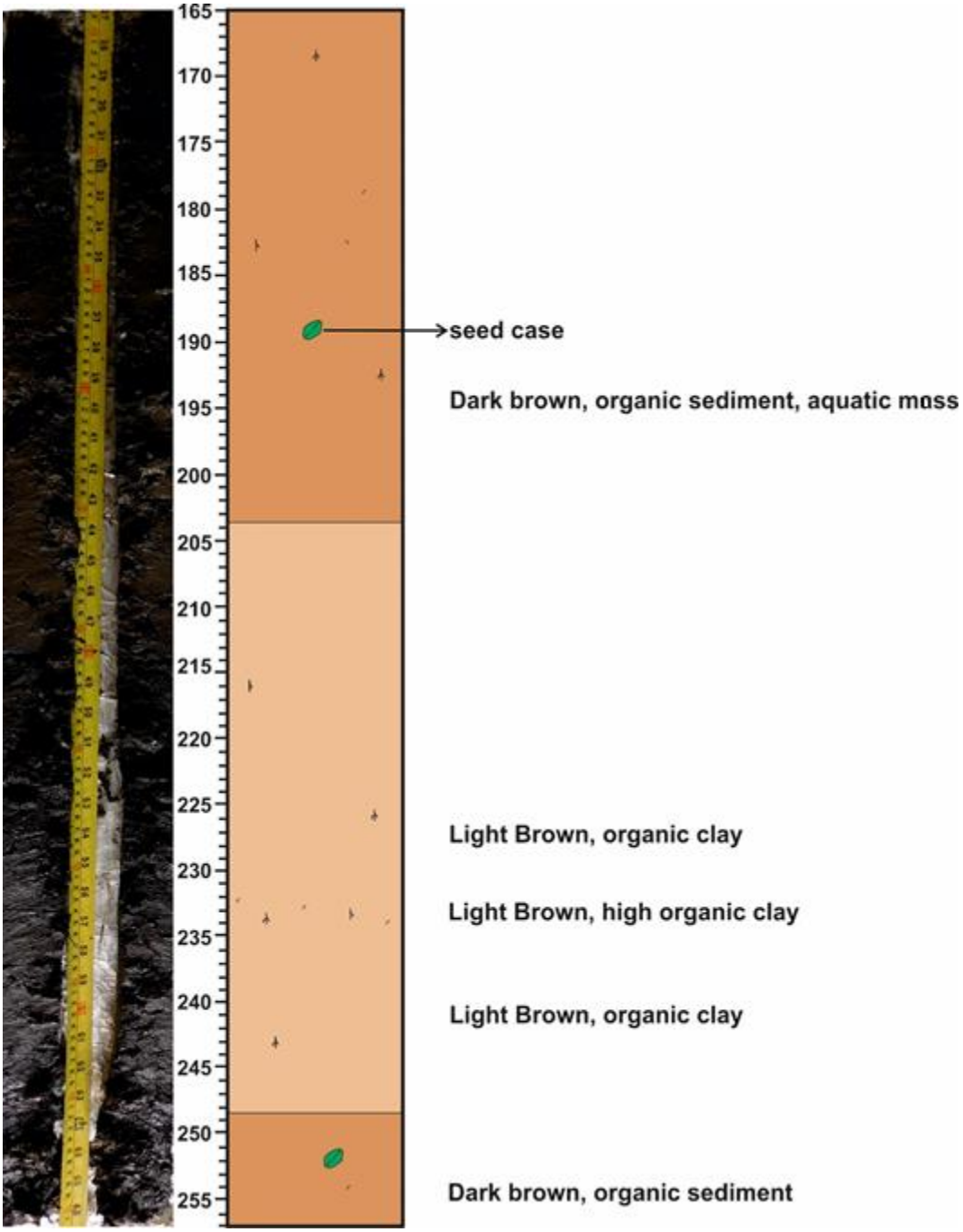

Figure 2.8. Long Core (LC) stratigraphical depiction. B) Depiction of the cross-section LC1B with a ruler in cm, an image of the core segment, and core stratigraphy (Kholia and Kotlia, 2018, personal communication). Seed cases with potential for radiocarbon dating are represented by the green ovals.

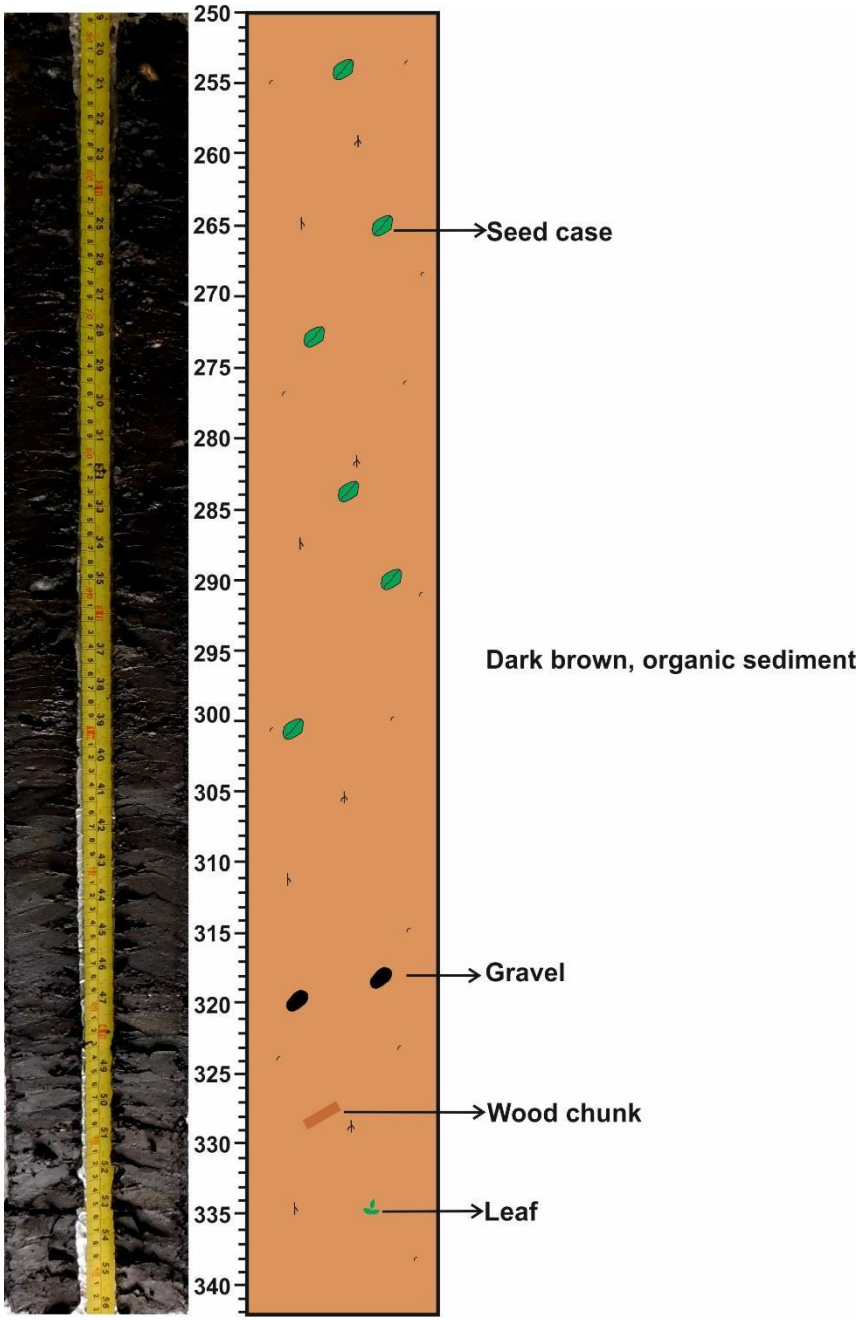

Figure 2.8. Long Core (LC) stratigraphical depiction. C) Depiction of the cross-section LC1C with a ruler in cm, an image of the core segment, and core stratigraphy (Kholia and Kotlia, 2018, personal communication). Seed cases with potential for radiocarbon dating are represented by the green ovals. The location of gravel, a piece of wood, and a leaf are also depicted and labeled.

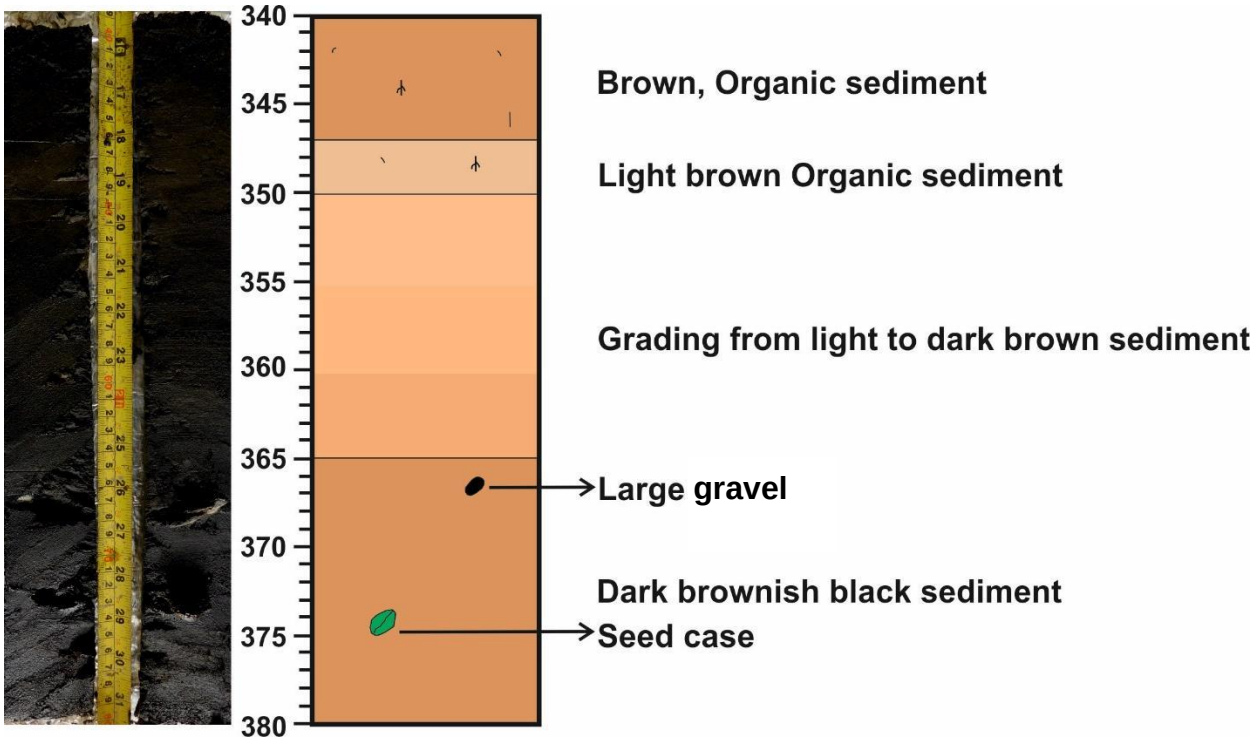

Figure 2.8. Long Core (LC) stratigraphical depiction. D) Depiction of the cross-section LC1D with a ruler in cm, an image of the core segment, and core stratigraphy (Kholia and Kotlia, 2018, personal communication). Seed cases with potential for radiocarbon dating are represented by the green ovals. The location of a large gravel is also depicted.

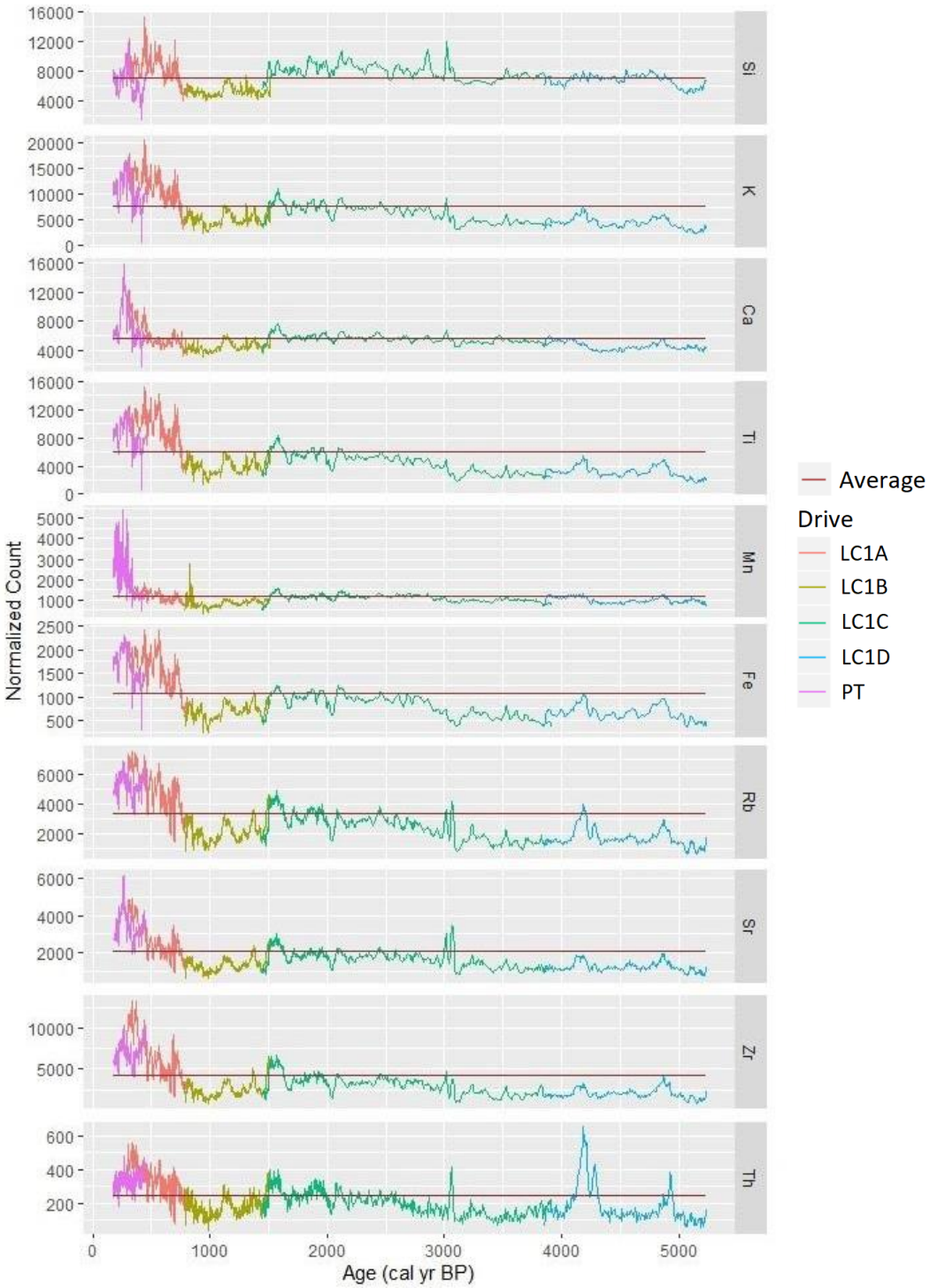

Figure 2.9. X-ray Fluorescence (XRF) elemental emission spectra. Stacked graph depicting the normalized counts of the x-ray emission spectra for all the elements measured by the pXRF scanner. Individual core drives are uniquely identified via color. The red line represents the mean value for each ratio.

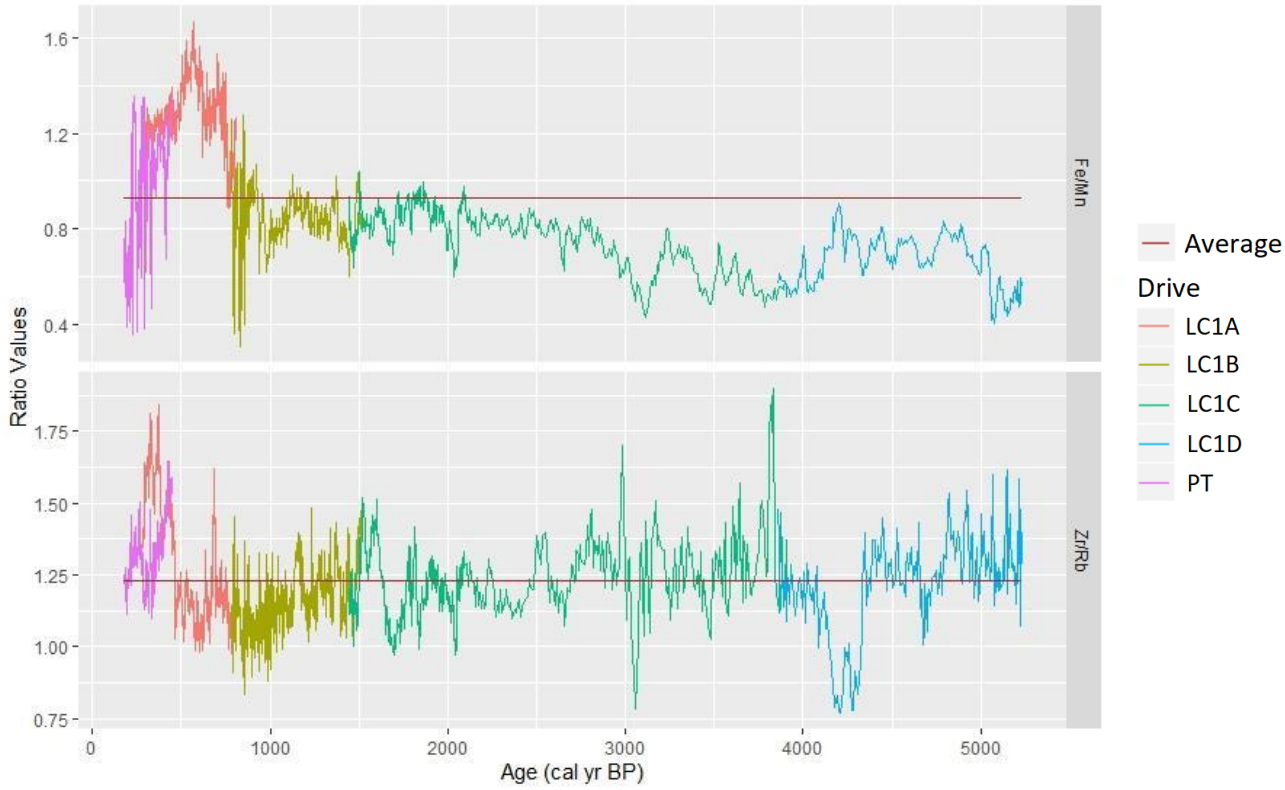

Figure 2.10. X-ray Fluorescence (XRF) elemental ratios emission spectra. Stacked graph depicting the ratio values of the x-ray emission spectra for Fe/Mn and Zr/Rb. Individual core drives are uniquely identified via color. The red line represents the mean value for each ratio.

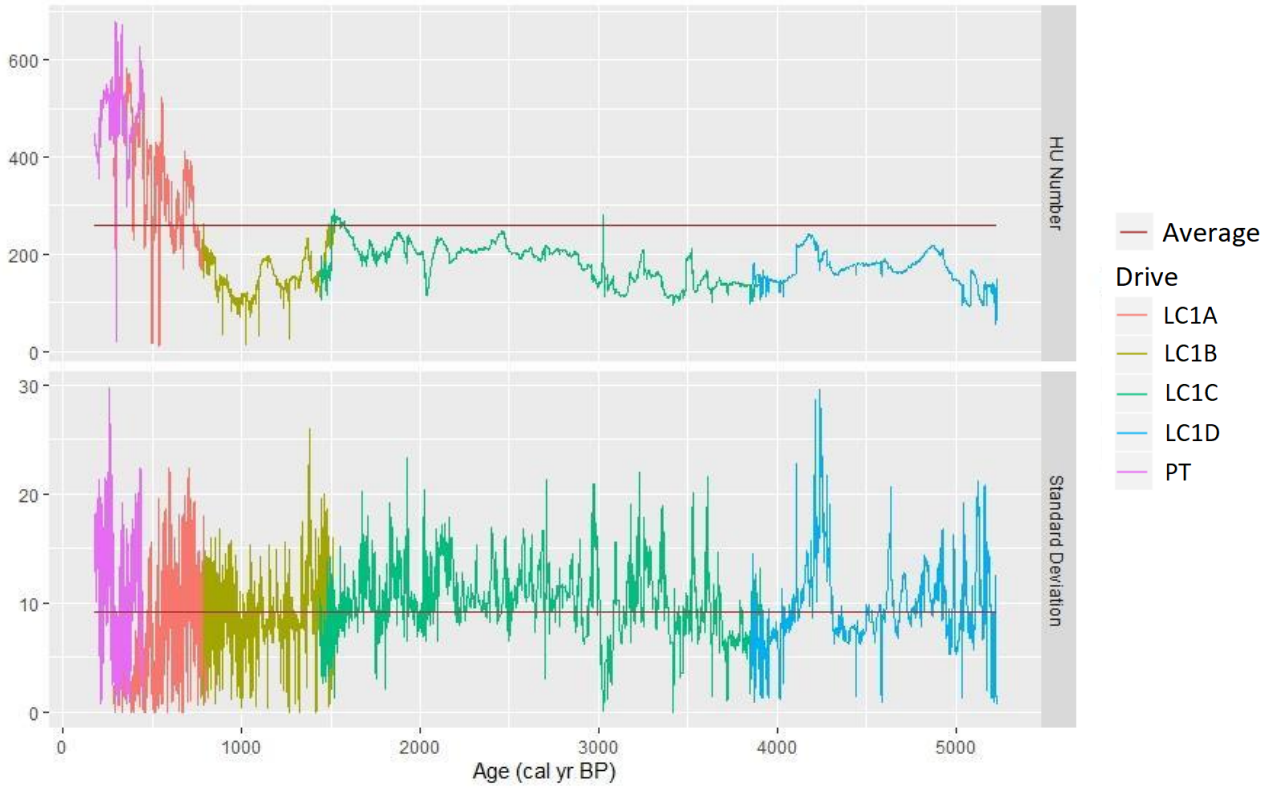

Figure 2.11. HU number and standard deviation from Computerized Tomography (CT). Stacked graph depicting the HU number and standard deviation for the Soft CT frequency. Individual core drives are uniquely identified via color. The red line represents the mean value for the HU number and standard deviation.

PT (50-75 cm)

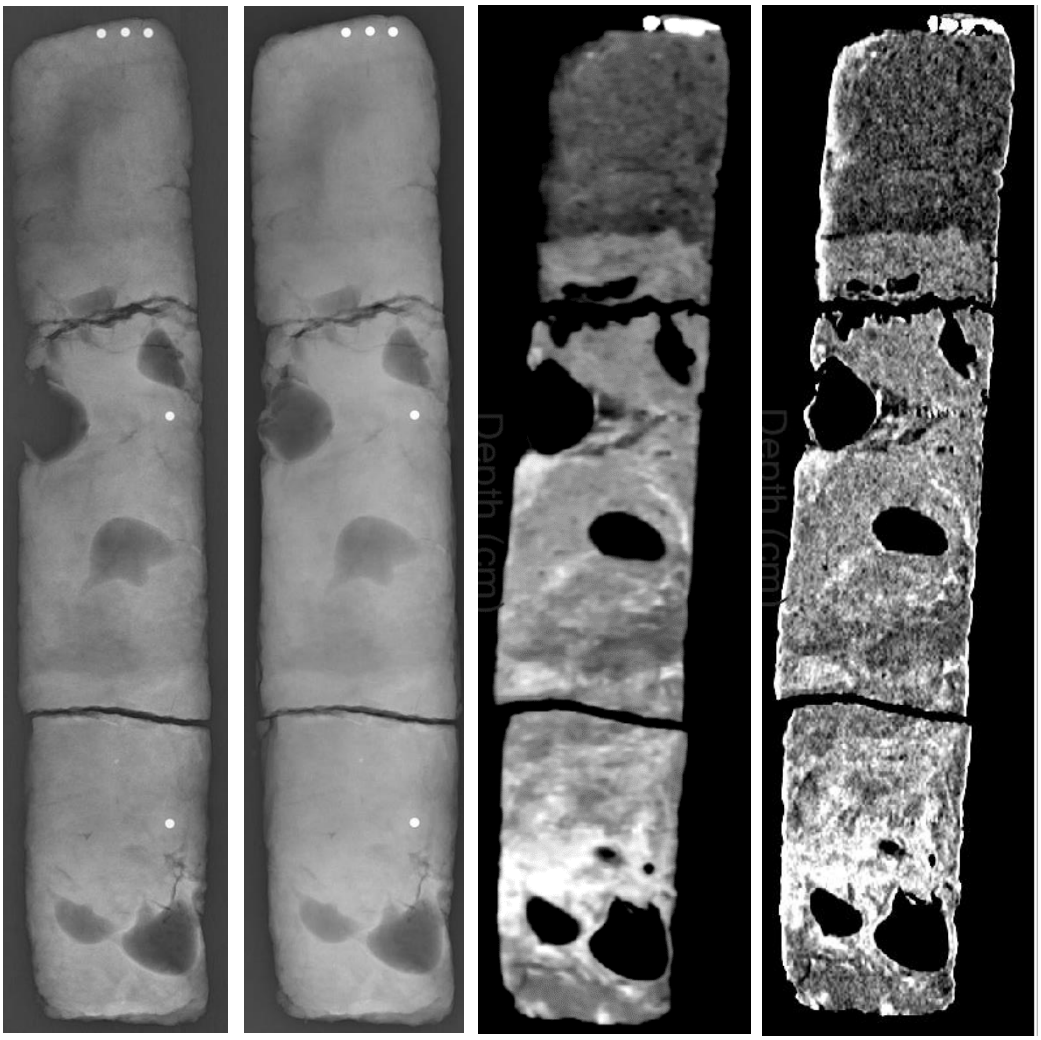

Figure 2.12. Radiographs and compiled tomograms for Plastic Tube (PT) core. A) Four images of PT drive (50 — 75 cm) as captured using the abdomen and right extremity x-ray settings along with the stacked CT model produced by SedCT for both soft tissue and bone settings. White dots in the x-ray are lead BBs used as markers to designate the top of the core (by placing three) and every 10 cm along the length of the core. Large black cavities mark the location of *Trapa* seed cases.

PT (75 - 95 cm)

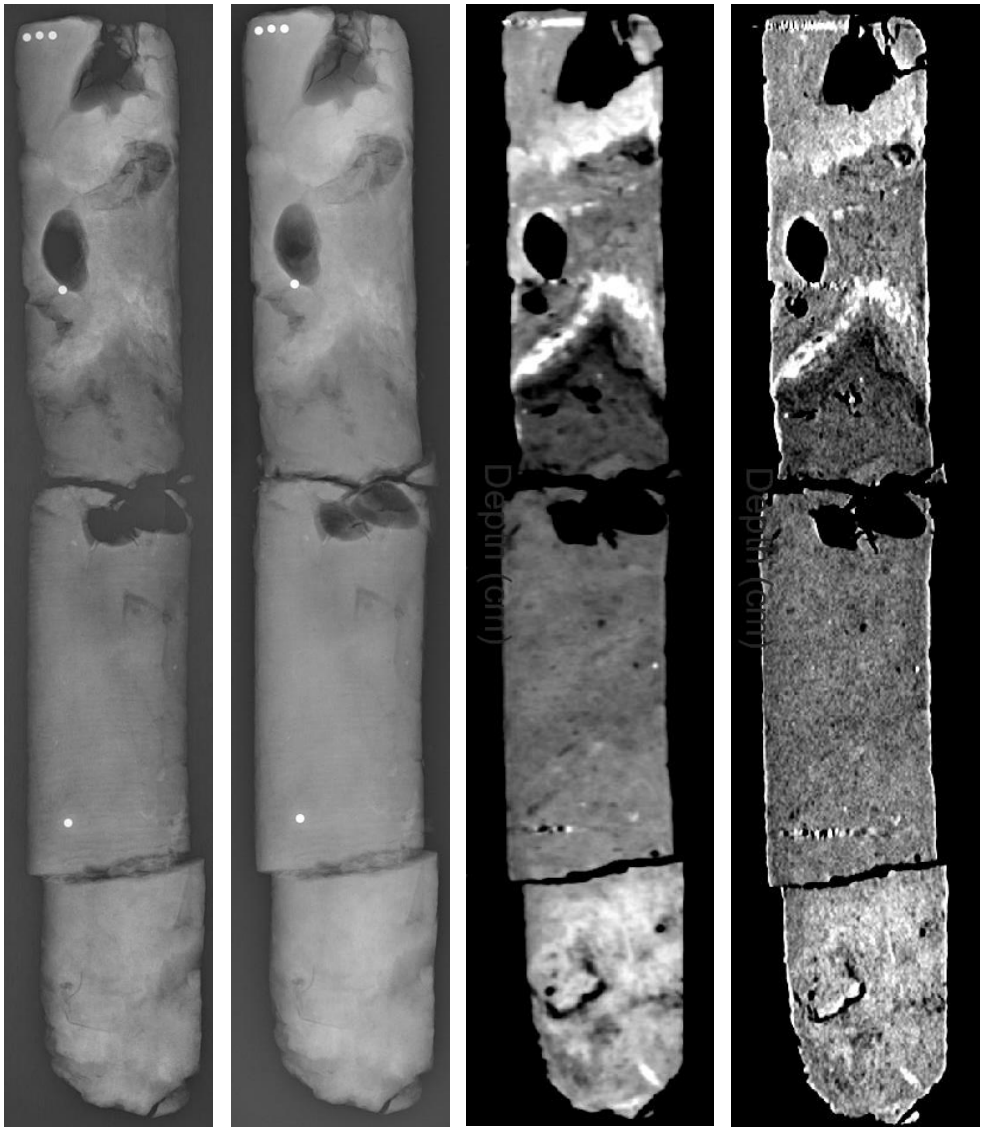

Abdomen X-ray | Right Extremity X-ray | Soft CT | Bone CT

Figure 2.12. Radiographs and compiled tomograms for Plastic Tube (PT) core. B) Four images of PT drive (75 — 95 cm) as captured using the abdomen and right extremity x-ray settings along with the stacked CT model produced by SedCT for both soft tissue and bone settings. White dots in the x-ray are lead BBs used as markers to designate the top of the core (by placing

three) and every 10 cm along the length of the core. Large black cavities mark the location of *Trapa* seed cases.

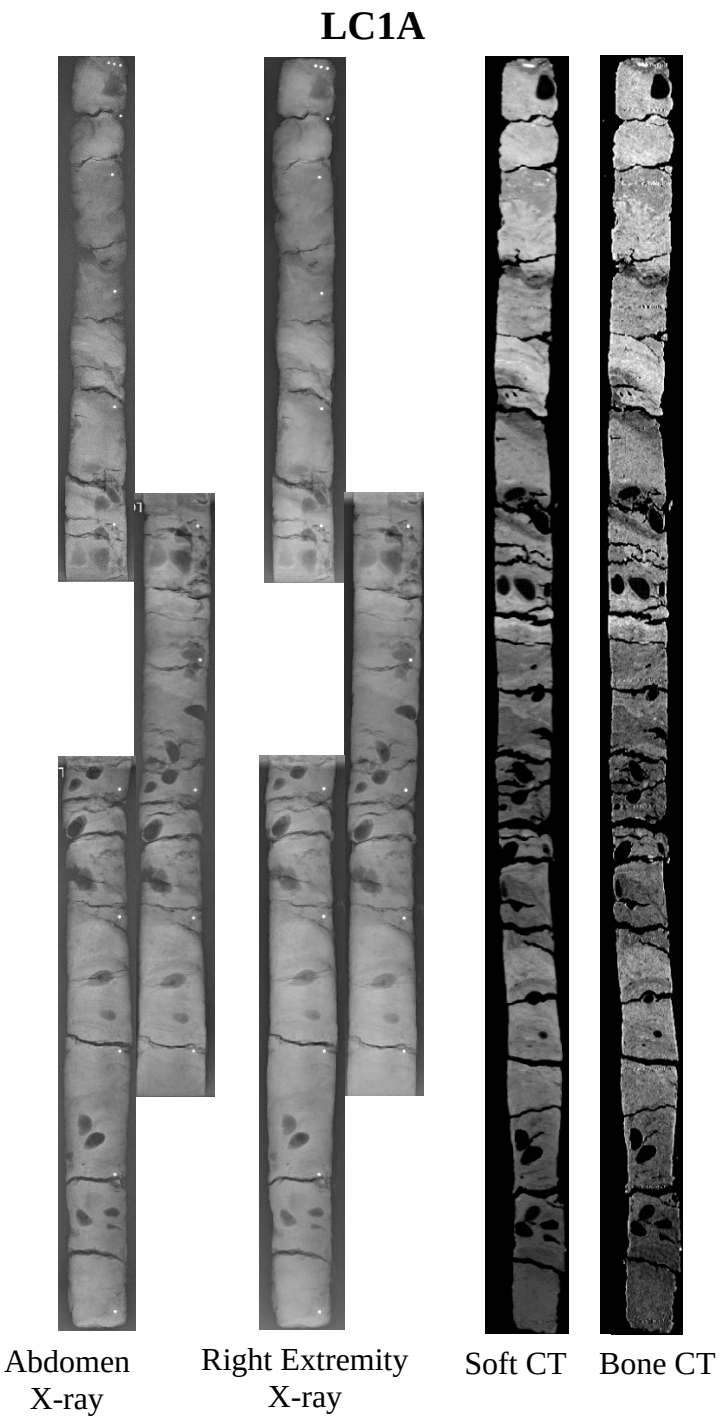

Figure 2.13. Radiographs and compiled tomograms for long core (LC). A) Eight images of LC1A drive (70 – 122 cm) as captured using the abdomen and right extremity x-ray settings along with the stacked CT model produced by SedCT for both soft tissue and bone settings.

White dots in the x-ray are lead BBs used as markers to designate the top of the core (by placing three) and every 10 cm along the length of the core. Large black cavities mark the location of *Trapa* seed cases.

Figure 2.13. Radiographs and compiled tomograms for long core (LC). B) Eight images of LC1B drive (165 – 257 cm) as captured using the abdomen and right extremity x-ray settings along with the stacked CT model produced by SedCT for both soft tissue and bone settings. White dots in the x-ray are lead BBs used as markers to designate the top of the core (by placing three) and

every 10 cm along the length of the core. Large black cavities mark the location of *Trapa* seed cases.

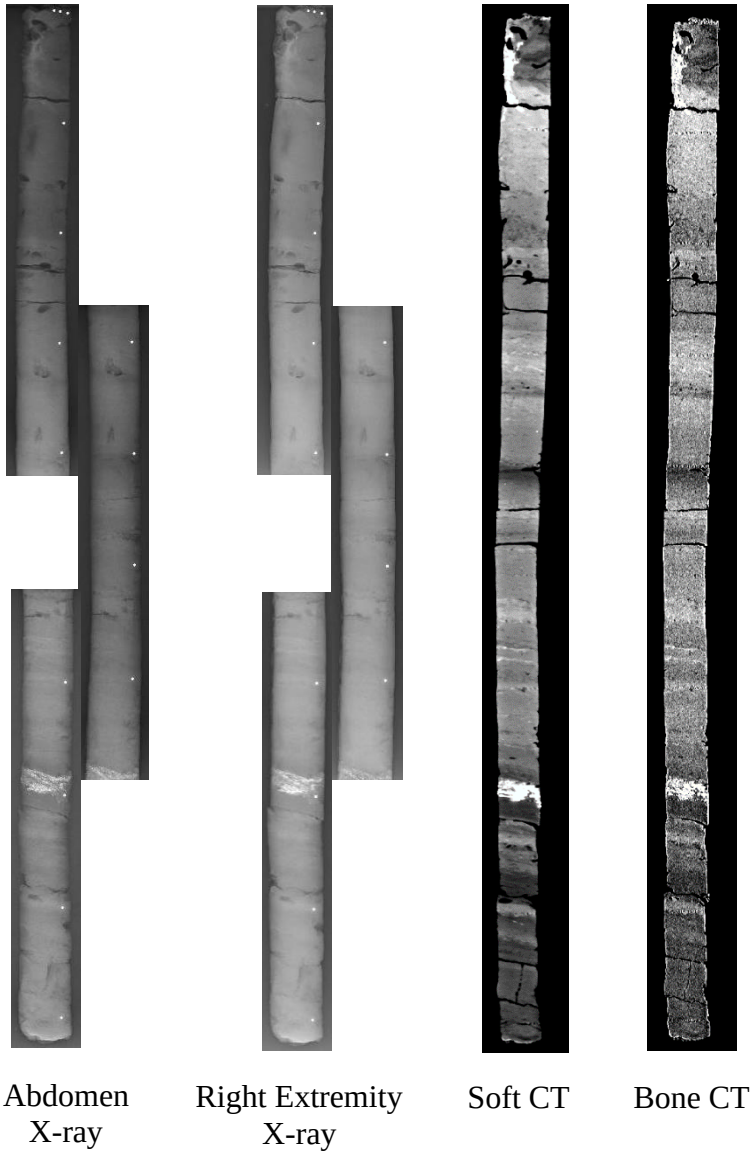

Figure 2.13. Radiographs and compiled tomograms for long core (LC). C) Eight images of LC1C drive (250 – 342 cm) as captured using the abdomen and right extremity x-ray settings along with the stacked CT model produced by SedCT for both soft tissue and bone settings. White dots in the x-ray are lead BBs used as markers to designate the top of the core (by placing three) and every 10 cm along the length of the core. Large black cavities mark the location of *Trapa* seed cases.

LC1D

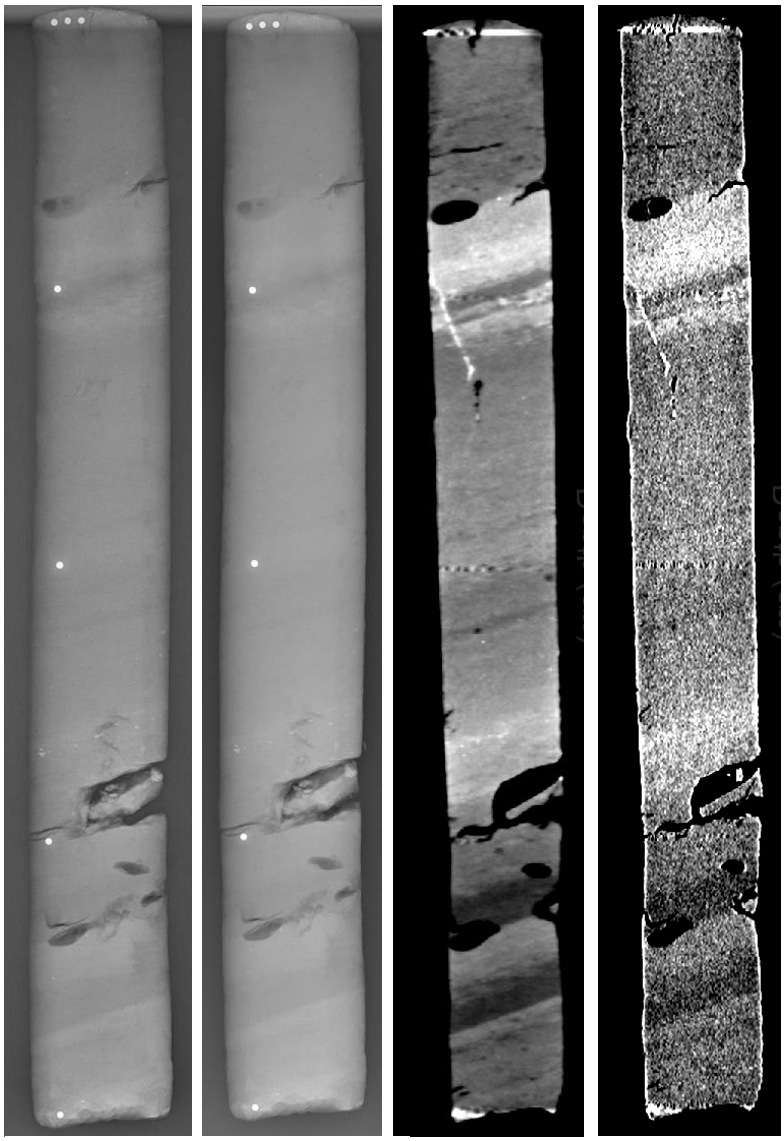

Figure 2.13. Radiographs and compiled tomograms for long core (LC). D) Eight images of LC1D drive (340 – 380 cm) as captured using the abdomen and right extremity x-ray settings along with the stacked CT model produced by SedCT for both soft tissue and bone settings. White dots in the x-ray are lead BBs used as markers to designate the top of the core (by placing

three) and every 10 cm along the length of the core. Large black cavities mark the location of *Trapa* seed cases.

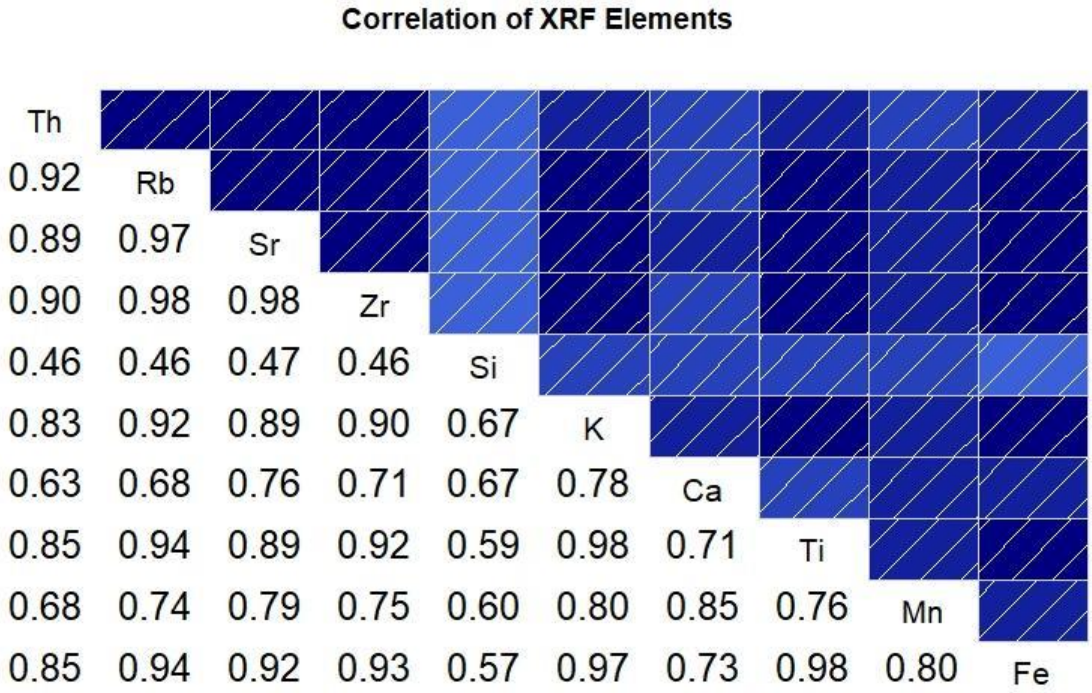

Figure 2.14. Correlogram for X-ray Fluorescence (XRF) elemental emission spectra. The correlogram's diagonal labels the corresponding row and column for their respective element analyzed with the pXRF. The bottom triangle lists the Spearman's Rho correlation coefficient for the various XRF elements with each other numerically (all with significant values of $p < 0.05$). The top triangle mirrors the same information as the bottom triangle, except the choropleth pictorially illustrates the strength of the correlation using the intensity of color and the direction of correlation with the gradient extending from red (negative) to blue (positive). Additionally, there is a white hash overlay on each color cell to designate direction with positive being in a forward slash direction (/) and negative being in a backslash direction (\).

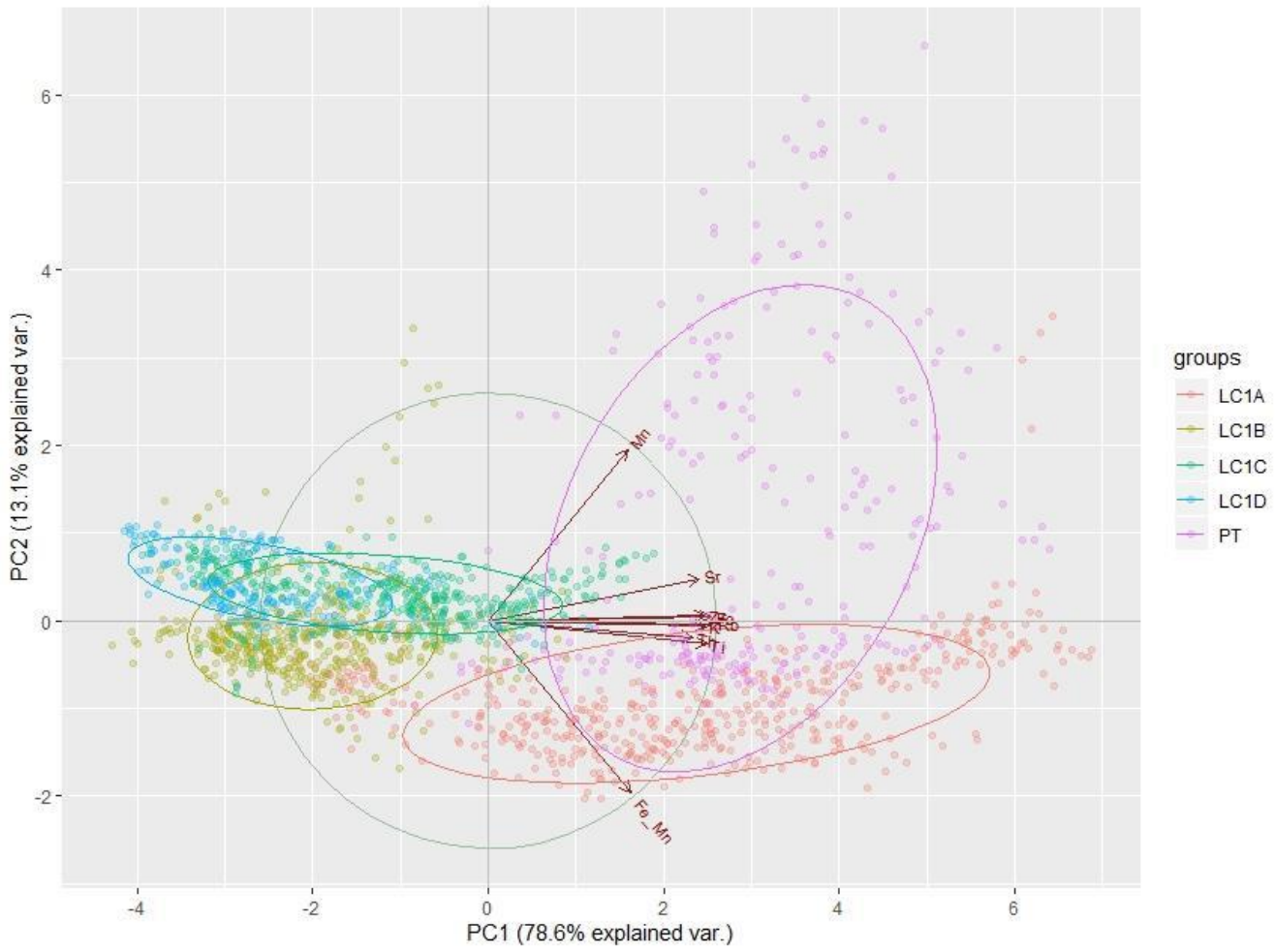

Figure 2.15. Principal Component Analysis (PCA) biplot for components. Principal component analysis (PCA) biplot depicting the ordination arrows for the filtered PCA results in brown and the ordination circle with the centering x- and y- axes included in grey. The observations are color-coded by drive and are grouped with their respective ellipses.

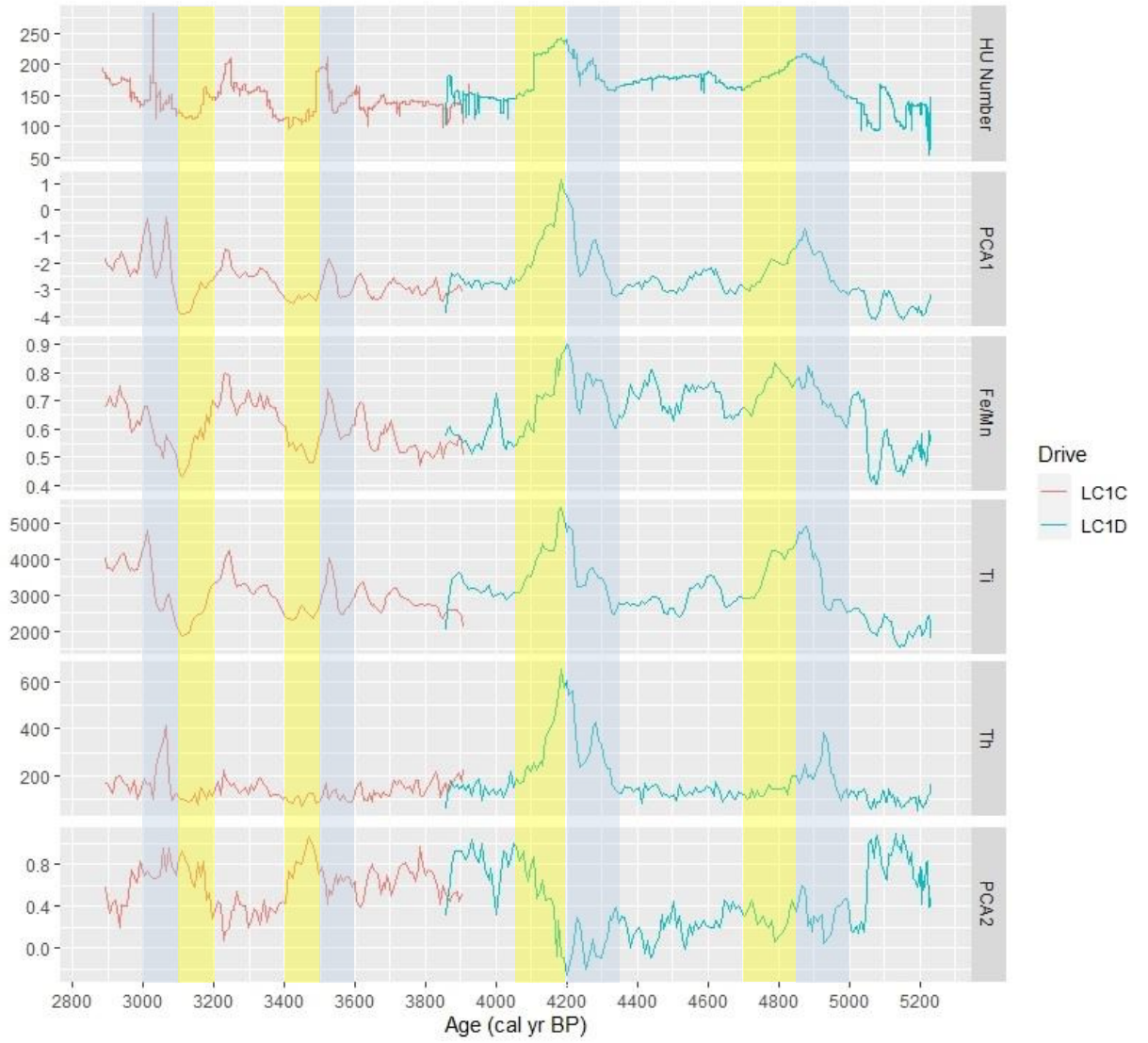

Figure 2.16. Summary multiproxy record of hydroclimate events. Anomalous hydroclimate events centered at 4850, 4200, 3500, and 3100 cal yr BP depicted by PCA scores, Z-scores of the HU number and Ti, and Fe/Mn. Periods of positive hydroclimate anomaly are highlighted in blue and periods of negative hydroclimate anomaly are highlighted in yellow.

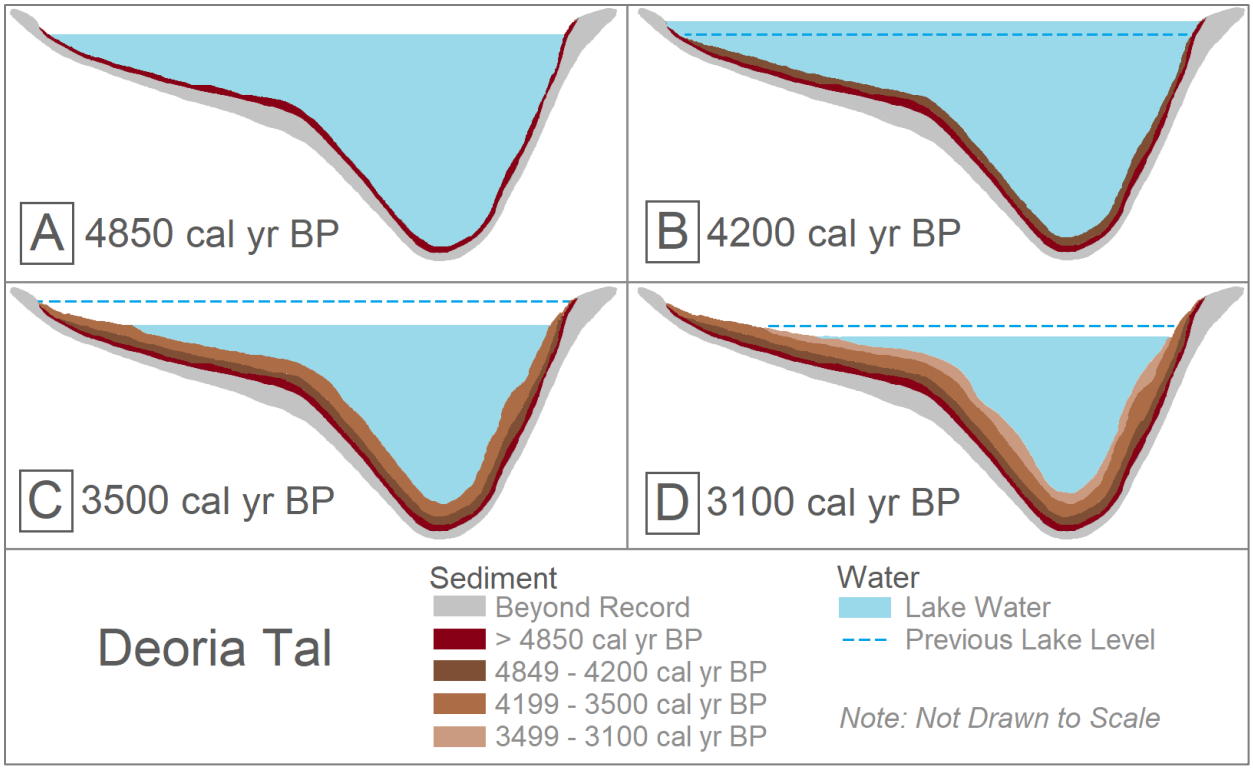

Figure 2.17. Pictorial illustration of lake response to abrupt hydroclimate events. The environmental interpretation of the lake hydrology during DRL-1 for (A) 4850 cal yr BP with a positive hydroclimate anomaly and elevated lake level (followed by a negative hydroclimate anomaly and lower lake level), (B) 4200 cal yr BP with an even larger positive hydroclimate anomaly and elevated lake level (followed by a negative hydroclimate anomaly and lower lake level), (C) 3500 cal yr BP with a positive hydroclimate anomaly and elevated lake level, although the lake level is lower relative to 4200 cal yr BP (followed by a negative hydroclimate anomaly and lower lake level), and (D) 3100 cal yr BP with a large negative hydroclimate anomaly and lower lake level (followed by a positive hydroclimate anomaly and elevated lake level).

CHAPTER 3

SUMMARY AND CONCLUSION

3.1 Review of Research Questions

The goal of this research was to use non-destructive, radiological approaches, i.e. X-ray fluorescence (XRF), X-Ray Imaging, and Computerized Tomography (CT) scans of a well-dated lake sediment core, recovered from a small, closed basin lake located in the Garhwal Himalaya to: (1) characterize regional hydroclimate variability during the mid- to late Holocene; (2) determine if evidence of an abrupt, short-lived climate event at 4200 cal yr BP is present at this site; and (3) use this record to determine whether there is a correspondence between hydroclimate variability during the late Holocene and Harappan metamorphosis.

Multi-proxy analysis of the sediment core from Deoria Tal, Uttarakhand, provides evidence for four episodes of notable hydroclimate change between 5200 and 3000 cal yr BP. These episodes, centered at 4850, 4200, 3500, and 3100 cal yr BP, were identified based on variations in elemental concentrations and sediment density. The events centered at 4850, 4200, and 3500 cal yr BP events were initially characterized by elevated detrital input, greater sediment density, and decreased lake ventilation, reflecting elevated lake level. These parameters then shift in an opposing direction suggesting the onset of lake level drawdown at 4850, 4200, and 3500 cal yr BP. The 3100 cal yr BP event was initially characterized by lower detrital flux, decreased sediment density, and increased oxygenation, reflecting lake drawdown. These parameters then shift in an opposing direction suggesting the onset of a positive lake mass balance at 3100 cal yr BP.

The most notable event evidenced at Deoria Tal between 5200 and 2000 cal yr BP occurs between 4350 and 4050 cal yr BP. This event is inferred to initially represent a deepening of the lake between 4350 and 4200 cal yr BP, followed by a rapid draw down of lake volume beginning at 4200 cal yr BP. The record generated in this study indicates that the 4200 year event in the Garhwal Himalaya was a two-step event: first characterized by a positive hydroclimate anomaly and elevated lake levels, followed by a centennial-scale drought event. Numerous studies suggest that the decrease in precipitation that occurred at 4200 cal yr BP was likely driven by a weakening of the Indian Summer Monsoon or ISM (Weiss, 2016; Tripathi et al., 2017). More recently it has been suggested that the negative hydroclimate anomaly evident immediately following 4200 cal yr BP can be explained by changes in the relative strength of the Indian Winter Monsoon or IWM, with a weakened IWM contributing to the regional drought culminating in the largest negative hydroclimate anomaly of the mid- to late Holocene in the Garhwal Himalaya (Wünnemann et al., 2010). The proxy record developed in this study cannot distinguish whether hydroclimate fluctuations were generated by variations in the ISM and/or IWM; however, it is notable that positive hydroclimate anomalies at DRL are generally associated with intervals of strengthened IWM (Giesche et al. 2019).

Broadly, the interval captured by DRL-1 (5200 – 3000 cal yr BP) falls within the middle of a climatic regime characterized by a weakening ISM (Peng et al., 2019; Kathayat et al. 2017). The trend of decreasing precipitation though the interval captured by DRL-1 was not gradual nor unidirectional. Notable hydroclimate anomalies characterized this interval with distinctive, discrete centennial-scale episodes of fluctuating hydroclimate (Leipe et al., 2014). DRL-1 is of particular interest because it spans the interval that captures the rise, expansion and eventual contraction of the Indus Civilization (Weiss 2016). Modeling and paleoenvironmental studies

suggest that the rapid, step-wise and sustained decline in population that characterized Harappa or Indus Valley Civilization, beginning at approximately 4200 cal yr BP, can be attributed to increasing water scarcity associated with changes in regional hydroclimate and a weakening of the ISM (MacDonald, 2011; Dixit et al., 2014; Leipe et al., 2014; Kotlia et al., 2015). According to Staubwasser et al. (2003), the 4200 cal yr BP event impacted the agricultural base of the agrarian society which likely contributed to the geographic and demographic contraction of the Harappa and may have ultimately led to demise of the civilization (Giosan et al., 2018). This study sheds light on the temporal relationship between hydroclimate anomalies and the contraction of Harappan civilization in northern India between 4500 cal yr BP and 3000 cal yr BP; however, it does not establish if the most severe, centennial-scale drought episode of the mid-Holocene, evidenced at Deoria Tal, ultimately precipitated the decline of the highly complex Harappan civilization.

3.2 Lessons Learned

The methodological approach used for the Deoria Tal record could be improved upon. After core collection, ideally the core should be radiographed with the X-ray and CT scanner first before being longitudinally split. After completing the radiological imaging, collecting the radiocarbon samples should be balanced with obtaining a uniformly planar surface for other imaging methodologies, including XRF and RBG scanning. The nondestructive methods should be completed as expediently as possible with proper core preservation and handling methods, including climate-controlled storage in a walk-in cooler to avoid shrinkage. Furthermore, the core should be measured in length to quantify how much shrinkage occurred between when the core was originally recovered and scanned so that the proxy results can be corrected as necessary

for any shrinkage. Following the nondestructive imaging and the collection of material for radiocarbon dating, destructive methods can be utilized.

By expediently scanning the core sample before latitudinally splitting the core, it should be possible to identify possible radiocarbon samples for collection with predetermined intentionality rather than waiting until sectioning to identify the location of suitable material. This increases the chance for maximizing the number of radiocarbon samples that could be collected from the core. Furthermore, by following this adjusted sequence of methodology and potentially including more analytical instrumentation, the number of potential quantifiable proxies that can be used for core evaluation would likely increase. Whether the data collection of the sediment cores was completed using a core scanner or resulted from a series of images stitched together utilizing photogrammetric techniques, the methodologies for image acquisition (Lamoureux and Bollmann, 2004; Yang et al., 2016), processing (Nederbragt et al., 2004), measurements (Pirard, 2004), and error assessment (Francus and Pirard, 2004) are quite communicable for X-ray, visible light (mounted spectrophometer, camera, etc.), and other wavelengths of the electromagnetic spectrum. Depending on the exact methodologies enacted, some results could include greyscale (Sáez et al., 2009; Francus et al., 2015), color reflectance (St-Onge et al., 2007), and/or grain size (Pirard, 2004; St-Onge et al., 2007) record(s) for paleoenvironmental interpretation. Additionally, if a CT scanner is a part of the methodology, sediment density (g/cm^3) could also be included (Flisch and Becker, 2003; Reilly et al., 2017).

3.3 Future Research Opportunities

Further information that would improve the paleoenvironmental reconstruction for Deoria Tal would be a comprehensive study of the bathymetry of the lake and the collection of a series of cores along a transect following Shuman et al. (2001). From the non-destructive

analyses of the Deoria Tal record, the paleoenvironmental record is inferred to capture extensive lake level changes. The new series of cores could utilize the proposed non-destructive, radiological methodology to recover a quantifiable grainsize and sediment density record (Flisch and Becker, 2003; Reilly et al., 2017), in addition to destructive sampling methodologies (loss-on-ignition, chironomids, pollen, etc.) and estimated sediment accumulation rates to reconstruct a refined lake-level record (Shuman et al., 2001). The refined lake-level record together with a detailed understanding of the bathymetry of the lake could in turn be used to quantitatively model changes in the mass balance of Deoria Tal in response to hydroclimate variations.

The high-resolution record generated in this study could be tested by collecting new lake sediment cores from the Garhwal and Kumaon Himalaya. These new cores could be analyzed using the methodology utilized in this study to determine if evidence of hydroclimate anomalies at 4850, 4200, 3500 and 3100 cal yr BP are evident regionally (Dixit and Tandon, 2016; Kar and Qumar, 2019). The incorporation of additional proxies including chironomids, pollen, charcoal and stable isotopes (^{13}C and ^{18}O) would enable the development of a more robust and holistic paleoenvironmental reconstruction for Deoria Tal.

Petrie et al. (2017) identified "gaps" that were necessary to adequately evaluate the contribution of environmental versus human factors respectively on the demise of the Harappan Civilization and specifically "high-resolution climatic and environmental evidence" at the local or regional scale. Much of the "debate" heretofore focused on juxtaposing global-scale climate records with the local-scale Harappan society interactions as uncovered through the archaeological record even though justification to do so is largely lacking (Petrie et al., 2017). However, if local and/or regional specific climatic records with enough resolution were

available, such as with the derived paleoclimatic record from this study and the proposed future research opportunities, further progress on addressing this question could be made.

3.4 Significance of Research and Conclusion

With a fuller understanding of the paleoclimate regime over the mid- to late Holocene, a potentially stronger comparison could be made with the various civilizations that inhabited the Indian subcontinent over the same time period. This includes ancient civilizations such as the Harappa but it also includes people living in India and neighboring countries today. For example, Bryson and Baerreis (1967) specifically utilized the juxtaposition of the Harappan civilization with the modern day by assessing the relative role of desertification, agricultural activity and hydroclimate variability on the expansion and contraction of the Harappa. Further improving our understanding of regional climate and its variability allows for better understanding climatic influence on human civilizations in the past. With improved understanding of the past, the principles can be applied further to provide much-needed comparative data in assessing and anticipating the impacts associated with projected regional climate change—particularly in this region. The record developed in this study provides a longer-term context for understanding the capacity of a highly urbanized and centralized society to respond to water resource challenges such as those anticipated to affect the regionally significant water resources that are at risk due to projected climate change (Ponton et al., 2012; Schug et al., 2013). Insight into possible applications of various mechanisms in the context of climatic and cultural change can be drawn from the past only if the knowledge of the past is available to draw from (Bryson, 1988).

REFERENCES

An, F., Lai, Z., Liu, X., Wang, Y., Chang, Q., Lu, B., and Yang, X. 2018. Luminescence Chronology and Radiocarbon Reservoir Age Determination of Lacustrine Sediments from the Heihai Lake, NE Qinghai-Tibetan Plateau and Its Paleoclimate Implications. Journal of Earth Science, 3(29), 695-706.

Ankit, Y., Kumar, P., Anoop, A., Mishra, P.K., and Varghese, S. 2017. Mid-late Holocene climate variability in the Indian monsoon: Evidence from continental shelf sediments adjacent to Rushikulya river, eastern India. Quaternary International, 443, 155-163.

Bist, K.S., and Sinha, A.K. 1980. Some observations on the geological and structural setup of Okhimath area in Garhwal Himalaya. Himalayan geology, 10, 467-475.

Blaauw, M. and Christen, J.A. 2011. Flexible paleoclimate age-depth models using an autoregressive gamma process. Bayesian Analysis, 6, 457-474.

Bohra, A. and Kotlia, B.S. 2015. Tectono-climatic signatures during Late Quaternary in the Yunam basin, Baralacha Pass (upper Lahaul valley, India), derived from multi-proxy records. Quaternary International, 371, 111-121.

Bollasina, M.A., Ming, Y., and Ramaswamy, V. 2011. Anthropogenic Aerosols and the Weakening of the South Asian Summer Monsoon. Science, 334(6055), 502-505.

Bolton, C.T., Chang, L., Clemens, S.C., Kodama, K., Ikehara, M., Medina-Elizalde, M., Paterson, G.A., Roberts, A.P., Rohling, E.J., Yamamoto, Y., and Xhao, X. 2013. A 500,000 year record of Indian summer monsoon dynamics recorded by eastern equatorial Indian Ocean upper water-column structure. Quaternary Science Reviews, 77, 167-180.

Booth, R.K., Jackson, S.T., Forman, S.L., Kutzbach, J.E., Bettis III, E.A., Kreigs, J., and Wright, D.K. 2005. A severe centennial-scale drought in midcontinental North America 4200 years ago and apparent global linkages. The Holocene, 15(3), 321-328.

Bronk Ramsey, C. 2017. OxCal Program, Version 4.3. Oxford Radiocarbon Accelerator Unit: University of Oxford. <https://c14.arch.ox.ac.uk/oxcal.html>

Bryson, R.A., and Baerreis, D.A. 1967. possibilities of major climatic modification and their implications: Northwest India, a case for study. Bulletin of the American Meteorological Society, 48(3), 136-142.

Bryson, R.A., and Murray, T.J. 1977. A Manmade Desert. In Climates of Hunger. Australian National University Press, Canberra, 107-114.

Bryson, R.A. 1988. Civilization and Rapid Climatic Change. Environmental Conservation, 15(1), 7-15.

Chassiot, L., Miras, Y., Chapron, E., Develle, A.L., Arnaud, F., Motelica-Heino, M., Giovanni, C.D. 2018. A 7000-year environmental history and soil erosion record inferred from the deep sediments of Lake Pavin (Massif Central, France). Palaeogeography, Palaeoclimatology, Palaeoecology, 497, 218-233.

Chatterjee, A. and Ray, J.S. 2017. Sources and depositional pathways of mid-Holocene sediments in the Great Rann of Kachchh, India: Implications for fluvial scenario during the Harappan Culture. Quaternary International, 443, 177-187.

Chaudhary, S., Gupta, V., and Sundriyal, Y.P. 2010. Surface and sub-surface characterization of Byung landslide in Mandakini valley, Garhwal Himalaya. Himalayan Geology, 31(2), 125-132.

Chauhan, M.S. and Sharma, C. 2000. Late Holocene vegetation and climate in Dewar Tal area, Inner Lesser Garhwal Himalaya. The Palaeobotanist, 49, 509-514.

Chauhan, M.S., Pokharia, A.K., and Srivastava, R.K. 2015. Late Quaternary vegetation history, climatic variability and human activity in the Central Ganga Plain, deduced by pollen proxy records from Karela Jheel, India. Quaternary International, 371, 144-156.

Cherkashina, T.Yu., Panteeva, S.V., and Pashkova, G.V. 2014. Applicability of direct total reflection X-ray fluorescence spectrometry for multielement analysis of geological and environmental objects. Spectrochimica Acta Part B, 99, 59-66.

Climate-Data. n.d. Chamoli Gopeshwar Climate (India). Climate-Data. Accessed 10 June 2021. Retreived from https://en.climate-data.org/asia/india/uttarakhand/chamoli-gopeshwar-33832/.

Cuven, S., Francus, P., and Lamoureux, S. 2011. Mid to Late Holocene hydroclimatic and geochemical records from the varved sediments of East Lake, Cape Bounty, Canadian High Arctic. Quaternary Science Reviews, 30, 2651-2665.

Davies, S.J., Lamb, H.F., and Roberts, S.J. 2015. Micro-XRF Core Scanning in Palaeolimnology: Recent Developments. In Micro-XRF Studies of Sediment Cores. Editors Croudace, I.W., and Rothwell, R.G. Springer, New York, 17, 189-226.

Demske, D., Tarasov, P.E., Leipe, C., Kotlia, B.S., Joshi, L.M., and Long, T. 2016. Record of vegetation, climate change, human impact and retting of hemp in Garhwal Himalaya (India) during the past 4600 years. The Holocene, 26(10), 1661-1675.

Dimri, A.P., Yasunari, T., Kotlia, B.S., Mohanty, U.C., and Sikka, D.R. 2016. Indian winter monsoon: Present and past. Earth-Science Reviews, 163, 297-322.

Dixit, Y., Hodell, D.A., and Petrie, C.A. 2014. Abrupt weakening of the summer monsoon in northwest India ~4100 yr ago. Geology, 42(4), 339-342.

Dixit, Y., and Tandon, S. K. 2016. Hydroclimatic variability on the Indian subcontinent in the past millennium; review and assessment. Earth-Science Reviews, 161, 1-15.

Dutt, S., Gupta, A.K., Wünnemann, B., and Yan, D. 2018. A long arid interlude in the Indian summer monsoon during ~4,350 to 3,450 cal. yr BP contemporaneous to displacement of the Indus valley civilization. Quaternary International, 482, 83-92.

Elder, J.F. 1988. Metal Biogeochemistry in Surface-Water Systems—A Review of Principles and Concepts. Department of the Interior, United States Geological Survey, 1013.

Enzel, Y., Ely, L.L., Mishra, S., Amit, R., Lazar, B., Rajaguru, S.N., Baker, V.R., and Sandler, A. 1999. High-Resolution Holocene Environmental Changes in the Thar Desert, Northwestern India. Science, 284(5411), 125-128.

Farooqui, A., Gaur, A.S., and Prasad, V. 2013. Climate, vegetation and ecology during Harappan period: excavations at Kanjetar and Kaj, mid-Saurashtra coast, Gujarat. Journal of Archaeological Science, 40, 2631-2647.

Flisch, A. and Becker, A. 2003. Industrial X-ray computed tomography studies of lake sediment drill cores. In Applications of X-ray Computed Tomography in the Geosciences. The Geological Society of London, London, Special Publications, 215, 205-212.

Fouinat, L., Sabatier, P., Poulenard, J., Reyss, J., Montet, X., and Arnaud, F. 2017. A new CT scan methodology to characterize a small aggregation gravel clast contained in a soft sediment matrix. Earth Surface Dynamics, 5, 199-209.

Francus, P., Kanamaru, K., and Fortin, D. 2015. Standardization and Calibration of X-Radiographs Acquared with the ITRA Core Scanner. In Micro-XRF Studies of Sediment Cores. Editors Croudace, I.W., and Rothwell, R.G. Springer, New York, 17, 491-505.

Francus, P., and Pirard, E. 2004. Testing for sources of errors in quantitative image analysis. In Image Analysis, Sediments and Paleoenvironments. Editor Francus, P. Springer Science and Business Media, Dordrecht, 7, 87-102.

Gadgil, S. 2003. The Indian Monsoon and Its Variability. Annual Review of Earth Planetary Sciences, 31, 429-467.

Gadgil, S. and Gadgil S. 2006. The Indian Monsoon, GDP, and Agriculture. Economic and Political Weekly, 41(47), 4887+4889-4895.

Gadgil, S. and Srinivasan, J. 2011. Seasonal prediction of the Indian monsoon. Current Science, 100(3), 343-353.

Gadgil, S., Vinayachandran, P.N., and Francis, P.A. 2003. Droughts of the Indian summer monsoon: Role of clouds over the Indian Ocean. Current Science, 85(12), 1713-1719.

Giesche, A., Staubwasser, M., Petrie, C.A., and Hodell, D.A. 2019. Indian winter and summer monsoon strength over the 4.2 ka BP event in foraminifer isotope records from the Indus River delta in the Arabian Sea. Climate of the Past, 15, 73-90.

Giosan, L., Clift, P.D. Macklin, M.G., Fuller, D.Q., Constantinescu, S., Durcan, J.A., Stevens, T., Duller, G.A.T., Tabrez, A.R., Gangal, K., Adhikari, R., Alizai, A., Filip, F., VanLaningham, S., and Syvitski, J.P.M. 2012. Fluvial landscapes of the Harappan civilization. Proceedings of the National Academy of Sciences, 109(26), E1688-1694.

Giosan, L., Orsi, W.D., Coolen, M., Wuchter, C., Dunlea, A.G., Thirumalai, K., Munoz, S.E., Clift, P.D., Donnelly, J.P., Galy, V., and Fuller, D.Q. 2018. Neoglacial climate anomalies and the Harappan metamorphosis. Climate of the Past, 14, 1669-1686.

Google. n.d. Deoria Tal and Surrounding Area. Google Earth. Accessed 13 March 2019. Retrieved from <https://earth.google.com/web/@30.59968314,79.08840904,1663.89671952a,25440.90788344d,35y,24.6608536h,60.09184095t,-0r?utm_source=referral&utm_campaign=hpp&utm_term=carmen1>

Goswami, B.N. and Chakravorty, S. 2017. Dynamics of the Indian Summer Monsoon Climate. Climate Systems and Climate Dynamics, Oxford Research Encyclopedia of Climate Science, 1-39.

Goswami, B.N., Venugopal, V., Sengupta, D., Madhusoodanan, MS.S., and Xavier, P.K. 2006. Increasing Trend of Extreme Rain Events Over India in a Warming Environment. Science, 314(5804), 1442-1445.

Gray, L.J., Beer, J., Geller, M., Haigh, J.D., Lockwood, M., Matthes, K., Cubasch, U., Fleitmann, D., Harrison, G., Hood, L., Luterbacher, J., Meehl, G.A., Shindell, D., van Geel, B., and White, W. 2010. Solar Influences on Climate. Reviews of Geophysics, 48(4).

Gupta, A.K., Anderson, D.M., and Overpeck, J.T. 2003. Abrupt changes in the Asian southwest monsoon during the Holocene and their links to the North Atlantic Ocean. Letters to Nature, 421, 354-357.

Gupta, A.K., Anderson, D.M., Pandey, D.N., and Singhvi, A.K. 2006. Adaptation and human migration, and evidence of agriculture coincident with changes in the Indian summer monsoon during the Holocene. Current Science, 90(8), 1082-1090.

Günther, F., Witt, R., Schouten, S., Mäusbacher, R., Daut, G., Zhu, L., Xu, B., Yao, T., and Gleixner, G. 2015. Quaternary ecological responses and impacts of the Indian Ocean Summer Monsoon at Nam Co, Southern Tibetan Plateau. Quaternary Science Reviews, 112, 66-77.

Hadden, C. 2021, May. Personal Communication.

Haenssler, E., Nadeau, M.J., Vött, A., and Unkel, I. 2013. Natural and human induced environmental changes preserved in a Holocene sediment sequence from the Etliko Lagoon, Greece: New evidence from geochemical proxies. Quaternary International, 308-309, 89-104.

Hahn, A., Kliem, P., Oehlerich, M., Ohlendorf, C., and Zolitschka, B., and the PASADO Science Team. 2014. Elemental composition of the Laguna Potrok Aike sediment sequence reveals paleoclimatic changes over the past 51 ka in southern Patagonia, Argentina. Journal of Paleolimnology, 52, 349-366.

Haug, G.H., Günther, D., Peterson, L.C., Sigman, D.M., Hughen, A., and Aeschlimann, B. 2003. Climate and the Collapse of Maya Civilization. Science, 5613(299), 1731-7135.

Hendy, I.L., Napier, T.J., and Schimmelmann, A. 2015. From extreme rainfall to drought: 250 years of annually resolved sediment deposition in Santa Barbara Basin, California. Quaternary International, 387, 3-12.

Heymann, C., Nelle, O., Dörfler, W., Zagana, H., Nowaczyk, N., Xue, J., and Unkel, I. 2013. Late Glacial to mid-Holocene palaeoclimate development of Southern Greece inferred

from the sediment sequence of Lake Stymphalia (NE-Peloponnese). Quaternary International, 302, 42-60.

Hummel, M. and Kiviat, E. 2004. Review of World Literature on Water Chestnut with Implications for Management in North America. Journal of Aquatic Plant Management, 42, 17-28.

Hunt, A.M.W. and Speakman, R.J. 2015. Portable XRF analysis of archaeological sediments and ceramics. Journal of Archaeological Science, 53, 626-638.

Islam, M.A., Chattoraj, S.L., and Champati R.P.K. 2014. Ukhimath landslide 2012 at Uttarakhand, India: Causes and consequences. International Journal of Geomatics and Geosciences, 4(3), 544-557.

Kar, R. and Quamar, M.F. 2019. Pollen-based Quaternary palaeoclimatic studies in India: an overview of recent advances. Palynology, 43(1), 76-93.

Kholia, N. and Kotlia, B.S. 2018, August. Personal Communication.

Kotlia, B.S., Singh, A.K., Joshi, L.M., and Dhaila, B.S. 2015. Precipitation variability in the Indian Central Himalaya during last ca. 4,000 years inferred from a speleothem record: Impact of Indian Summer Monsoon (ISM) and Westerlies. Quaternary International, 371, 244-253.

Kotlia, B.S., Singh, A.K., Zhao, J., Duan, W., Tan, M., Sharma, A.K., and Raza, W. 2017. Stalagmite based high resolution precipitation variability for past four centuries in the Indian Central Himalaya: Chulerasim cave re-visited and data re-interpretation. Quaternary International, 444, 35-43.

Kotlia, B.S. 2019, February. Personal Communication.

Kothyari, G.Ch., Shukla, A.D., and Juyal, N. 2017. Reconstruction of Late Quaternary climate and seismicity using fluvial landforms in Pindar River valley, Central Himalaya, Uttarakhand, India. Quaternary International, 443, 248-264.

Lamoureux, S.F., and Bollmann, J. 2004. Image acquisition. In Image Analysis, Sediments and Paleoenvironments. Editor Francus, P. Springer Science and Business Media, Dordrecht, 7, 11-34.

Leipe, C., Demske, D., Tarasov, P.E., and HIMPAC Project Members. 2014. A Holocene pollen record from the northwestern Himalayan lake Tso Moriri: Implications for palaeoclimatic and archaeological research. Quaternary International, 348, 93-112.

MacDonald, G. 2011. Potential influence of the Pacific Ocean on the Indian summer monsoon and Harappan decline. Quaternary International, 229, 140-148.

Madella, M. and Fuller, D.Q. 2006. Palaeoecology and the Harappan Civilisation of South Asia: a reconsideration. Quaternary Science Reviews, 25, 1283-1301.

Menzel, P., Gaye, B., Mishra, P.K., Anoop, A., Basavaiah, N., Marwan, N., Plessen, B., Prasad, S., Riedel, N., Stebich, M., and Wiesner, M.G. 2014. Linking Holocene drying trends from Lonar Lake in monsoonal central India to North Atlantic cooling events. Palaeogeography, Palaeoclimatology, Palaeoecology, 410, 164-178.

Midhun, M. and Ramesh, R. 2016. Validation of δ18O as a proxy for past monsoon rain by multi-GCM simulations. Climate Dynamics, 46, 1371-1385.

Nederbragt, A.J., Francus, P., Bollmann, J., and Soreghan, M.J. 2004. Image calibration, filtering and processing. In Image Analysis, Sediments and Paleoenvironments. Editor Francus, P. Springer Science and Business Media, Dordrecht, 7, 35-58.

Niederman, E. 2019, February 13. Trapa seed case. Image.

Olsen, J., Anderson, J.N., and Leng, M.J. 2013. Limnological controls on stable isotope records of late-Holocene palaeoenvironment change in SW Greenland: a paired lake study. Quaternary Science Review, 66, 85-95.

Olsen, J., Björck, S., Leng, M.J., Gudmundsdóttir, E.R., Odgaard, B.V., Lutz, C.M., Kendrick, C.P., Andersen, T.J., and Seidenkrantz, M.S. 2010. Lacustrine evidence of Holocene environmental change from three Faroese lakes: a multiproxy XRF and stable isotope study. Quaternary Science Reviews, 29, 2764-2780.

Patwardhan, S., Kulkarni, A., and Sabade, S. 2016. Projected Changes in Semi Permanent System of Indian Summer Monsoon in CORDEX-SA framework. American Journal of Climate Change, 5, 133-146.

Paul, S., Ghosh, S. Oglesby, R., Pathak, A., Chandrasekharan, A., and Ramsankaran, R.A.A.J. 2016. Weakening of Indian Summer Monsoon Rainfall due to Changes in Land Use Land Cover. Scientific Reports, 6, 32177.

Peng, Jie, Yang, X., Toney, J.L., Ruan, J., Li, G., Zhou, Q., Gao, H., Xie, Y., Chen, Q., and Zhang, T. 2019. Indian Summer Monsoon variations and competing influences between hemispheres since ~35 ka recorded in Tengchongqinghai Lake, southwestern China. Palaeogeography, Palaeoclimateology, Palaeoecology, 516, 113-125.

Petrie, C.A., Singh, R.N., Bates, J., Dixit, Y., French, C.A.I., Hodell, D.A., Jones, P.J., Lancelotti, Ca., Lynam, F., Neogi, S., Pandey, A.K., Parikh, D., Pawar, V., Redhouse, D.I., and Singh, D.P. 2017. Adaptation to Variable Environments, Resilience to Climate Change. Current Anthropology, 58(1), 1-30.

Pirard, E. 2004. Image measurements. In Image Analysis, Sediments and Paleoenvironments. Editor Francus, P. Springer Science and Business Media, Dordrecht, 7, 59-86.

Ponton, C., Giosan, L., Eglinton, T.I., Fuller, D.Q., Johnson, J.E., Kumar, P., and Collett, T.S. 2012. Holocene aridification in India. Geophysical Research Letters, 39, L03704.

Porinchu, D. 2018, May 8. Deoria Tal. Image.

Prasad, S., Kusumgar, S., and Gupta, S.K. 1997. A mid to late Holocene record of palaeoclimatic changes from Nal Sarovar: a palaeodesert margin lake in western India. Journal of Quaternary Science, 12(2), 153-159.

Rajani, M.B. and Rajawat, A.S. 2011. Potential of satellite based sensors for studying distribution of archaeological sites along palaeo channels: Harappan sites a case study. Journal of Archaeological Science, 38, 2010-2016.

Reilly, B.T., Stoner, J.S., and Wiest, J. 2017. SedCT: MATLAB™ tools for standardized and quantitative processing of sediment core computed tomography (CT) data collected using a medical CT scanner. Geochemistry, Geophysics, Geosystems, 18(8), 3231-3240.

Reimer, P. J., Bard, E., Bayliss, A., Beck, J. W., Blackwell, P. G., Bronk Ramsey, C., Buck, C.E., Cheng, H., Edwards, R.L., Friedrich, M., Grootes, P.M., Guilderson, T.P., Haflidason, H., Hajdas, I., Hatté, C., Heaton, T.J., Hoffmann, D.L., Hogg, A.G., Hughen, K.A., Kaiser, K.F., Kromer, B., Manning, S.W., Niu, M., Reimer, R.W., Richards, D.A., Scott, E.M., Southon, J.R., Staff, R.A., Turney, C.S.M., and van der Plicht, J. 2013. IntCal13 and Marine13 radiocarbon age calibration curves 0–50,000 years cal BP. Radiocarbon, 55(4), 1869-1887.

Sáez, A., Valero-Garcés, B.L., Giralt, S., Moreno, A., Bao, R., Pueyo, J.J., Hernández, A., and Casas, D. 2009. Glacial to Holocene climate changes in the SE Pacific. The Raraku Lake sedimentary record (Easter Island, 27° S). Quaternary Science Reviews, 28, 2743-2759.

Sanwal, J., Kotlia, B.S., Rajendran, C., Ahmad, S.M., Rajendran, K., and Sandiford, M. 2013. Climatic variability in Central Indian Himalaya during the last 1800 years: Evidence from a high resolution speleothem record. Quaternary International, 304, 183-192.

Sarkar, A., Mukherjee, A.D., Bera, M.K., Das, B., Juyal, N., Morthekai, P., Deshpande, R.D., Shinde, V.S., and Rao, L.S. 2016. Oxygen isotope in archaeological bioapatites from India: Implications to climate change and decline of Bronze Age Harappan civilization. Nature Scientific Reports, 6, 26555.

Saxena, A. and Singh, D.S. 2017. Multiproxy records of vegetation and monsoon variability from the lacustrine sediments of eastern Ganga Plain since 1350 A.D. Quaternary International, 444, 24-34.

Schmidt, M., Leipe, C., Becker, F., Goslar, T., Hoelzmann, P., Mingram, J., Müller, S., Tjallingii, R., Wagner, M., and Tarasov, P.E. 2019. A multi-proxy palaeolimnological record of the last 16,600 years from coastal Lake Kushu in northern Japan. Palaeogeography, Palaeoclimatology, Palaeoecology, 514, 613-626.

Schug, G.R., Belvins, K.E., Cox, B., Gray, K., and Mushrif-Tripathy, V. 2013. Infection, Disease, and Biosocial Processes at the End of the Indus Civilization. PloS One, 8(12), e84814.

Sharma, C. and Gupta, A. 1997. Vegetation and climate in Garhwal Himalaya during EarlyHolocene : Deoria Tal. The Palaeobotanist, 46(3), 111-116.

Sharma, C., Chauhan, M.S., and Rajagopalan, G. 2000. Vegetation and climate in Garhwal Himalaya during last 4,000 years. The Palaeobotanist, 49(3), 501-507.

Shuman, B., Bravo, J., Kaye, J., Lynch, J.A., Newby, P., and Webb, T., III. 2001. Late Quaternary Water-Level Variations and Vegetation History at Crooked Pond, Southeastern Massachusetts. Quaternary Research, 56, 401-410.

Singh, D., Tsiang, M., Rajaratnam, B., and Diffenbaugh, N.S. 2014. Observed changes in extreme we and dry spells during the South Asian summer monsoon season. Nature Climate Change, 4(6), 456-461.

Singh, V., Yadav, R.R., Gupta, A.K., Kotlia, B.S., Singh, J., Yadava, A.K., Singh, A.K., and Misra, K.G. 2017. Tree ring drought records from Kishtwar, Jammu and Kashmir, northwest Himalaya, India. Quaternary International, 444, 53-64.

St-Onge, G., Mulder, T., Francus, P., and Long, B. 2007. Continuous Physical Properties of Cored Marine Sediments. In Proxies in Late Cenozic Paleoceanography. Editors Hillaire-Marcel, C., and De Vernal, A. Elsevier Science and Technology, Amsterdam, 1, 63-98.

Staubwasser, M., Sirocko, F., Grootes, P.M., and Segl, M. 2003. Climate change at the 4.2 ka BP termination of the Indus valley civilization and Holocene south Asian monsoon variability. Geophysical Research Letters, 30(8), 1425.

Tripathi, D., Chauhan, D.K., Farooui, A., Kotlia, B.S., Thakur, B., Morthekai, P., Long, T., Chauhan, M.S., and Pokharia, A.K. Late Quaternary climatic variability in the Central Ganga Plain: A multi-proxy record from Karela Jheel (Lake). Quaternary International, 443, 70-85.

Turner, A.G. and Hannachi, A. 2010. Is there regime behavior in monsoon convection in the late 20th century?. Geophysical Research Letters, 37(16), L16706.

van Loon, H., and Meehl, G.A. 2012. The Indian summer monsoon during peaks in the 11 year sunspot cycle. Geophysical Research Letters, 39(13), L13701.

Weiss, H. 2016. Global megadroughts, societal collapse and resilience at 4.2-3.9 ka BP across the Mediterranean and west Asia. Pages magazine, 24, 62-63.

Wilhelm, B., Arnaud, F., Sabatier, P., Crouzet, C., Brisset, E., Chaumillon, E., Disnar, J.-R., Guiter, F., Malet, E., Reyss, J.-L., Tachikawa, K., Bard, and Delannoy, J.-J. 2012. 1400 years of extreme precipitation patterns over the Mediterranean French Alps and possible forcing mechanisms. Quaternary Research, 78, 1-12.

Winner, C. 2012. Rain, Rivers, and the Fate of Civilizations. Oceanus Magazine, 49(3), 30-35.

Wright, R.P., Bryson, R.A., and Schuldenrein, J. 2008. Water supply and history: Harappa and the Beas regional survey. Antiquity, 82, 37-48.

Wünnemann, B., Demske, D., Tarasov, P., Kotlia, B.S., Reinhardt, C., Bloemendal, J., Diekmann, B., Hartmann, K., Krois, J., Riedel, F., and Arya, N. 2010. Hydrological evolution during the last 15 kyr in the Tso Kar lake basin (Ladakh, India), derived from geomorphological, sedimentological and palynological records. Quaternary Science Reviews, 29, 1138-1155.

Xi, D., He, H., Yu, Z, Huang, Q., Hu, J., Xu, Y., Shi, Z., Qin, Z., and Wan, X. 2018. New SIMS U-Pb age constraints on the largest lake transgression event in the Songliao Basin, NE China. PLoS ONE, 13(6), e0199507.

Yang, F., He, Y., Deng, Z.S., and Yan, A. 2016. Improvement of automated image stitching system for DR X-ray images. Computers in Biology and Medicine, 71, 108-114.

Zaragosi, S., Bourillet, J., Eynaud, F., Toucanne, S., Denhard, B., Toer, A.V., and Lanfumey, V. 2006. The impact of the last European deglaciation on the deep-sea turbidite systems of the Celtic-Armorican margin (Bay of Biscay). Geo-Marine Letters, 26(6), 317-329.